Article:

Hong, Jinhua, Jin, Chuanhong, Yuan, Jun orcid.org/0000-0001-5833-4570 et al. (1 more author) (2017) Atomic Defects in Two-Dimensioal Materials: From Single-Atom Spectroscopy to Functionalities in Opto-/Electronics, Nanomagnetism, and Catalysis. Advanced Materials. 1606434. ISSN 0935-9648

Published in Advanced Materials Vol.29, issue14, 1606434
Issue online: 6 APR 2017; Version of Record online 10 MAR 2017
This is author's preprint of the paper (DOI: 10.1002/adma.201606434)

DOI: 10.1002/adma.((please add manuscript number))
Article type: Review

Atomic defects in two-dimensional materials: from single-atom spectroscopy to functionalities in opto/electronics, nanomagnetism and catalysis

Jinhua Hong[1], *Chuanhong Jin*[1, *], *Jun Yuan*[1, 2, *], *Ze Zhang*[1, *]

Dr. Jinhua Hong, Prof. Chuanhong Jin, Prof. Jun Yuan, Prof. Ze Zhang
[1]State Key Laboratory of Silicon Materials, School of Materials Science and Engineering, Zhejiang University, Hangzhou, Zhejiang 310027, P. R. China

Prof. Jun Yuan
[2]Department of Physics, University of York, Heslington, York, YO10 5DD, United Kingdom

Keywords: point defects, S/TEM and EELS-ELNES/EXELFS, electronic structure, nanomagnetism, catalysis

Abstract: Two-dimensional layered graphene-like crystals including transition metal dichalcogenides (TMDs) have received extensive research interest due to their diverse electronic, valleytronic and chemical properties, with the corresponding optoelectronics and catalysis application being actively explored. However, the recent surge in two-dimensional materials science is accompanied by equally great challenges such as defects engineering in the large-scale sample synthesis. It is necessary to elucidate the effect of structural defects on the electronic properties, in order to develop an application-specific strategy for the defect engineering. Here in this paper, we review the two aspects of the existing knowledge of native defects in two-dimensional crystals. One is the point defects emerging in graphene and hexagonal boron nitride as probed by atomically resolved electron microscopy and their local electronic properties as measured by single-atom electron energy-loss spectroscopy. The other will focus on the point defects in TMDs and their influence on the electronic structure, photoluminescence and electric transport properties. Our review of atomic defects in two-dimensional materials will offer a clear picture of the defect physics involved to demonstrate the local modulation of the electronic properties and possibly benefit in potential applications in magnetism and catalysis.

1. Introduction

The discovery of graphene[1-10] and subsequent development of other graphene-like layered materials[11-17] have defined the history of two-dimensional materials research, which sparks considerably the exploration of low-dimensional condensed matter physics[2, 6, 8, 9, 16] and enrich the two-dimensional crystal family[18]. In the past decade, extensive research efforts have also been made in the exploitation of electric, optical and optoelectronic properties of 2D materials.

1.1 The rise of the 2D families

Modern electronics is fast developing in a trend that devices are becoming smaller, faster and cheaper[19], as exemplified by the Moore's Law. For example, TSMC and Intel are now already approaching the scaling extreme of 10nm and 7nm, respectively, below which quantum tunnelling or short channel effect[20] will occur. Many 2D materials have been considered as promising candidate[21] to break out the 5-nm theoretical scaling limit[22] of silicon transistors according to the Moore's Law. Very recently, Desai *et al.*[23] successfully demonstrated MoS_2-based transistors with 1-nm gate length using carbon nanotube as the gate electrode. The excellent switching performance[23] with nearly ideal sub-threshold swing and a high on/off ratio provides an exciting paradigm for 2D materials to open up a new era of highly-integrated 2D electronics alternative to the silicon-based microelectronics. The endeavor in discovering and engineering non-silicon 2D ultrathin channel materials[21] in transistor applications has never stopped, which now is marked by the coming of the era of 2D crystals and post-silicon electronics. As a large group, two-dimensional (2D) layered materials possess several distinct structural properties and diverse physical functionalities, ranging from superconductor, (semi)metal, semiconductor to insulator. As the corresponding typical member of 2D family, graphene, boron nitride (BN) and transition metal dichalcogenides (TMDs)[24] hold different promising potentials not only in electric, optoelectronic applications, but also in magnetic and catalytic chemistry. The former functionalities are closely associated with the intrinsic electronic structure, while the latter usually results from localized defect states. The band structure engineering linked through understanding of the structure-property correlation is a key topic of the nanophysics of 2D materials.

1.2 Why point defects?

Band engineering resides at the heart of modern microelectronics. The route to tailoring the electronic structure can be traced back to the modulation of the atomic structure by defects, doping and heterostructuring[18], for example. Silicon-based transistors, GaAs-based optoelectronic devices[25] and GaN-based light emitting diodes[26, 27] constitute the foundation of vast majority of modern electronics industry, which can be ascribed to great success of modern band engineering technology. Although the 2D material systems could be the hope of future electronics, their band modulation/engineering has not been extensively explored as the techniques responsible for the mature silicon semiconductor systems. Thus there is still a huge gap between the advance in the laboratory research and the industrial application, even though the 2D materials are known to present novel and promising properties in transport[28] and photovoltaics harvest[29, 30]. As structure disorder, including intrinsic defects and impurity dopants, is a very important factor involved in most semiconductors such as Si and GaN, the same challenge also needs to be explored in the 2D material synthesis and scalable applications.

1.3 TEM/EELS and other techniques to probe defects

To characterize the atomic structure of crystalline materials, many advanced techniques can be utilized such as X-ray diffractometers (XRD), transmission electron microscopes (TEM), scanning tunneling microscopes/spectroscopy (STM/STS) and atomic force microscopes (AFM). However XRD has its limitation in the spatial resolution and the latter three instrumentations has obvious advantage in directly imaging the structure of local disorders like atomic-scale defects. Based on the quantum tunneling effect of valence electrons, STM/STS has been shown as a powerful tool to image the atomic structure and defects on the sample surface, together with the local density of states which depicts the electronic structure such as bandgap, defect state and charge density wave[31]. And AFM[32] utilizes the tip-sample interatom van der Waals interaction to image the local structure even for insulator samples. Among these scanning probe microscopy techniques, only STM/STS will be involved in defects' characterization in a few parts of this review.

With the rapid development of aberration corrected electron optics[33-36], TEM or scanning TEM can now easily offer sub/atomic resolution imaging capabilities, thus they become the methods of choice to visulize the defects' atomic structure for ordinary samples together with local chemical and electronic information, for example, by Z-contrast imaging[37], electron energy-loss spectroscopy (EELS)[33, 38] or energy dispersive X-ray spectroscopy (EDX)[33]. However, sub/atomic resolution TEM imaging of graphene and BN remains a great challenge in the electron microscopy society because of the weak electron scattering power of the light elements. To increase the electron scattering and decrease the beam irradiation damage, low voltage 20~80 kV below the knock-on threshold is preferred. Recently, considerable progress have been made to push the low-voltage resolution limit to sub-atom level with a good signal-to-noise ratio (Nion[39] and JEOL-triple C[40], and the recent SALVE-Ⅲ project with Cc/Cs correction [41, 42]).

Based on inelastic scattering of high energy electrons, energy-loss spectroscopy in the TEM can probe the excitation of valence electrons (called valence EELS, or VEELS) of the sample to reveal the information about the local electronic structure. Plasmon excitation[43, 44] or bandgap determination[45, 46] have been successfully demonstrated by VEELS. Apart from the low-loss region where valence electron excitation dominates, the chemical identification and mapping can also be easily realized by high-loss spectroscopy or core-loss EELS where excitation of the inner shell of atoms in the sample can be studied. As a versatile tool different from EDX, core-loss EELS can also be used to measure the chemical shift and realize valence state mapping[47] in atomic resolution through electron energy loss near edge fine structure (ELNES)[37, 38, 48]. On the other hand, extended energy loss fine structure (EXELFS)[37, 38, 48] of the target atom comes from the scattering of its neighboring atoms and thus reflects the atomic coordination and the local crystal field.

In this paper, we will mainly review the aberration corrected (scanning) transmission electron microscopy (AC-(S)TEM) of single-atom defects discovered in typical 2D crystals and their spectroscopy revealing the defect physics including electronic and magnetic properties. Throughout the review, the terminology "single-atom or point defect" is used to include the traditionally known point defects such as vacancy, adatom, antisite and dopant atoms (or impurity)[49]. To limit the scope of the review, we mainly focus on only single-atom point defects and their effect on the electronic properties almost without involving line defects such as dislocations or grain boundaries, since a few other papers have reviewed the 0D-to-1D atomic defects in one specific 2D material systematically[50-54]. Valence electron energy-loss spectroscopy (EELS), electron energy-loss near edge fine structure (ELNES) or extended energy-loss fine structure (EXELFS) have successfully employed down to atomic scale, to demonstrate the defects' local electronic structure. The resulting effects on the macroscopic functional properties will be examined in transport, optical, magnetic measurements and change in heterogeneous catalysis. In the following sections, we will focus on three types of 2D crystal systems with different functionalities: semimetallic graphene, insulating BN and semiconducting MoS_2. Vacancies/antisite defects, dopants within the lattice of their monolayers and the modulation of the electronic structures will be systematically examined, with discussion on how these single-atom defects tailor the electronic, optical, magnetic and catalytic properties.

2. Graphene system

As a single-atom-thick hexagonal honeycomb-like structure, graphene has a linear Dirac cone without bandgap in its electronic structure[55] and exhibits high-mobility transport and room-temperature quantum hall effect of graphene[6, 8, 9]. Early experiments in mechanical exfoliated graphene show that this Dirac semimetal has ultrahigh electron mobility[56] ~10^5 $cm^2V^{-1}s^{-1}$, even larger than the commercial single-crystalline silicon and GaAs. Ideal graphene has very high mechanical stiffness[57] (Young's modulus~0.5~1 Tpa) and presents excellent thermal transport properties[58-60] (thermal conductivity~5500 $Wm^{-1}K^{-1}$) exceeding that of the diamond. Besides, graphene behaves inert in chemical reactions and is intrinsically nonmagnetic. Chemical vapor deposition[10] and graphene oxide (GO) reduction[61, 62] are the possible ways for large-scale synthesis to open up the industrialization of graphene. However, these preparation methods will inevitably introduce atomic defects in the as-grown graphene, which considerably affect the electric, thermal, mechanical, chemical and even magnetic properties. For instance, Hao *et al.*[63] reported the effect of defects on the mechanical and thermal properties that the Young's modulus gently decreases with the increase of the defect concentration in graphene, while the thermal transport is much more sensitive to the density of defects, since they act as scattering centers of the phonons and reduce the thermal conductivity. As the vacancy defects increase (to ~1%), the thermal conductivity decreases quickly towards 20% of that in perfect graphene[63].

2.1 Electronic states of edge atoms in graphene

Graphene has received great research interest as a promising candidate for future electronics, and the edge states of graphene play a crucially important role in the electric properties of graphene-based nanodevices. It is quite necessary to explore the electronic states of edge carbon atoms in graphene, which can be carried out with atomic resolution by scanning tunneling microscopy (STM) or scanning TEM (STEM) plus EELS.

Suenaga *et al.*[64] utilized low-voltage aberration corrected STEM to conduct single-atom spectroscopy analysis at the graphene edge, as shown in Fig. 1**a-d**. Only the carbon atoms at the active edge (marked by red and blue dots) are potentially mobile while all the others in the bulk-like region are stable under the bombardment of the scanning electron probe at low voltage 60kV. The red edge atom in Fig.1**b** is singly-coordinated, the blue one is doubly coordinated and the green atoms in the normal bulk-like region are triply-coordinated, also as shown in Fig. 1**c**. The K-edge ELNES of different carbon atoms are analyzed in the spectrum-imaging mode. The ELNES spectrum (green) in Fig.1**d** demonstrates the typical sharp

π^* peak (around 286 eV) and σ^* peak (at 292eV), characteristic of the bulk-state sp^2 carbon atom[65]. Compared with the standard triple-coordinated carbon ELNES, the spectrum (blue) from the double-coordinated carbon atom (on zigzag or armchair edge) presents an extra peak around 282.6 eV (marked as D). And the ELNES spectrum (red) from single-coordinated carbon atom (on Klein edge) has an extra peak at 283.6 eV (marked as S) except for the weaker normal π^* and σ^* peaks. In the core-loss spectrum, ELNES actually reflects the density of unoccupied states of the target atom. Thus, the ELNES spectra in Fig.1 is the experimental measurement of the density of unoccupied *2p* states of carbon atoms with different edge configurations, which indicates the unoccupied states are very sensitive to the chemical coordination. Suenaga's results are the first demonstration of such edge states measurement and advance our understanding of local structure-property correlation with single-atom accuracy. This ELNES analysis can be fingerprinting method to probe the electronic or bonding states of unknow nanomaterials down to atomic scale in combination with theoretical calculations[66, 67]

2.2 Localized plasmon enhancement in graphene

Plasmon resonance[68] has long been investigated and can be localized at nanometer scale[69], especially in metal nanoparticles[44, 70, 71]. Below the nanometer limit, the plasmonics theory based on the simple Drude model is no longer valid and the quantum effect will dominate the electronic excitation[44, 72, 73]. It is interesting to study the localization of plasmon resonance as it may bridge the size mismatch of optical wavelength and nanoelectronic devies and is useful for the realization of the integrated optoelectronics.

Zhou *et al.*[74] discovered the surface palsmon resonance can be enhanced at atomic scale especially at the sites of single point defects, as shown in Fig. 2. Electron energe-loss spectroscopy in aberration corrected TEM was employed to explore the atomic antenna induced by the localized enhancement of plasmon. The annular dark field image of the doped graphene in Fig. 2**a** demonstrates a silicon dopant atom replacing two neighboring lattice atoms of graphene. This substitutional Si dopant is four-coordinated with neighboring carbon atom. Figure 2**d** shows that the low-loss spectra of monolayer graphene are dominated by two plasmon-related excitation peaks: one is π plasmon at 4.5 eV; the other is $\pi+\sigma$ plasmon[4, 43] resonance at 15 eV. Detailed look into the plasmon excitation through spectrum imaging present an enhancement of $\pi+\sigma$ plasmon resonance at the silicon dopant defects, as shown in Fig. 2**e**. To demonstrate the spatial distribution, the $\pi+\sigma$ plasmon mapping is achieved through STEM-EELS in the spectrum imaging mode across the point defects, as shown in Fig.

2**b**. The plasmon decays exponentially with the increase of the distance from the defects. The intensity line profiles (Fig. 2c) of $\pi+\sigma$ plasmon mapping in Fig. 2b show that the plasmon has a localized enhancement with a full width at half maximum (FWHM) of 0.41 nm. This indicates the silicon dopants act as atomic antenna with a frequency on the order of 10^{15}Hz. This experimental demonstration of nanoplasmonics[75] down to single atom level suggests a possible route towards atomic-scale optoelectronic devices if engineering dopants along grain boundaries or interfaces of graphene can act as the plasmonic waveguide[69, 76]. This single-atom sensitive method could be extended to other dopants or defects to adjust the energy of plasmon resonance, which could benefit in designing plasmonic nanodevices.

2.3 Dopant atoms in graphene

Impurity atoms often exist in prepared crystal samples due to the complexity of the synthesis and further transfer process, for instance in chemical vapor deposition of graphene[10]. Generally, we can also regard impurity as unintentional dopant atoms. The local atomic structure and density of states of the individual dopant atoms can be obtained by STM or TEM.

Zhou *et al.*[77] utilized the annular dark field imaging and ELNES in core-loss EELS on an aberration corrected STEM to reveal the chemical bonding and local electronic structure of individual silicon dopants and clusters[78] in graphene. Figure 3a demonstrates the ADF imaging of threefold-coordinated Si dopant in a single-vacancy site, called as Si-C_3. And Fig. 3b shows the fourfold-coordinated Si atom occupying a double-vacancy site, marked as Si-C_4. Both types of Si defects are stable configurations replacing the lattice carbon atoms. The chemical bonding or hybridization of the substitutional Si defects can be further determined by single-atom ELNES analysis, as shown in Fig. 3d,e. The experimental L-edge ELNES of Si-C_3 (blue curve) and Si-C_4 (red) in Fig. 3e is a direct reflection of the density of unoccupied 3*d* states due to their different coordinations. DFT calculation revealed the relaxed geometry of Si-C_3 is a nonplanar structure with obvious out-of-plane distortion and Si-C_4 stays practically within the atomic plane of graphene (Fig. 3c, side view). This means Si-C_3 adopts sp^3 hybridization and Si-C_4 is sp^2d hybridized. The DFT calculated Si-C_3 ELNES (blue) in Fig. 3d show a sharp peak at 105 eV and a weaker shoulder at 101 eV agree well with the experimental spectrum. The appearance of 102.2eV and 107eV peaks and the absence of the sharp peak at 105eV in Si-C_4 simulated ELNES (red) are also consistent with the measurements.

Ramasse *et al.*[79] also discovered both types of Si dopants in graphene through annular dark field imaging and EELS-EXELFS. EXELFS is actually a reflection of the coordination environment or local crystal field. As shown in Fig. 3f, the calculated EXELFS of planar fourfold-coordinated Si coincides with the experiments and confirm its sp^2d hybridization. For the Si-C_3, the distorted geometry gives a more accurate simulation than the planar structure, compared to the experimental spectrum, indicating Si-C_3 is sp^3 hybridized.

The sharp peak at 105eV in Si-C_3 (Fig. 3d,e) is mainly resulted from electronic dipole transition into final states of unoccupied $3d_{xy}$ and $3d_{x2-y2}$ orbitals[77]. The Si-C_3 adopts sp^3 hybridization with neighboring C atoms, hence $3d$ orbitals will make negligible contribution to the density of states below Fermi level, as depicted in Fig. 3g. In contrast, the Si-C_4 has remarkable density of $3d_{xy}$ states near Fermi level, confirming its sp^2d hybridization. The red shift of $3d_{xy}$ states of Si-C_4 relative to that of Si-C_3 is a redistribution of empty electronic states, accounting for the absence of the sharp peak at 105 eV in the ELNES of Si-C_4. Figure 3h maps out the charge density distribution of $3d_{xy}$ state of the Si-C_4, further confirming its sp^2d hybridization[77] rather than sp^3. This combination of energy loss fine structure and DFT calculation successfully probes the chemical bonding or electronic states of single dopant atoms with three-dimensional structure and advance the physical chemistry to single atom level.

Intentional doping such as B or N has been long put forward in the band engineering of graphene to open its zerogap or tailor the Dirac electronic structure. Zhao *et al.*[80] imaged the local structure of individual substitutional N dopants[81] in graphene through atomic-resolution STM and measured the density-of-states by scanning tunnelling spectroscopy (STS), as shown in Fig. 4. The experimental STM image of single N dopant in graphene in Fig. 4a is consistent with the simulated image in Fig. 4b, and the central N atom substituting C lattice atom has obvious out-of-plane distortion (Fig. 4a, inset), indicating its possible sp^3 hybridization. Typical large-area STM imaging of N-doped graphene implies the random distribution of the N dopants. The measured STM spectroscopy of N dopants in Fig. 4c demonstrates the local change of electronic density-of-states near the Dirac point of graphene. The projected density-of-states of N dopant (Fig. 4d) reveal a resonance of its p_z orbital which is mainly located at 0.3eV above Fermi level, indicating the localized charge distribution of the N center. After measuring the STS spectra of N-doped graphene with different doping concentrations, each substitutional N dopant atom was found to contribute 0.42 charge carrier averagely (Fig. 4e). This is because only a part of the extra charge of each N atom will be delocalized into the graphene lattice due to the localized electronic perturbation caused by N dopant. Similar atomic-scale visualization of the individual N dopants in graphene has also been shown by Meyer *et al.*[82] using high-resolution TEM imaging on an aberration corrected

TEM plus a proper filtering process. This chemical doping opens a possible route to tailoring the charge carrier concentration of graphene film, which will enhance the catalytic activity as shown later.

2.4 Magnetism in graphene

Perfect monolayer or multilayer graphene is well-known nonmagnetic material, while intrinsic vacancies or external defects such as dopants will induce local magnetic moments. These defects will result in the overall macroscopic paramagnetism, and even high-Curie-temperature ferromagnetism has been reported by Wang et al.[83-85] in the hysteresis loop measurements of graphene.

Yazyev *et al.*[86] employed first principles calculations to study the magnetism in graphene induced by single-atom defects including hydrogen chemisorption and single vacancy. The projection of spin charge density of both defects shows the magnetic superstructure are both localized, as shown in Fig. 5. The chemisorption of H atom on top of carbon sublattice gives rise to the overall magnetic moment of 1 μ_B, where the central spin-up component has a ferromagnetic coupling with odd-nearest-neighboring sites and an antiferromagnetic coupling with even-nearest-neighboring sites (Fig. 5a). The magnetic moment is mainly localized on the central atom and its first-nearest neighbors. In the case of single vacancy[87] in graphene, its threefold symmetry is broken. This is resulted from the Jahn-Teller distortion since the removal of one carbon atom yields three dangling bonds and two of them tend to form a new C-C bond and the left one is unsaturated but makes the major contribution to the total magnetic moment of 1.1~1.5 μ_B (Fig. 5b). In both cases, the local magnetism does not originate from the *d* or *f* electrons of impurities or defects in traditional metals. Very recently, González-Herrero *et al.*[88] demonstrated a successful magnetic manipulation of individual H atoms adsorbed on graphene through magnetic coupling between neighboring H atoms, using spin-polarized STM. Lin *et al.*[89] utilized the ELNES of the core-loss spectroscopy to uncover the high-spin states of isolated metal dopants Fe, Cr occupying the divacancies or edges of graphene. These are experimental confirmation of the local nonmagnetic-to-magnetic transition through H or metal decoration on graphene, which demonstrates great potential to tailor the magnetic properties, early theoretically predicted by Krasheninnikov *et al.*[90].

Apart from DFT prediction of the defect induced magnetism in graphene, several experimental groups[83, 91, 92] offered tentative but indirect evidence of the macroscopic ferromagnetism or paramagnetism in graphene. Nair *et al.*[93] employed SQUID magnetometry to measure magnetic properties of defective graphene down to helium temperatures. By continuous tuning of the defects' stoichiometry, the defect origin of magnetism in graphene can be deduced (Fig 6). Two types of point defects, fluorine adatoms and single vacancies, show noticeable paramagnetism[93], but no magnetic ordering could be detected even at low temperature. Figure 6a shows the strong paramagnetism in distinctively fluorinated graphene where the fluorine atoms are chemisorption adatoms. As the fluorine concentration increases, the magnetization curve shifts upward. The number of spins, N_{spin}, increases proportionally with the concentration of paramagnetic F centers when the stoichiometry ratio F/C is less than 0.5. For higher F/C ratio, the number of spins get complicated with the increase of F adatoms. Irradiation induced vacancies also generated paramagnetism in graphene, since the overall magnetic moments increase with the vacancy concentration (Fig. 6b). The deduced magnetic moment per vacancy reaches 0.1~0.4 μ_B, which coincides reasonably with the theoretical DFT prediction of magnetic moments via vacancy mechanism ~1μ_B per vacancy[86]. Nair *et al.*[93] provided a systematic and comparable experimental approach to directly support the microscopic defects induced nanomagnetism introduced by many theoretical studies of graphene. Due to the low defect concentration limit, necessary for the structural integrity of graphene, the average spacing between magnetic centers are still too large (~10 nm) to form magnetic ordering, accounting for the absence of ferromagnetism in their experiments. Hence ferromagnetism observed in graphene remains to be explored whether in the nanostructure characterization or in the designated defect engineering.

2.5 Catalytic chemistry in graphene

Perfect graphene is known to be inert for most chemical reactions and presents weak catalytic activity if no defects or chemical decoration is introduced. Chemical modification with foreign atoms[94] can tailor the electronic structure of graphene and activate the catalytic behavior in a wide range of chemical reactions. For instance, various chemical doping of graphene by B, N, Si, P, S, Se, I atoms[94] have been reported to be a useful strategy for the improvement of catalytic applications of graphene such as oxygen reduction reaction (ORR)[95, 96], oxygen evolution reaction (OER)[97] and hydrogen evolution reaction (HER)[98, 99]. The former ORR is a chemical process widely involved in the fuel cells or metal-air batteries, where doping engineering makes graphene a promising metal-free nanocarbon catalyst[94].

Boron doped graphene[100] can be achieved through thermal annealing graphene oxide in boron oxide and exhibits excellent ORR catalytic activity in fuel cells[101]. The B dopants take a substitutional site in the hexagonal lattice of graphene. Local charge redistribution[102] occurs around B dopants: the positive charge is located on the B atom and negative charge on the neighboring C atoms, which behave as active centers for oxygen molecule adsorption in ORR catalysis.

N-doped graphene[97, 99] has been the most extensively investigated metal-free catalysis system for ORR since N atom is a donor. Layered N-doped graphene has not only high specific surface area, but also durable structural stability after plentiful cycles in ORR[95]. And its good conductivity facilitates the charge transfer or transport between the electrode and the catalytically active centers. N dopant atoms have been widely examined to be the sites for the enhanced ORR with high electrocatalytic activity and long-term stability[95], better than the commercial noble metal Pt, as shown in Fig. 7a. The localized defect states induced by the N dopant atoms are near the Fermi level of graphene, benefiting in the electron transfer from graphene to the antibonding orbitals of oxygen molecule in the oxygen reduction process[103]. Compared to the two-electron transfer in the pristine graphene, the N-doped system demonstrates a much more efficient transfer of four electrons in the oxygen reduction catalysis in alkaline fuel cells[104]. The N-doped graphene electrode yields large steady catalytic current density with immunity to CO poisoning, superior to the commercial Pt nanoparticle easily suffering from agglomeration and CO poisoning.

N atoms can be introduced through initial CVD growth[105], solvothermal process[106], arc-discharge[107] and post-growth annealing of graphene or graphene oxide in ammonia[95, 108, 109]. The substitutional N dopants in the graphene lattice will adopt three configurations[108]: triple-coordinated graphitic N in a hexagon, double-coordinated pyridinic N in a hexagon, double-coordinated pyrronic N in a pentagon. And these bonding states of N dopant atoms present different response to the ORR activity. The report by Geng *et al.*[95] suggested the graphitic N species play an important role in the 4e$^-$ ORR in alkaline solution. Lai *et al.*[108] found that the graphitic N was associated with the limited catalytic current density, while the pyridinic N improved the onset potential of ORR. The results of Niwa *et al.*[110] showed that the ORR activity of the doped graphene with more graphitic N content is higher than that of doped graphene with more pyridinic edge N, which partially coincides with the DFT prediction of the much lower energy barrier in graphitic N by Boukhvalov *et al.*[111]. However, the lack of comparative investigation on doped graphene with pure graphitic N or pyridinic edge N hinders a universal and persuasive conclusion on their contribution to the ORR activity enhancement.

Bangert *et al.*[112] employed low energy ion implantation to dope monolayer graphene with B and N atoms in a patterned way. By adjusting the energies of the ions, B or N atoms can be successfully planted into the lattice of monolayer graphene in a high substitution-to-vacancy ratio by dopants occupying the vacancy defects created. The whole monolayer structure is mostly hexagonal graphene lattices except dopant impurities, as shown in Fig. 7b. The annular dark field (ADF) imaging and single atom electron energy loss spectroscopy (EELS) allows structural and chemical analysis of dopants in graphene including element assignment and bonding nature[112]. Compared to the uniform ADF intensity of normal carbon lattice atoms, the B dopant has a darker intensity and the N atom is brighter (in Fig. 7b) as highlighted in the yellow dashed rectangles. Further spectrum imaging of the rectangular areas by STEM-EELS confirms the chemical species of both dopants (Fig. 7c,d). The obvious K-edges of B and N atom and their ADF images demonstrate their substitutional incorporation into the graphene lattice in a sp^2 hybridization. This detection is also an atomic-scale imaging of graphitic N dopant atom, as mentioned above.

Dual-doped graphene by B and N atoms has been successfully illustrated by Wang *et al.*[113] to tailor the band gap of graphene system with much better activity than the Pt/C. The B, N co-doped graphene was also found by Zheng *et al.*[114] to exhibit more excellent catalytic activity with a higher current density and larger onset potential than the single doped graphene. The dominating pathway of four-electron transfer for oxygen reduction accounts for the highly-enhanced ORR catalytic performance in the co-doped system.

3. Boron nitride system

Boron nitride (BN) has several crystalline phases: hexagonal, cubic, rhombohedral and wurtzite with the space groups of P63mmc, F43m, R3m, P63mc, respectively [115]. The cubic boron nitride is three-dimensional superhard material in a structure similar to the diamond and thus has the same highest Mohs hardness scale with applications in cutlery and drill[116]. Only the hexagonal phase BN will be discussed in this paper. Hexagonal boron nitride (BN) is white in color and has a similar honeycomb graphene-like layered structure, the BN is also called “white graphite” and used as a lubricant due to its low friction coefficient. Hexagonal BN is an insulator with an energy gap of 5.8 eV[11] and has extreme chemical stability at high temperature. Hence BN is often used as a high-temperature insulating ceramic or corrosion-resistant coating layer, and holds promising potential in graphene-based nanodevices.

3.1 Structural property in BN

As a two-dimensional planar graphene-like structure, atomically thin BN has received much research interest in its structural and electronic properties since its early preparation[117] by mechanical exfoliation. Jin *et al.*[12] and Meyer *et al*[82] used high-resolution aberration corrected TEM to reveal the hexagonal lattice structure of monolayer BN and directly discriminate the chemical species. As shown in Fig. 8a, single B vacancy can be easily distinguished in the HRTEM imaging of BN monolayer. Krivanek *et al.*[39] further employed quantitative ADF imaging for atom-by-atom structural and chemical analysis of BN monolayer containing C and O dopants (Fig. 8b). Each atom was unambiguously resolved and identified. Under the electron beam irradiation, point defects such as single boron vacancies[12] will be preferentially generated even at low voltage 80 kV. Continuous electron bombardment to the BN monolayer leads to the aggregation of boron vacancies to form triangular holes composed of three equivalent N-terminated zigzag edges. Similar experimental observation of zigzag edges formed at 120kV was reported by Meyer *et al.*[118]. The initial formation of single B vacancy has a three-fold symmetry and these gradually transforms into triangular holes under beam irradiation due to the asymmetric beam damage mechanism of the two distinctive sublattice in BN thin film. Alem *et al.* observed both zigzag and armchair edges in the BN nanosheet[119]. No vacancy reconstruction is found in the monolayer system, indicating the instability of B-B or N-N bonds in this 2D lattice of BN.

Alem *et al.*[120] visualized the structural Jahn-Teller distortion of single point vacancies in BN bilayer system via ultra-high resolution TEM where both spherical and chromatic aberrations are corrected. The sub-Å resolution image with a high signal-to-noise ratio show convincingly the local lattice distortion of the individual point defects. Figure 9a shows the exit-wave-reconstructed phase of a bilayer BN with the inset manifesting the image of a boron monovacancy (V_B) in either the bottom or the upper layer of the BN bilayer. Instead of the expected threefold *p*3 symmetry for the V_B vacancy, the experiments (shown in the inset of Fig. 9a) revealed a reduced *pm* symmetry due to the B-N bond reconstruction between layers caused by the Coulomb repulsion of the highly negative charge in the defect site. The DFT calculated structure of single boron vacancy in a BN bilayer has an obvious distortion from the three-fold symmetric structure, as shown in Fig. 9b, e. The experimentally reconstructed phase of the exit wave function coincides quantitatively with the simulated phase (Fig. 9c, d, f, g). The nearest-neighboring N lattice atoms around B vacancy get bonded with the B lattice atoms in the other layer, thus the B-N bonds are reconstructed between layers. This study is also important example of the advancement in the measurement of the three-dimensional structure distortion of single defects in combination with DFT simulation, in picometer-scale accuracy.

3.2 Electronic states of the vacancies in BN

The sites neighboring single vacancies preserve remarkably different chemical bonding and coordination environment compared to the faraway normal lattice sites, thus leading to unique electronic states. The detection of ELNES in the core loss EELS can be used to analyze the unoccupied electronic states of novel nanostructures or single point defects at the single atom level and sensitivity.

3.2.1 Electronic states probed by TEM

Suenaga et al.[121] combined ADF imaging and EELS-ELNES in an aberration corrected STEM to investigate the electronic properties of N atoms around the vacancy and N atoms from the normal sublattices. Although the delocalization effect of EELS signal is inevitable and limits the atomic-resolution chemical mapping of BN sublattices, the STEM-EELS technique still provides an easy access to the density of empty electronic states of the target N atom. Figure 10 a,b shows the ADF image of a BN monolayer with a B monovacancy and the structural model in Fig. 10c shows the chemical coordination environment. The EELS line profile conducted along the yellow arrow in Fig. 10b crosses the normal triple-coordinated N atoms “1 and 3” and unsaturated double-coordinated N atom “2”. The K-edge fine structures of each N atom are presented in Fig. 10d with the common π^* peak at 401 eV, resulted from the $1s \rightarrow \pi^*$ transition. A prominent prepeak at 392 eV appears on the unsaturated N atom “2”, which is highlighted in yellow. The structure of B vacancy indicates that this prepeak may be signature of the dangling bonds of three N atoms around B vacancy[121]. As shown in Fig. 10e, the DFT simulated ELNES spectra of normal N atom and unsaturated N atom around B vacancy show the obvious chemical shift of π^* peak in the vacancy case, highlighted by the arrow head. The dangling bonds of N atoms is calculated to have unoccupied molecular orbital with lower energy than that of the normal triple-coordinated N sublattice, thus giving rise to lower $1\mathrm{s} \rightarrow \pi^*$ transition energy and behaving as a sharp prepeak at 391.7 eV. Contour maps of the electronic states of the double-coordinated N atom in Fig. 10f display the spatial distribution of the occupied deep-level $1s$ state and the $2p$ state at the lowest unoccupied molecular orbital (LUMO). The $1s$ state deviates from the well-known spherical shape and seems to be attracted towards the vacancy center and the $2p$ state gets closer to this center. Three such equivalent N atoms do make contribution to the core-level transition as an obvious prepeak in the K-edge spectrum.

Compared with previous identifications of the chemical species of BN monolayer simply by quantitative ADF imaging or HRTEM phase reconstruction, Suenaga *et al.* provides a more direct evidence for the atom-by-atom structural and chemical analysis by mapping the electronic states of single defects through ELNES analysis[64] and theoretical calculations.

3.2.2 Electronic structure and single photon emitter

The introduction of vacancies into BN monolayer system will lead to localized defect states in the intrinsic band structure. Huang *et al.*[122] employed first principle calculations to show the in-gap defect level in the electronic structure, as shown in Fig. 11a,b. for the relaxed structure of vacancies V_B, V_N and V_{BN}. The corresponding schematic electronic structure is presented in Fig. 11b. The vacancy V_B has a Jahn-Teller distortion with its symmetry lowering from D_{3h} to C_{2v}. And two of the neighboring N atoms have the same spin direction, in antiparellel coupling with the spin of the third N atom, hence the distribution of magnetic moment of the neighboring N atoms in V_B is 1, 1, -1 μ_B, respectively. Defect states of V_B are complicated owing to the crystal field splitting and spin exchange splitting, resulting in one spin-up state moving down into valence band. The other three hole levels above valence band maximum indicate charge-neutral V_B is a triple acceptor, as shown in the left of Fig. 11b.

While for vacancy V_N, the structure remains three-fold symmetric (D_{3h}) with the total magnetic moment of 1 μ_B from the three neighboring B atoms in the same spin direction[122]. The V_{BN} has a C_{2v} symmetry and the spin is unpolarized, thus V_{BN} is nonmagnetic. For V_{BN}, the electronic structure in the right of Fig.11b imply that all the in-gap defect states are empty and high in energy and thus V_{BN} behaves as deep acceptors if in a charge neutral state.

The localized defect states induced by vacancies in BN may lead to novel physical properties such as nanophotonic emission[123, 124]. Tran *et al.*[125] showed a polarized and intense single-photon emission in hexagonal BN at room temperature (Fig. 11c). The photon energy of the excitation laser at 532nm (~2.3 eV) was much smaller than the gap of BN (5.8 eV) and thus excitation of the defect states within the gap can be expected. The brightest emission was found at 623nm (1.99eV) and localized within the atomically thin layers (see emission mapping in the Fig. 11c inset), together with other weak emission doublets at longer wavelength (1.99eV~1.79eV). The time-resolved fluorescence measurement of the brightest emission shows a lifetime of 3ns as well as its antibunching nature consistent with the characteristic of a single photon emitter. Linearly polarized dipole transition was also verified for this quantum emitter by excitation emission polarization measurements. This linear polarized dichroism actually reflects the highly anisotropy of the defect structure involved. Among the possible intrinsic vacancy defects (V_B, V_N, N_BV_N), the DFT calculations further support the anisotropic antisite-vacancy complex N_BV_N (N replaces one neighbouring B around V_N, Fig. 11c right inset) could be most likely defect responsible for the intense sub-bandgap quantum photonic emission in BN. The origin for other weak emissions (1.99eV~1.79eV), remain to be exploited.

3.3 Magnetic properties of dopant defects

Ideal monolayer hexagonal BN is a nonmagnetic material, similar to graphene. Doping transition metal atoms to occupy the vacancy sites of BN monolayer system is shown to be a theoretical possibility for chemical decoration and local magnetism. Exploring different transition metal dopant atoms is also necessary for designing magnetic and even catalytic[126] applications of BN nanosheets from the single atom perspective.

Huang *et al.*[122] calculated the relaxed structure of different transition metal adsorbates on the vacancy sites of V_B, V_N and V_{BN} in monolayer BN, as shown in Fig. 12a. The binding energy of transition metal atoms on V_B is obviously larger than that on V_N and V_{BN} (in Fig. 12b), which could be induced by a large charge transfer between metal atom and nearest-neighboring N atoms around V_B. And the geometry of absorption structure of each metal atom in Fig. 12c can be understood by the structure and charge distribution. Metal atoms on V_{BN} have a smallest height above the BN monolayer surface due to the largest empty space of the defects for the accommodation of the transition metal adatoms. The height of metal atoms on V_B is smaller than that on V_N due to the negative charge state of neighboring N atoms in V_B.

In the theoretical calculations[122] by Huang *et al.*, the total magnetic moment for the adsorption structures of single transition metal atoms on the vacancy sites is shown in Fig. 12d. For the case of vacancy V_B, the metal adatom transfers three electrons to the three in-gap hole states of V_B and itself becomes a metal ion in a +3 valence state. All the transition metal atoms are in the high-spin state because the exchange splitting is larger than the crystal field splitting except for Fe, Co, Ni. In the case of Fe, Co, Ni adsorption on V_B site, the large crystal field splitting results in a low-spin state, for instance, $d^{3\uparrow}d^{2\downarrow}$ for Fe^{3+}. By increasing the height of the adatom above the BN monolayer surface or applying an external electric field, the magnitude of crystal field splitting energies can be reduced. Thus the Fe adatom on V_B will undergo a 'spin crossover' from low-spin state to high-spin state, and this spin transition has been manipulated through spin-polarized STM experiments[127]. In the adsorption on V_{BN}, two electrons of the metal atom (M) transfer to the in-gap states of V_{BN} and yield a M^{2+} ion. The remaining valence electrons obey Hund's rules, resulting in the total magnetic moment's linear relation with the atomic number Z (blue curve in Fig. 12d). For the metal adsorption on V_N, the electron arrangement is quite complex and differs from that on V_B and V_{BN}, due to the hybridization of in-gap defect states of V_N and valence electron states 4*s*, 3*d* of metal ligands. Different spin configurations lead to various magnetic moments in the metal adsorption on V_N.

As an important theoretical prediction for a doped BN monolayer, the nanomagnetism induced by transition metal dopants calls for experimental exploration, especially for spin-polarized STM at the single atom level[128-131]. As the 'spin crossover' and magnetic states can be manipulated by varying the relevant crystal filed of vacancy defects as well as the external electric field[132], they could have applications in external field driven memory devices. The research into macroscopic scale magnetism in BN system should focus on valid defect engineering and the development of large-scale magnetic decoration.

3.4 Band engineering by carbon doping

Doping impurity atoms in individual vacancy defects tailors the electronic structure locally and plays a limited role in the change of the macroscopic properties, unless this doping can reach a relatively high level. For traditional silicon semiconductors, a quite low doping level ~ 10^{-6} is enough to considerably change the electric conductivity. However, in insulating BN system, heavy doping to a high level will be needed to transform its electric properties.

Monolayer BN has a single-atom-thick honeycomb structure similar to graphene with almost the same lattice parameters. The substitution of B or N by C atoms will not induce obvious lattice mismatch, thus carbon doping in BN monolayers yields coherent hexagonal BCN nanosheests. A transition from insulator to conductor after adequate doping was predicted by many theoretical calculation[133, 134] and observed experimentally[135] in the BN nanostructures such as nanosheets, nanotubes and nanoribbons.

3.4.1 Early researches on BCN bulk system

Watanabe *et al.*[136] measured the hall effect of chemical vapor deposited BC_2N thin film, and found it's a p-type semiconductor and its acceptor level is shallow, at between 5.5 meV and 23 meV. Later spectroscopic measurements by scanning tunnelling microscopy[137] revealed a characteristic optical gap of 2 eV, which is further verified by the low temperature photoluminescence spectra showing a 600 nm peak at 4.2K. Furthermore, the density-of-states of the occupied valence band measured by X-ray photoemission spectroscopy (XPS) shows a threshold energy of 0.95 eV valence band maximum locates above Fermi level. It can be deduced that the band gap must be larger than 1.9 eV, since the Fermi level is located almost in the middle of the gap but closer to the valence band extreme in a p-type semiconductor.

Chen *et al.*[138] remeasured the band structure of BC_2N thin film by angle-resolved electron energy-loss spectroscopy (EELS) in a STM high vacuum system. The band gaps at different parallel momentum transfers are derived from the onset energies of the low loss fine structures. Measurements of band gaps as a function of momentum transfer present a monotonically decreasing trend, indicating an indirect bandgap in the electronic structure.

From the experiments by Watanabe *et al.* and Chen *et al.*, the bulk BC_2N material is an indirect semiconductor with an indirect gap of 1.4 eV. The direct optical transition in bulk BC_2N has an energy of 2 eV, consistent with previous observations of a vertical gap by photoluminescence and XPS[137] and with the DFT calculation by Liu *et al.*[134].

3.4.2 Recent advancement in monolayer BCN system

Mazzoni *et al.*[133] systematically predicted the electronic structure and energetics of B-C-N hybrid graphene-like structures by first principle calculations. The formation energy of different configurations show that the structure with a sequence of zigzag C-C bonds is the most stable and no B-B or N-N bonds are favored. In the carbon-rich structure of BC_2N, the lowest formation energy lies in the configuration with the maximum of the number of B-N and C-C bonds, indicating a tendency towards island-like structures in segregated phases[133]. The electronic structures of the considered BCN configurations show a wide range of band gaps from zero to 2.5 eV. And some metallic structures are calculated to preserve relatively low formation energy. An insulating, semiconducting to metallic transition is therefore predicted with the increasing addition of carbon into the BN system. It is found that the hybrid structure with large band gap generally have the higher stability and is usually correlated with the chemical stoichiometry ratio of B/N ~1. In other words, under thermal equilibrium condition, the large-bandgap structure in segregated phases with maximum zigzag C-C bonds and B-N bonds is the most stable BCN hybridized system. The first-principles DFT calculations by Mazzoni *et al.* predict theoretically the separated BN and graphene domains in the carbon doped BN system[133].

Ci *et al.*[139] first synthesized two-dimensional hexagonal monolayer hybridized BCN through chemical vapor deposition. Almost no substitutional doping of B or N into graphene lattice occurs in this hybrid system. The ultraviolet visible absorption spectra of hybridized BCN atomic layers present two peaks corresponding to pure graphene and BN, confirming that this BCN system was phase-segregated with BN and graphene domains randomly distributed. Furthermore, the domains are expected to be larger than a few nanometers to screen the effect of short-period superlattice that makes a semiconductor. The optical response of BCN atomic layers preserves both properties of graphene and BN. In their electric measurements, the highly carbon-doped hybridized atomic layers present the electric resistance increasing dramatically as the temperature decrease, which is the characteristic of a semiconductor, indicating the graphene domain contribute to the insulating-semiconducting transition[139]. However, other groups found ternary alloy BCN near the domain boundaries of BN/graphene heterostructure[140] or even completely hybrid alloy phase in the high-temperature growth[141]. This is inconsistent with the previous theoretical prediction of the C/BN immiscibility by Yuge[142], and the contrasting experimental reports remain a controversy.

3.4.3 In-situ doping in TEM

Wei *et al.*[135] employed *in-situ* TEM to observe the doping effect of carbon in BN monolayer nanosheet, as shown in Fig. 13. They proposed a post-synthesis route[143] by utilizing the electron beam irradiation effect to create B or N vacancies for subsequent doping by carbon atoms decomposed from the hydrocarbon molecules intentionally introduced into the TEM. In this way, the BN monolayer can be completely transformed into conducting carbon system, and the intermediate state is semiconducting and magnetic BCN nanosheet. In Fig. 13a, the selected area electron diffraction of the doped BN nanosheets confirms the hexagonal lattice after long-time irradiation. During the continuous irradiation-damage assisted carbon doping, the chemical analysis was conducted by electron energy-loss spectroscopy and spatially resolved energy filtered TEM mapping. The comparison of the core loss EELS before and after irradiation in Fig. 13b indicate the successful doping of carbon atoms and the obvious π^* peaks at 284 eV mark the introduction of carbon in sp^2 hybridization. Energy filtered TEM image of B and C elements in Fig. 13c,d shows the enrichment of carbon atoms in central particular sites of the BN nanosheet, which hints the segregation of carbon phase domains. The *in-situ* electric transport measurements in Fig. 13e shows that the pristine BN is insulating and the doped BN nanosheets become conducting. And also the electric conductivity increases obviously with the irradiation time, indicating a transition[135, 143] from insulator, semiconductor to conductor, which is in good agreement of previous theoretical predictions on BCN system. This *in-situ* experiment by Wei *et al.* demonstrated an effective and precise control of electric and magnetic properties of two-dimensional nanosheets through irradiation-assisted doping of carbon.

3.4.4 Band edge excitation of BCN monolayer by EELS

Arenal *et al.*[144] employed spatially-resolved STEM-EELS to study the bandgaps of single-wall and double-wall BN nanotubes. The low-loss electronic excitations of all nanotubes show a threshold at ~5.8 eV, which is an independent nonoptical measurement of the wide gap of BN nanostructures. Pan *et al.*[145] investigated the electron energy-loss spectroscopy of BN nanosheets with different thicknesses and found unique extra electronic excitations in the monolayer below its band gap threshold 5.8 eV. As shown in Fig. 13f, the atomically-resolved ADF image of a BN monolayer shows abnormal intensities at some atomic sites, indicating the possible substitution of impurity atoms. Quantitative ADF intensity analysis discriminates the chemical species of dopants such as C atoms (in yellow), O atom (in dark blue) from the normal B (light blue) and N (gray) atomic sublattices. Based on this atomic model in Fig.13f, the DFT has been used to calculate the low-loss spectrum (by WIEN2K package) which is shown as the black solid curve in Fig. 13g. This is to be compared with the experimental low-loss spectrum shown as the gray curve. Two obvious peaks at 6.3 eV and 14.3 eV are the typical π, σ plasmon resonance of the BN monolayer. Low-energy pre-peak extends to 3 eV on the shoulder of the π plasmon peak, and this pre-peak structure appears only in some localized regions. Another shoulder structure at 7.5 eV on the high-energy side of the π plasmon peak was also only selectively observed. These abnormal low-loss fine structures[145] are believed to be associated with defects inside, which can be inferred from the fact that only a few localized regions give these preplasmon or postplasmon shoulder structures. This has been collaborated by the quantitative ADF imaging and impurity atom assignment in Fig. 13f. Correspondingly, the calculated spectrum is consistent with the experimental low-energy preplasmon structure, as indicated by the blue arrows in Fig. 13g. The local substitution of carbon atoms in BN sublattices corresponds to moderate doping, which make the electronic excitation extends to lower energy region of the spectrum, suggesting the transformation into a semiconductor. This EELS measurement by Pan *et al.* presents another non-optical and nonelectric experimental approach for the checking of the insulator-to-semiconductor transition through electronic structure engineering by carbon substitutional doping in monolayer BN.

4. Transition metal dichalcogenides (TMDs)

Among the two-dimensional graphene-like materials, layered transition metal dichalcogenides (TMDs)[24, 146-148] have recently also attracted extensive research interest in their atomic structure, unique electronic and optical properties, electric transport because of its great significance in valleytronics[149-152] and electronics[23, 28, 153] application. As a typical TMDs family, Ⅳ-Ⅵ group MX_2 (M = Mo, W; X = S, Se) has three types of crystal phases: 1T phase as a metal; 2H phase and 3R phase as semiconductors. Among these polymorphs, hexagonal MoS_2 in 2H phase has already been investigated widely in materials research and in industrial applications[154] of lubricants and hydrodesulfurization catalysts. As a representative of TMDs, MoS_2 has many structure, electronic, optoelectronic and catalytic properties similar to other TMDs-MX_2. Hence we mainly focus on MoS_2 to limit the scope of this section, where most contents are also applicable to other Ⅳ-Ⅵ group TMDs.

4.1 Introduction of MoS_2

Monolayer 2H-MoS_2 has a sandwiched structure in a trigonal prismatic coordination formed by covalent bonding between Mo and S atom layers. The basic skeleton of single layer MoS_2 are assembled into its bulk counterpart through interlayer van der Vaals interaction and specific interlayer stacking sequence, similar to h-BN and graphite. The layered nature of the bulk MoS_2 makes interlayer sliding easily happen when it's subject to external friction, therefore they are often used as lubricants. In addition, large interlayer separation provides enough space for mass transportation of small molecules in the interlayer channels with high specific surface area, thus there is considerable potential for applications in lithium ion battery[155, 156] and hydrogen storage[157].

Since the weak van der Waals interaction between layers, micromechanical exfoliation[17, 158], liquid-phase ultrasonic dispersion[159] were widely employed to prepare MoS_2 atomic layers. Laser[160] or plasma thinning[161] has also been adopted to obtain few layers from thin flakes. However, these top-down methods are impractical for the scalable production. Solutions such as chemical/physical vapour deposition enable wafer-scale production of monolayer or few-layer MoS_2 nanosheets. For the CVD growth approach, ammonium tetrathiomolybdate[162, 163] $(NH_4)_2MoS_4$ can be decomposed in Ar+S gas at a temperature 1000 ℃ to form MoS_2. Molybdenum oxides[164-166] (MoO_3, MoO_2) can also be reduced to MoS_2 under the flow of S vapor. So far, synthesis of large area high quality MoS_2 by CVD provides a very effective way for its electric and optoelectronic application.

The most attractive physical properties of layered MoS_2 lie in the thickness-dependent behaviour of its optical, electronic transport and optoelectronic properties which are deeply rooted in the electronic band structure. Interesting quantum confinement effect[13, 158] appears in the form of a crossover[167] from the indirect to a direct gap semiconductor when the layer number of MoS_2 decreases from bulk to monolayer. From multilayer to bilayer, the MoS_2 present an increasing indirect bandgap from ~1.3 eV to ~1.6 eV. In the monolayer limit, MoS_2 has been reported to behave as a direct semiconductor[158] with a bandgap 1.8 eV, indicating its potential application in optoelectronics and photovoltaics[147, 168, 169]. Besides, the monolayer MoS_2 lacks an inversion symmetry that is present in the multilayer's crystal structure, leading to different interband transition selection rule in the vicinity of K and K' points of the first Brillouin zone, giving rise to valley contrasting circular polarization dichroism[149-151, 170]. This valley dependent dichroism has also been identified in the electroluminescence measurements[171].

Monolayer MoS_2-based field effect transistors[28] show a high current on/off ratio $\sim1\times10^8$, although the charge carrier mobility is still low for electronic applications. Mechanically exfoliated MoS_2 monolayers have been utilized to fabricate FET devices to detect environmentally detrimental gas NO[172] with a high sensitivity up to 0.8ppm. Most MoS_2 nanosheets used as the channel material in FETs are n-type semiconductors, and the origin of this doping character is still unclear with some research suggesting either S vacancies or impurity atoms[173].

Surface adsorbates, intrinsic structural defects[174] such as point defects, dislocations and grain boundaries, and edge structures are all considered as important causes for the low mobility of charge carriers in electric transport and highly enhanced catalytic activity. Plentiful efforts have been taken to identify these nanostructures by recent atomically resolved transmission electron microscopy. Atomic defects such as vacancies[174] (pristine) and grain boundaries[164, 165] have been discovered in monolayer MoS_2 prepared by CVD growth. Wang *et al.* have synthesized MoS_2 nanoribbons[175] encapsulated in carbon nanotubes. For nanoribbons, the armchair type presents a width-dependent semiconducting gap, while the ferromagnetic zigzag nanoribbons are always metallic regardless of the width [176, 177]. For consistency with the above sections, we will only discuss the defects in atomic size including point defects, adatoms and impurity dopants in monolayer MoS_2 system and show how they tailor the electronic, magnetic and catalytic properties.

4.2 Point defects in MoS_2

Direct semiconducting property with a proper bandgap of 1.8 eV makes monolayer MoS_2 a proper candidate in field effect transistors, integrated logic circuits, photodetectors, gas sensors and flexible optoelectronic or plasmonic devices. The widely-adopted synthesis of MoS_2 atomic layers by chemical vapor deposition[166, 178] help to bridge the gap between large-scale high-quality crystal growth and the nanoelectronic applications. However, the obtained electron mobility[179] of MoS_2 is much lower than that of the mechanically exfoliated counterparts[180]. Furthermore, all experimentally reported electron mobilities of CVD, PVD or mechanically-exfoliated MoS_2 have almost one order of magnitude lower than its theoretical limit[181] of $410 cm^2V^{-1}s^{-1}$. Such large discrepancies are widely believed to arise from charge carrier scattering centers such as point defects, grain boundaries, surface adsorption, dangling bonds or Coulomb impurities. These defects are common in any crystal materials, and have been thoroughly investigated in traditional Si or GaN semiconductors as they play a crucial role in the electric and optical properties[49].

Zhou *et al.*[174] gave a systematic characterization of intrinsic atomic defects in CVD grown MoS_2 by atomic resolution annular dark field (ADF) imaging in an aberration corrected TEM, as shown in Fig. 14. The ADF imaging is also Z-contrast imaging and allows for atom-by-atom chemical mapping through quantitative intensity analysis. Hence it is easy to directly assign the type of the point defects. Shown in Fig. 14a, the sulfur vacancies in MoS_2 include mono-vacancy (V_S) and double-vacancy (V_{S2}) with only one or two S atoms missing from the sulfur sublattice site. Both are single-site vacancies. Other extended Mo vacancies such as V_{MoS3} and V_{MoS6} were also observed, where the central Mo atom and its neighboring S atoms are absent. Besides these vacancies, antisite defects with Mo atom replacing S2 column (Mo_{S2}) or S2 occupying the Mo site ($S2_{Mo}$) are also found. Among all these observed point defects, only antisite defect Mo_{S2} breaks the threefold symmetry of the underlying lattice structure. In the observations by Zhou *et al.*, vacancy V_S is the most common defect, while antiste defects are only occasionally found, in agreement with the lowest formation energy of V_S in their DFT calculation[174].

Lin *et al.*[182] performed an atomic structure study of monolayer MoS_2 doped by Au and Re impurity atoms and observed their atomic-scale migration on the surface. As shown in Fig. 14b,c, dopant atoms on the monolayer MoS_2 substrate are Re and Au, respectively. The Re atom tend to substitute the Mo sublattice and thus leads to the experimental observation that nearly all Re atoms are located at the site of Mo, also in accordance with the theoretical calculation by Dolui *et al.*[183]. While in the case of Au dopant, the substitutional doping will have very high formation energy, hence the Au prefer to stay as an adatom site. Single Au adatom can adopt three different adsorption configurations: on top of Mo, S and the hollow center, as shown in the inset of Fig. 14c. These individual Au dopant atoms are quite chemically active and tend to aggregate into clusters by surface migration. Although Re dopants replacing Mo sublattice do not migrate, the agglomeration of carbon impurities always occur around Re to form a cluster, indicating the chemical activity by dopant's decoration. Both types of dopant atoms by substitution or adsorption exhibit chemical reactivity and may act as active sites in catalysis.

4.3 Electronic and magnetic properties of atomic defects

To explore the local electronic or magnetic structure in MoS_2 system and energetics induced by defects, first-principles density functional theory calculations has been widely used, although mostly employed in semiquantitative interpretation in energetics. Many such experiment-theory joint investigations have successfully presented the evidence for the modification of electronic properties of MoS_2.

4.3.1 Sulfur vacancies V_S and dopants occupying V_S

Komsa et al.[184] discovered that single vacancies V_S and V_{S2} could be readily created by electron beam irradiation at acceleration voltage of 80kV. As shown in Fig. 15a, the HRTEM of monolayer MoS_2 demonstrate the hexagonal atomic structure with an edge terminated by Mo atoms. Within the nanosheet, large numbers of sulfur vacancies can be found with the characteristic three-fold structural symmetry. The simulated HRTEM images in Fig. 15d, e based on the structure of vacancies V_S (Fig. 15b) and V_{S2} (Fig. 15c) agree quantitatively with the experimental imaging in Fig. 15f. During the continuous observation under electron beam, more S vacancies appeared in the monolayer. A knock-on elastic scattering model with lattice vibration taken into consideration[185] has been proposed in the irradiation damage mechanism, which can reasonably account for the experimentally derived displacement cross sections.

Impurity atoms in the TEM chamber tend to fill in the vacancy site of MoS_2, forming a substitutional dopant atom. Komsa et al. explored the electronic properties induced by various dopant atoms by DFT calculations[184]. Figure. 15g shows the local spin-resolved density of states of different dopant atoms where occupied defect states are filled in color. It is obvious that N, P, As and Sb in V-A group behave as acceptors and F, Cl, Br, I in Ⅶ-A group are obviously donors. All these dopants have asymmetric spin-resolved density of states with extra electrons occupying the spin-up state, indicating their local magnetism. Other impurity atoms C and Si induce symmetric unoccupied mid-gap states. Komsa *et al.* demonstrated electron-beam mediated single-atom substitutional doping as a new way for engineering the electronic structure of TMDs.

4.3.2 Metal dopants substituting Mo lattice atom

Dolui *et al.*[183] employed ab-initio calculation to study various dopants at substitutional sites and adsorption sites in monolayer MoS_2. Nb, Zr and Y atoms are found to prefer to substitute the Mo lattice sites and act electronically as p-type dopants since they have less number of the valence electrons than Mo ($4d^5 5s^1$). The Nb doping induced p-type transition has also been confirmed by later experiments by Suh *et al.*[186]. These p-type dopants create acceptor states just above valence band maximum. As n-type donors, Re atoms ($5d^5 6s^2$) adopt an energetically preferred configuration replacing Mo sites. At 0.19 eV, its donor level has the lowest activation energy among all the possible n-type transition metals. However, the incorporation of any transition metal by substitutional doping does not create shallow donor states. Another way for n-doping is by introducing alkali atoms, as reported later in the electric transport by Fang et al.[187]. The alkali metal atoms tend to adsorb on top of Mo sites (T_{Mo}) and are an n-type dopants by donating *s* valence electrons[183]. Degenerate doping of alkali metals will shift the Fermi energy into the conduction band.

Cheng *et al.*[188] predicted from first-principles calculation that monolayer MoS_2 doped by transition metals is a two-dimensional dilute magnetic semiconductor. In their calculation, Mo vacancies and S vacancies do not have local magnetic moment. The metal elements from IIIB to VIB group has no more valence electrons than Mo, hence their substitution of Mo does not induce magnetism. Among VIIB-to-IB group metals substituting Mo sublattice, only Mn, Fe and Co preserve the C_{3v} symmetry and show magnetism, and all the other metals (even like Ni) preserve no magnetic moment because of the structure symmetry reducing from C_{3v} to C_1 as Jahn-Teller distortion occurs in the structure relaxation. For IIB group metal Zn, Cd and Hg, the substitutional dopants all induce magnetic moment of $2\mu_B$. Further calculations demonstrate that the magnetic ground states for Fe and Co dopants adopt antiferromagnetic coupling, while the other magnetic dopants Mn, Zn, Cd and Hg take ferromagnetic ordering when their concentration is over 6.25%. The proposed Curie temperature T_C is far below room temperature and reaches 93K in the case of Mn doping.

Mishra *et al.*[189] predicted that single Mn atom dopants substituting Mo lattice atom induce an antiferromagnetic coupling with the neighboring chalcogenide atoms resulted from the *d*-*p* hybridization. Such a magnetic 'superatom' can form in MoS_2, $MoSe_2$ and $MoTe_2$ system. When the doping concentration increases to 5%, each magnetic superatom is energetically favorable to form ferromagnetic coupling with the neighboring superatoms, well consistent with the results by Cheng *et al.*[188]. This long-range ferromagnetic ordering can be ascribed as the exchange interaction of Mn-*d* spins and S-*p* spins.

4.3.3 Intrinsic antisite defects

Hong *et al.*[190] discovered that the dominant type of point defects in monolayer MoS_2 is highly related to the sample synthesis methods, indicating the possibility for defect engineering via sample growth or formation mechanism involved. It is observed that antisite defects Mo_{S2} with Mo occupying the sites of S sublattice are the dominant point defects in physical vapor deposited[152, 191-193] (PVD) MoS_2. While sulfur vacancies V_S (in Fig. 14a, or Fig. 15f) are the most common defects in monolayer MoS_2 prepared by mechanical exfoliation (ME)[158] and chemical vapor deposition (CVD)[162, 163, 166, 178]. The experimentally observed population ratios of different defects' concentrations are consistent with the expectation based on the DFT calculated formation energies of defects. A tentative growth mechanism[190] has been outlined for the formation of antisite defects in the PVD growth.

The predominant defects such as antisite Mo_{S2} and Mo_S (shown in Fig. 16a) in PVD samples are determined to reach a density of $(2.8\pm0.3)\times10^{13}$ cm^{-2} and 7.0×10^{12} cm^{-2}, corresponding to an atom percent of 0.8% and 0.21%, respectively. These concentration levels are even higher than that of the dominant point defect V_S vacancy in the CVD samples with a statistical concentration of about $(1.2\pm0.4)\times10^{13}$ cm^{-2}, which is close to other previous experimental reports[194] of vacancies in MoS_2. As dominant defects (vacancies or antisites), such defect concentrations (0.8%~0.2%) are both remarkably high if the defects are all electronically active, since the doping level of degenerate semiconductor is only on the order of 10^{-2}~10^{-4}.

Such high doping level of point defects often hints considerable modification of the electronic properties[190]. As an example of antisite defects, Fig. 16 shows the atomically resolved ADF image of antisite Mo_S with Mo replacing only one S atom in a S_2 sublattice column. The relaxed structural model of antisite Mo_S in Fig. 16c, d still retains the three-fold symmetry and the simulated ADF image in Fig. 16b agrees well with the experimental imaging. On the other hand, the antisite Mo_{S2} (in Fig. 14a) has an obvious off-center characteristic because of the deviation of the antiste Mo atom from the center of the triangles formed by three most neighboring Mo atoms. This structure property makes a big difference from the three-fold symmetry of antisite Mo_S and leads to contrasting magnetic properties.

It is known to all that perfect monolayer MoS_2 is a nonmagnetic semiconductor and sulfur vacancies alone will not induce local magnetism[190]. Owing to the advanced first-principles calculation, Hong *et al.* finds only antisite Mo_S will give rise to magnetism in monolayer MoS_2, while other defects such as V_S, V_{S2}, and Mo_{S2} preserve no magnetic moments, where all defects are considered in a neutral state. The calculated electronic structure of antisite Mo_S is shown in Fig. 16e, where the defect states behave as nearly flat band dispersion within the intrinsic band gap of a perfect MoS_2 monolayer. The flat dispersion also indicates the highly involvement of Mo-*d* electrons and these in-gap states were deduced to mostly originate from the *d* orbitals of the four Mo atoms within the ansite defect. Further, the density distribution of extended electron wavefunction around the antisite Mo_S form a ‘superatom’ with a radius of roughly 6 Å, representing the hybridization of Mo-*d* and S-*p* orbitals as shown in Fig. 16g.

The calculated spin charge density of antisite Mo_S presents the magnetic structure with a total magnetic moment of $2\mu_B$, as shown in the visualized spin density distribution (Fig. 16f). For the Mo_S antisite, the strong orbital hybridization between central Mo and surrounding atoms yields such a magnetic ‘superatom’ where the magnetic moment is not localized only on the central Mo atom as the neighboring atoms also contribute about 20% of the total magnetic moment. Figure 16g plots the spin-resolved distribution of a defect-induced state (state 3) marked in Fig. 16e to illustrate the origin of the magnetism. The occupied spin-up component (yellow isosurface) is mainly composed of the d_{xy} and d_{x2-y2} orbitals of the antisite Mo atom, while the unoccupied spin-down component (cyan isosurface) is projected onto the

d_{xy} and d_{z2} orbitals of surrounding Mo atoms, consistent with the total spin charge density shown in Fig. 16f.

The difference of magnetic antisite Mo_S and nonmagnetic Mo_{S2} can be well explained by crystal field theory and hybrid orbital theory. In the case of three-fold symmetric Mo_S, the antisite Mo takes d^4s hybridization forming five orbitals, i.e. s, d_{xz}, d_{yz}, d_{xy} and d_{x2-y2}, which are filled by eight electrons, six from the antisite Mo and two from the adjacent Mo atoms. The former three orbitals are occupied by six electrons and the latter two, degenerated in energy, are filled by two electrons which are unpaired. The spin direction of these two electrons aligns in parallel due to on-site Coulomb repulsion according to Hund's Rules, thus contributing to the magnetic moment of 2 μ_B. In the case of antisite Mo_{S2}, however, the antisite Mo atom is significantly off the symmetrical center of the three neighboring Mo atoms, leading to orbital d_{xz} missing in the formation of bonding, therefore, the antisite Mo takes d^3s hybridization forming four hybridized orbitals, originated from s, d_{xy}, d_{x2-y2}, d_{yz}, filled by eight electrons. As a result of the d^3s hybridization, the defect Mo_{S2} is non-magnetic. The structural symmetry breaking of antiste Mo_{S2} makes a big difference in the magnetic properties[190], in contrast with the antisite Mo_S. The experimental confirmation of this interesting magnetism calls for the exploration of the atomic defects' chemical physics possibly by spin-polarized scanning tunnelling microscopy and spectroscopy at the single atom resolution and sensitivity.

4.4 Optical properties and nanophotonics by vacancies

Defects usually have a dominating influence on the physical properties of tow-dimensional materials. For instance, the Raman-active centrosymmetric A_{1g} mode will appear in the defective graphene, which has been taken as a criterion to value the crystal quality of graphene and is thus generally marked as D-peak[195]. Different from the case of graphene, the sandwiched structured TMDs like MoS_2 and WS_2 exhibit no such characteristic/fingerprinting Raman peaks that can be directly related to defects. However, Parkin et al[196] recently discovered the shift of first order Raman mode (E_{2g}) dependent on the density of sulfur vacancies introduced by electron beam irradiation inside the TEM.

Chow et al.[197] engineered the vacancy defects in mechanically exfoliated MoS_2 and WS_2 monolayer (Fig. 17a,b) through controllable ion bombardment in Ar plasma treatment. The created vacancy defects' concentration increases with the plasma etching time, but no obvious changes were observed by Raman spectroscopy, indicating its insensivity to defect formation. In contrast, vacancy defects give rise to characteristic peaks in the room-temperature photoluminescence (PL) spectroscopy of these TMDs, resulted from the gradually emerging exciton-defect interaction. Figure 17a shows the normalized PL spectra of exfoliated MoS_2 monolayers treated by plasma etching. In the pristine prepared MoS_2 monolayer, the PL spectrum is dominated by the peaks of neutral charged excitons $X^{O,A}$ and $X^{O,B}$ (A, B excitons in other literatures[158]) from the direct transition at K-point gaps. Other charged exciton X^T (trion[198]) could also be deduced by Gaussian fitting and emerges more clearly as a low-energy tail to the main excitonic peaks in the case of pristine WS_2 monolayer in Fig. 17b. These minor features are found to stem from Coulomb impurities, lattice strain, or unintentional impurity doping in the pristine exfoliated monolayers[197]. In other words, the inherent n-type electronic properties of pristine MoS_2 or WS_2 account for the charged trion emission X^T.

With the increase of the plasma treatment time, an extra peak X^D (specific to defects) arises at 0.1eV lower than the $X^{O,A}$ exciton and becomes more intense in monolayer MoS_2 (Fig. 17a). This subgap feature X^D can be attributed to excitons bound to vacancy defects intentionally induced by plasma bombardment. Similar enhancement of vacancy-related exciton peaks is also observed in the monolayer WS_2 shown in Fig. 17b. Besides, the charged excitons emission X^T (trion) become weaker with the plasma treatment, indicating the annihilation of intrinsic charged exciton due to the compensation effect of plasma ions[197]. This compensation mechanism also explains the slow increase of defect-bound exciton lines X^D at the beginning of the plasma treatment. The rapid increase of X^D peaks after a period of plasma etching suggests the introduction of the vacancy defects, which is directly confirmed by further HRTEM characterization.

Tongay *et al.*[199] investigated the effect of anion vacancies in TMDs on the optical properties which is obvious at low temperature. Controllable irradiation of α particles induced vacancies in monolayer MoS_2. An exciton emission bound to defects appears at 0.15eV below the free neutral exciton peak X^O corresponding to the direct K-K valley transition. With the increase of α particle dose to 8×10^{13} cm^{-2}, the new subgap peak emerging at 1.78 eV get more intense since this arise from the radiative recombination of neutral exciton bound to defects. The sub-bandgap emission demonstrates the exciton physics induced by artificially introduced vacancies, which would be applicable in optoelectronics through controllable defect-exciton interaction in the defect-lattice superstructures.

Nan *et al.*[200] employed oxygen plasma etching for the defect engineering of monolayer MoS_2. In contrast to the reports shown above, no defect-bound exciton peaks were observed, indicating the oxygen processing did not create vacancies but possibly generated substitutional dopant. Nan *et al.* observed a 1000-time photoluminescence enhancement of the neutral exciton X^O main peak after oxygen plasma treatment. Such huge increase is associated with the p-doping effect of oxygen bonding, which reduces the negative charged trion in the n-type pristine MoS_2. The low-temperature spectra illustrated the suppression of nonirradiative recombination of neutral exciton at the presence of oxygen dopant after the plasma treating. This defect engineering opens up the trion-to-exciton conversion, which accounts for the strong PL enhancement and would be a methodology for the applications in light-emitting devices.

Photoluminescence or cathodoluminescence allows the detection of defect exciton state which is below the energy of the delocalized neutral exciton in direct K-K transition of TMDs. Fabbri *et al.*[201] reported a new near-infrared emission at 0.75 eV in a multilayer MoS_2 flake. The cathodoluminescence mapping of this peak demonstrated its distribution only around the edge regions, which were identified to contain rich sulfur vacancies by aberration corrected TEM and EELS. The DFT calculations and experimental results supports the proposition that sulfur vacancies lead to the novel subgap emission in MoS_2. Recently, single-photon emission with ultranarrow linewidth (~130 μeV) and long lifetime (1 ns) has been discovered in the WSe_2 system at low temperature[202-205]. These quantum-dot-like exciton emissions are located 40-100 meV below the K-K valley exciton. The spectroscopic mapping of the single-photon emissions shows they are from highly localized sites on the uniform monolayer, indicative of exciton bound to atomic defects. Several types of single-photon emission emerge as a function of the photon energy and show different Zeeman-splitting responses to the external magnetic field. The underlying defect structure is still unknown and need to be explored to understand the microscopic mechanism of the observed single-photon emission. Nevertheless, these examples show the integration of quantum dot photonics in TMDs-based optoelectronic devices has great potential for quantum information processing[204].

4.5 Electric transport properties induced by atomic defects

Defects in monolayer MoS_2 will induce localized states within the direct bandgap and result in the characteristic defect excitons[197, 199] observed by Chow et al. and Tongay et al. In addition to the modification of the optical properties, structural defects also considerably affect the electric transport properties, particularly at low temperature.

Qiu et al.[194] observed the variable-range hopping (VRH) transport phenomena at a low carrier density in the field effect transistor based on monolayer MoS_2, as shown in Fig.17 c-e. The charge carrier density is modulated by the gating voltage. The measured conductivity (σ) of the back-gated transistors below a critical carrier density behaves as functions of the temperature (T). In the low-temperature region, the measured conductivity has a much weaker temperature dependence, well fitted by 2D variable-range hopping equation, which is typical of transport through localized states. In the high-temperature region (Fig. 17e), the Arrhenius plot of the normalized σ shows activated electric transport since the high temperature induces rapidly-increasing electric conductivity. And the experimental curve can be well fitted by the Mott's formalism $\sigma \sim \exp(-T_0/T)$, indicating the transport is dominated by nearest-neighboring hopping between localized defect sites. This is associated with sulfur vacancies in the pristine MoS_2 as revealed by high resolution electron microscopy. The DFT calculation shows the in-gap defect states has dispersionless character, indicating the heavy effective mass and highly localization.

When the charge carrier density is below a critical value, the Fermi level will be located in the vicinity of the defect states and the hopping electrons involved in the transport are localized within the vacancy defect structure. If the gating voltage increases the charge carrier density over this threshold, the Fermi level will lift and the localized gap states will be occupied and the macroscopic transport evolves into normal band-like transport rather than hopping transport (Fig. 17c,d). The nearest-neighboring hopping transport at high temperature and variable-range hopping transport at low temperature offer an example to tailor the electronic properties and nanoelectronic applications of TMDs via vacancy defect mechanism.

Zhu et al.[206] revealed the presence of large amounts of band tail states and determined their density distribution in MoS_2 through capacitance and alternating current (AC) conductance measurements of the field effect transistors. The chemical vapor deposited monolayer MoS_2 is used as the channel semiconductor and mainly contain vacancy defects[174, 190]. The localized in-gap states from vacancy and other defects respond like traps with different time constant, giving rise to hump features in the standard capacitance-frequency curve, which is typical of the standard capacitance measurement of defects in traditional semiconductor devices[49]. Moreover, the effective electron mobility in CVD MoS_2 devices are mostly two orders of magnitude lower than the theoretical intrinsic limit, indicating severe scattering mechanism by the trap states from structural disorders.

Transport measurements of the electronic devices give a range of electron mobility 0~80$\mathrm{cm^2V^{-1}s^{-1}}$ in monolayer MoS_2 by different research groups[179, 180]. Considering the diversity of point defects, it is of significance to explore the influence of various defects on the charge carrier mobility from the perspective of phonon scattering mechanism[190]. In 2D crystals, the phonon-limited carrier mobility can be derived[207, 208] by $\mu \propto 1/(m^* E^2)$, where m^* is carrier effective mass and E is the deformation potential for the energy bands under proper cell compression and dilatation. As shown in Table 1, the effective mass for charge carriers, deformation potentials and phonon-limited carrier mobility are calculated for perfect and defective MoS_2 monolayers[190]. In the model, each defective monolayer consists of only one type of defects (either vacancy or antisite) in a 6×6 supercell, equivalent to the experimentally measured defect density 2.8×10^{13} cm^{-2} revealed by statistics. For electrons flowing in the intrinsic conduction band, the phonon-limited mobility makes little change when introducing vacancies V_S and V_{S2} into the perfect MoS_2, while decreases by almost three times when antisite defect involves. For holes in the intrinsic valence band, the mobility shows much more sensitive response to the defects—decrease by three times for S vacancies and even more for antisite defects, compared to that of perfect MoS_2 without any defects. For charge carriers transporting through defect states within the gap, the estimated mobility contribution is all quite low as <1 $cm^2V^{-1}s^{-1}$and <10 $cm^2V^{-1}s^{-1}$ for electrons and holes, respectively. This is understandable since these defect states are highly localized and in a low density in the two-dimensional lattice. In practical device transport measurements, many other factors such as contact resistance, interface bonding and carrier density will affect the overall effective mobility and lead to complexity and difficulty in distinguishing each contribution. After all, Table 1 shows that antisite defects will lower the phonon-limited carrier mobility more severely than other types of point defects. Continual effort in defect engineering is still necessary for the TMDs' applications in flexible electronics and photonics.

4.6 Foreign-atom doping engineering

Doping engineering often play a strategic role in tailoring the physical properties of semiconductors. The success of modern complementary metal oxide semiconductor (CMOS) industry is based on the artificial transformation of the silicon semiconductor into p-type and n-type through foreign atom doping such as P and B elements[49]. Nowadays, researchers have intensively investigated effective methods of equivalent chemical doping of two-dimensional layered transition metal dichalcogenides through the initial growth process in the chemical vapor deposition.

4.6.1 Chalcogenide heteroatom doping

Doping semiconducting MoS_2 can be controlled by alternating the chalcogenide specie or metal element. Gong *et al.*[209] successfully synthesized monolayer Se-doped MoS_2 with a large range of doping concentration. Through a chemical vapor deposition, the precursor MoO_3 reacts with S/Se mixing powder to form monolayer $MoS_{2(1-x)}Se_{2x}$ alloys. The atomically resolved annular dark field (ADF) image of Se-doped MoS_2 (x=0.12) is shown in Fig. 18a. This Z-contrast imaging allows for atom-by-atom chemical analysis through quantitative analysis of the ADF intensity to map the atomic distribution of Se dopants. Most hexagonal lattices preserve brighter Mo atoms and darker S_2 column, while some S_2 sites present even higher intensity than the Mo sites. This abnormal ADF intensity arises from the substitutional doping of Se atoms. For the chalcogenide sites with ADF intensity higher than normal S_2 sites, they can be classified as single substitution S+Se, which is colored in bright green in Fig. 18b. Those chalcogenide sites showing brighter than Mo sites can be seen as double substitution Se_2, highlighted in white. The color mapping in Fig. 18b demonstrate the random substitution doping of Se in monolayer MoS_2. Similar atomic distribution mapping has also reported in the $MoS_{2(1-x)}Se_{2x}$ semiconductor alloys prepared through physical vapor deposition of MoS_2 and $MoSe_2$ powder by Feng *et al.*[191].

High-level foreign atom doping should actually be considered as bandgap engineering by alloying. Li *et al.*[210] showed the redshift of the Raman vibration modes E_{2g} and A_{1g} for both Mo-Se and Mo-S bonds when the concentration of Se increases in the $MoS_{2(1-x)}Se_{2x}$ semiconductor alloy. The photoluminescence spectroscopy of this alloy measured by Mann et al.[211] further reveal the range of the band gap from 1.55 eV (pure $MoSe_2$) to 1.85 eV (pure MoS_2). The bandgap of the alloy decreases linearly with the concentration x of Se dopants, as shown in Fig. 18c. All these controllable dopings of foreign chalcogenides have illustrated practical ways for band gap engineering and will benefit the development of TMDs' optical and optoelectronic applications with gap-tunable requirements.

4.6.2 Congener metal doping

Band gap engineering can also be realized through alloying two TMDs with different metal species. Monolayer $Mo_{1-x}W_xS_2$ semiconductor alloys were also earlier reported by Chen *et al.*[212] and Dumcenco *et al.*[213]. The metal atoms in the alloyed $Mo_{1-x}W_xS_2$ are found to be in a random distribution through atom-by-atom structural and chemical analysis by transmission electron microscopy. Composition-dependent band gap emission can be tuned from 1.82 eV to 1.99 eV by photoluminescence measurements. However, this tunable band gap E_g does not display a linear relationship with the relative concentration of W (x), but shows an obvious bowing-like dependence in the region of low concentration of W atoms. In fact, the measured emission energies of $Mo_{1-x}W_xS_2$ alloy are smaller than the linear combination of the gap of MoS_2 and WS_2, and quantitatively obeys the relationship:

$$E_g(\text{alloy}) = (1-x)E_g(\text{MoS}_2) + xE_g(\text{WS}_2) - bx(1-x) \tag{1}$$

where b is the bowing parameter and the last term shows a parabolic dependence on the relative concentration x. Similar bowing-like dependence on the chemical stoichiometry has also been reported in the randomly alloyed $Mo_{1-x}W_xSe_2$ by Zhang et al.[214, 215] (Fig. 18d). This is in contrast with the previous $MoS_{2(1-x)}Se_{2x}$ alloying by different chalcogenide species with almost the same electron configuration ns^2np^4 to participate in hybrid bonding. Through DFT calculations, the composition-dependent bandgaps also show a small decrease before the turning point at x=0.3 and then rise quickly to reach the value of pure WSe_2. The bowing coefficient b fitted from experimental photoluminescence in the sulfide alloys is derived to be ~ 0.25eV in $Mo_{1-x}W_xS_2$, consistent with the DFT-derived[212] value of 0.28eV.

This bowing-like variation of the bandgaps (Fig. 18d) can be understood in terms of the molecular orbital theory. Calculations show the energy of the lowest unoccupied molecular orbital (LUMO) in $Mo_{1-x}W_xS_2$ alloy has an upward-parabolic dependence on the W concentration, in contrast with the linear relation for highest occupied molecular orbital (HOMO)[212]. Hence the gap between LUMO and HOMO then behave as a bowing curve, as shown in Fig. 18d. Further calculation shows that the projected density of states (PDOS) of W atoms is a linear increasing function of x in the HOMO, but a bowing-like function in the LUMO. Decomposition of the frontier orbitals in TMDs shows that the HOMO contribution from metal atom is mainly of d_{xy} , $d_{x^2-y^2}$ character, which is the same for both MoS_2 and WS_2. But as for LUMO, the orbitals are different as only d_{z^2} contributes in MoS_2 while d_{xy} , $d_{x^2-y^2}$, d_{z^2} contribute in WS_2. The identical orbital composition in HOMO for MoS_2 and WS_2 give rise to the HOMO energy's linear dependence on the W concentration x. Owing to different orbital composition in LUMO and higher LUMO energy level in WS_2, W atoms make less contribution to the LUMO, leading to its energy level smaller than the expected linear increasing with the W concentration x.

It is interesting and encouraging that a few recent reports find that deep levels introduced by intrinsic Se vacancies can be supressed in the slightly-doped $Mo_{1-x}W_xSe_2$ system[216]. As a result, the photoluminescence get significantly enhanced and unexpectedly the n-type conduction is turned into p-type when the isoelectronic tungsten is doped with a low content x in the $MoSe_2$ monolayer[217]. All the alloy engineering demonstrated above offers a strategic route to tailor the functionalities of TMDs for electronics and optoelectronics applications.

4.6.3 Other heteroatom doping

MoS_2 is an inherent n-type semiconductor and the donor is attributed to the intrinsic vacancies[194]. Fang *et al.*[187] doped MoS_2 by K vapor and observed the n-type conductance of MoS_2. The electron sheet density can reach as high as 1×10^{13}cm^{-2}, indicating a degenerate n-doping of K. In this heavy doping, K atoms are adsorbed on the surface, similar to the case in graphene. Kiriya *et al.*[218] also demonstrated n-doping of MoS_2 by charge transfer from molecule adsorption of benzyl viologen which is stable in the atmosphere on the surface.

Degenerate doping of MoS_2 at metal junctions can decrease the contact resistance in FETs by more than three times.

The transition from intrinsic n-type conduction to p-type conduction in MoS_2 through doping engineering is a prerequisite for the applications in charge-splitting p-n junctions and complementary or bipolar electronic devices. Compared to traditional p-type doping by surface adsorption or intercalation, substitutional doping by proper acceptor metals will be a more reliable way due to the protection of covalent bonding within the monolayer. Suh *et al.*[186] prepared Nb-doped MoS_2 through standard vapor transport with iodine as the transport agent, where high-purity Mo, S and Nb powders are used as the precursors. Atomically thin nanosheet was obtained by mechanical exfoliation of the as-grown 0.5% Nb-doped MoS_2 bulk material. The Hall measurement of the nanosheets shows a hole concentration $\sim 1.8\times10^{14}cm^{-2}$, indicating a highly degenerate p-type doping in MoS_2, which was also illustrated by the transport characteristic of its field effect transistor.

Direct atomic-scale imaging of transition metal doped in the atomically thin TMDs has so far rarely been reported. Zhang *et al.*[219] demonstrated Mn can be doped in monolayer MoS_2 supported on graphene through CVD growth, while no detectable Mn dopants are observed in MoS_2 if grown on other substrates such as SiO_2 and sapphire. Gao *et al.*[220] synthesized Nb-doped WS_2 through in-situ CVD growth where the dopants originate from the $NbCl_5$ precursor. Through quantitative ADF intensity analysis of the atomically resolved transmission electron microscopy, dopants Nb were unambiguously visualized in a random substitution of W lattices. Similar to the Nb doping of MoS_2 by Suh *et al.*, the Nb atom is an acceptor in WS_2 but does not induce any midgap states according to the theoretical calculation.

4.7 Defect engineering for catalysis

4.7.1 Edge sites and phase transition

Traditionally, nano-sized MoS_2 is widely used as an effective catalyst in the hydrodesulfurization[154] (HDS) in the oil refining industry. In this HDS application, the active sites for the catalysing reactions are proved to be the unsaturated edge structures of nano-MoS_2. Recently, MoS_2 has been demonstrated as a promising and effective catalyst[221] alternative to the noble metal Pt in the hydrogen evolution reaction (HER) due to its low cost, high abundance and reactivity[222-224]. The active edge sites of MoS_2 nanoparticles were early identified by Jaramillo *et al.* through scanning tunnelling microscopy and the electrocatalytic HER activity enhancement scales linearly with the number of edge sites[225]. Thereafter, enormous efforts have been made in maximizing the active edge sites of 2H-MoS_2 to optimize the catalysis efficiency in HER.

Xie *et al.*[226] developed a MoS_2 catalyst with good crystalline quality as well as abundant edge sites. Controllable defect engineering by extra thiourea was employed as one precursor to confine the size of MoS_2 nanocrystallites in the initial nucleation growth and thus more edge sites would be formed. The electrochemical HER test demonstrated a small onset potential of 120mV and a low Tafel slope of 50mV/dec which were both much better than that found in defect-free nanosheets, bulk MoS_2 and thicker nanosheet assembly. In addition, the negligible current loss after 3000-cycle voltammograms tests confirmed the good long-term stability, in contrast with the amorphous MoS_2 catalyst[227-229] despite its high activity. Kibsgaard *et al.*[223] engineered the surface structure of atomically thin MoS_2 through an ordered double-gyroid bicontinuous network of nanopores with a high surface curvature. In this porous structure, the large-area extension of the inert basal plane of MoS_2 was hindered and a large portion of edge sites were exposed, giving rise to much enhanced HER catalytic activity. Ye *et al.*[230] suggested another way to create more active edge sites inside the basal plane by oxygen plasma and hydrogen etching. A large number of cracks or triangular nanoholes will emerge within the pristine monolayer MoS_2, introducing a high density of edge states across the whole monolayer. Then a significant improvement of the electrocatalytic activity is observed. Xie *et al.* proposed oxygen incorporation with controllable disorder engineering[231] as a new strategy for the increase of both conductivity and edge sites. The incorporation of oxygen dopants effectively modified the electronic structure of the disordered 2H MoS_2 nanosheets and thus improve the electronic conductivity, which promotes the charge flow between the electrodes and active sites and boost the catalytic performance with an onset overpotential of 120mV and large cathodic current density.

Phase transition is the second route for increasing the HER activity[232, 233]. Lukowski *et al.*[234] and Voiry *et al.*[235] reported the huge improvement of the HER Tafel slope to 40mV/dec catalysed by chemically exfoliated metallic 1T-MoS_2 through lithium ion intercalation. The transition from semiconducting to metallic properties of 1T-MoS_2 overcomes the limitation of the inefficient charge transfer kinetics in 2H MoS_2. This metallic phase greatly improves the electric contact resistance[236] and benefits in the charge injection from the electrode and charge transport to the catalytically active sites involved in the hydrogen evolution. Also, the remarkably reduced hydrogen adsorption Gibbs free energy (ΔG_H) results in the catalytic activity enhancement[222].

4.7.2 Point defects

Apart from the phase control and edge sites engineering, intrinsic point defects inside the inert basal plane of MoS_2 also hold important potential in the hydrogen evolution. Li *et al.*[237] reported the successful chemical modification of the catalytically inert basal plane of 2H MoS_2 by vacancy defect creation and the introduction of strain array. The sulfur vacancies in the monolayer are produced by controllable argon plasma treatment, as evidenced by PL measurements discussed previously. Atomically-resolved ADF image shown in Fig. 19a reveal the random distribution of sulfur vacancies induced by plasma ionic bombardment and no Mo sublattices were found to be damaged. Periodic lattice strain is introduced by depositing MoS_2 monolayer onto a patterned support of the array of Au nanocones, as shown by the inset of Fig. 19b. Local electronic structure of sulfur vacancies explored by scanning tunnelling spectroscopy (STS) exhibits an evident peak within the bandgap of the monolayer (Fig. 19b). The calculated *d*-orbital projected density of states confirms the presence of an in-gap state induced by vacancies. The localized gap states nearby Fermi level are believed to be responsible for the hydrogen adsorption and reaction.

Activation of the inert basal plane of 2H-MoS_2 monolayer by increasing active vacancy-site density allows the tuning of the hydrogen adsorption free energy (ΔG_H) which fundamentally determines the catalytic performance. The maximum reaction rate can be achieved only when the Gibbs free energy of hydrogen adsorption on a catalyst is close to zero, on the basis of the Sabatier principle[238]. As the density of S vacancies increase to over 3% (of all sulfur atoms in the monolayer), the Gibbs free energy decreases significantly from over 2eV to less than 0.2eV (Fig. 19c). Compared to the effect due to S vacancies, introduction of lattice strain decreases the free energy ΔG_H much more mildly. Theoretical simulation shows an optimal combination of 11% S vacancies and 1% strain leads to a free energy ΔG_H =0 eV. This also maintains the balance between high density of active sites and the structural integrity. The average density of sulfur vacancies in Fig. 19a is equivalent to 11.3%, typical of the optimal experimental choice for HER.

The polarization curves by linear sweep voltammogram in Fig. 19d show the HER catalytic activity of 2H MoS_2 monolayer. Compared to the almost noncatalytic Au substrate, the monolayer with only strain has slight activity and the monolayer with only vacancies presents increased activity. Noble-metal Pt electrode display the highest activity, while the monolayer with both vacancies and strain has the most improved catalytic performance achieved among all non-precious nanocarbon and MoS_2 catalysts. The combination of vacancies and strain give rise to an enhanced activity with an onset overpotential of 170mV and low Tafel slope about 60 mV/dec. As shown in Fig. 19e, vacancies contribute much more to the turnover frequency (TOF) than the strain. The strained monolayer with vacancies exhibits a TOF per S vacancy of 0.31 s^{-1}, namely 0.31 H_2 molecules per second at 0 V versus reversible hydrogen electrode, a value even higher than that of the 1T metallic[235] MoS_2 and 2H nanocrystallites[239] with plentiful edge sites (0.02 s^{-1}).

Further HER kinetics study by Li *et al.*[240] using scanning electrochemical microscopy illustrates the charge transfer rate of strained vacancy is 4 times larger than that of unstrained vacancy in monolayer MoS_2. The elastic strain greatly promotes the charge transfer from the active vacancy sites. These systematic and comparative researches by Li *et al.* successfully demonstrated a useful strategy of atomic-scale defect engineering for the electrochemical catalytic applications of MoS_2 in HER.

Voiry *et al.*[236] improved the electrical coupling between the substrate and the MoS_2 nanosheet catalyst to greatly enhance the charge injection and transport by a phase engineered low-resistance contact. The efficient charge injection and the catalytically-active unsaturated Mo sites around S vacancy defects lead to an excellent increase in the HER activity with a small onset overpotential of -100mV and Tafel slope of 50mV/decade. And the turnover frequency are even comparable to the state-of-the-art performance of metallic edges dominated MoS_2 nanoislands[225].

Ouyang *et al.*[241] systematically assessed the HER catalytic activity of different intrinsic point defects within the inert 2H-MoS_2 monolayer from the first-principles calculation. Among all the possible vacancies and antisite defects, only V_S, V_{MoS3} and Mo_{S2} can be the active sites to activate the inert basal plane of 2H-MoS_2 monolayers and greatly improve the HER catalysis performance. According to Sabatier principle[238], when the Gibbs free energy of hydrogen adsorption (ΔG_H) gets smaller and down to zero in value, then the overall HER reaction can reach its optimal condition with the maximum rate. When the free energy ΔG_H increases, a higher reaction barrier will emerge and lead to low turnover frequency and low reaction rate. Compared to the ΔG_H of 1.92 eV for H adsorption on the perfect MoS_2, the calculated ΔG_H for antisites S_{Mo} and $S2_{Mo}$ are both very positive value larger than 1 eV, indicating the antisites' weak interaction with H atom for the proton-electron transfer in the electrochemical hydrogen adsorption (Volmer reaction[242]). While vacancies V_S, V_{MoS3}, antisite Mo_{S2} has free energy of -0.06 eV, -0.13 eV and 0.09 eV, respectively, comparable to the metallic edges ($\Delta G_H = 0.08$ eV) and Pt catalyst ($\Delta G_H = -0.09$ eV). The further calculation show that these three point defects also have very small H desorption Gibbs free energy close to 0 eV in Heyrovsky reaction and Tafel reaction[242]. This indicates the highly catalytic activity of these point defects in the overall HER and they could greatly help to activate the inert basal plane of MoS_2 if proper engineering of designated defects is realized to increase the density of these catalytic centers within the monolayer.

5. Conclusive Remarks and Prospects

Two-dimensional materials from graphene, hexagonal BN to transition metal dichalcogenides continue to attract research interest since they provide an ideal platform for novel physics exploration and materials applications. The exploration in physics and chemistry of these 2D crystals has been proceeding rapidly towards their large scale applications. However, compared to the maturing modern electronics or optoelectronics based on silicon and other traditional semiconductors, the research on 2D materials is still at its early stage and much more exploration of the structure-property correlation is necessary to improve the functionalities or uncover new potentials, as illustrated in the sections above.

5.1 Common challenges of interest

The microscopic growth mechanism of graphene-like 2D materials is crucial to the formation of the crystals and intrinsic defects and even to the controllable defect engineering of great interest. It also remains a common and great challenge for the whole 2D society even in the simplest graphene system. The diversity of atomic defects in TMDs originates from the binary elements and more complicated precursor decomposition/reduction reaction through intermediate products, compared to the involvement of only C (possible H) in the graphene growth. However, the exploration of the fundamental growth mechanism down to atomic scale is still quite limited until now[243-245], awaiting more in-situ TEM researches. Another challenge is the defect engineering within or after the sample growth. Morphology control, one way to engineering the defects macroscopically, can be realized by changing the type and flux of the atmosphere and substrate, for instance, in the CVD growth of graphene[246]. Recent STM experiment[88] has reported hydrogen adsorption on graphene inducing the long-range magnetism. While in the TMDs system, less has been discovered in the defects controlling through growth atmosphere, except the post-growth plasma treatment inducing vacancies described in sections above.

5.2 Defects-functionalities

Point defects such as vacancies, adatoms, antisites and dopant impurities are local structural disorders and form a distinctive chemical and electronic environment in the two-dimensional lattices. These atomic-scale defects are either intrinsically formed or unintentionally/purposely introduced, but presenting significant effects on the physical or chemical properties of many studied two-dimensional crystals. The modulation of the electronic structure lies at the heart of the defect engineering, which can be probed locally by high-resolution transmission electron microscopy with electron energy-loss spectroscopy or nanophotonics, or visualized macroscopically by electrical transport, PL, magnetic measurement and heterogeneous catalysis.

The aberration corrected TEM facilitates us in the direct imaging of the defects' structure with rich information in coordination and symmetry. STEM-EELS spectrum imaging further allows us to perform accurate elemental analysis of the single-atom defects to determine the chemical shift and bonding states. ELNES in the core loss spectrum has been successfully utilized to detect unoccupied electronic states above Fermi level in the edge C atoms, B, N and Si dopant atoms in monolayer graphene, and also in the case of vacancies in monolayer BN. ELXELFS in core loss has also provided a paradigm to identify the dopant's coordination and bonding states in the Si-doped graphene. These EELS measurements offer indirect measurement of the three-dimensional structure of the single point defects studied, as such they are a good supplement of the inherent two-dimensional imaging in TEM together with rich electronic properties. Valence electron EELS fine structure was also used to reveal the local electronic structure of impurity-doped BN and to demonstrate the potential of the surface plasmon enhancement down to quasi-atom scale induced by Si dopants in graphene. The methodology of high-resolution TEM combined with the electron energy-loss spectroscopy offers great opportunities to explore the quantum chemistry of defects with single atom accuracy in the two-dimensional crystal systems.

As for the macroscopic electric transport of graphene and MoS_2, the intrinsic vacancy/antisite defects contribute localized states and become charge carrier traps, and thus the effective carrier mobility is decreased. From this perspective, the vacancy/antisite defects are detrimental factors for microelectronic applications of 2D materials in field effect transistors. Minimizing the content of these intrinsic defects can be a useful approach to avoid these carrier traps. Special treatment should be taken to decrease the defects' formation during and after the sample growth. It has also been shown that the thermal annealing of MoS_2 in the sulfur flow effectively increase the electron mobility due to the annihilation of intrinsic sulfur vacancies. Interesting phenomenon such as low-temperature hopping transport induced by localized defect states has also been observed in defective MoS_2. For pn-junction power devices and logic applications in CMOS, the n-to-p transformation through chemical doping is necessary for both graphene and MoS_2. Doping B, N into graphene and K, Nb into MoS_2 has been shown to successfully introduce donors or acceptors. Tremendous efforts will be needed to follow up on these initial chemical decoration engineering to open up the inspiring era of 2D microelectronics.

The optical properties of TMD MX_2 (M=Mo, W; X=S, Se) has been demonstrated to be effectively modified by defect engineering such as chemical doping with congeneric heteroatom and vacancies creation through controllable plasma etching. The former strategy leads to composition-dependent tunable gap, while the latter leads to new exciton emission by introducing localized states within the intrinsic gap. It is quite encouraging that the exciton emission in MoS_2 and WS_2 bound to vacancy defects within ~0.1eV below the K-K valley exciton (free exciton) coincides well with the recent ultrabright single-photon emitter found in WSe_2. Further defect engineering will inspire more research on rich quantum photon emission in more TMDs and BN. However, the accurate correlation of the quantum emission and defect structure is still in a very initial status, and it remains a challenge to map out the nanophotonic diversity of the defect-emission. We believe that the additional knowledge will boost the development of quantum technologies like quantum information processing, particularly if the stimuli can also be scalably engineered into the 2D crystal platform.

Nanomagnetism was also studied intensively via theoretical calculation and limited experimental measurement. Vacancies, H and F adatom turns nonmagnetic graphene into paramagnetic material. In the MoS_2 system, substitutional doping of Mn, Fe, Co etc. and antisite defect Mo_S engineering through proper physical vapor deposition could make MoS_2 a promising two-dimensional dilute magnetic semiconductor. The current barrier to reach the prediction lies in the difficulty in the experimental doping engineering.

Macroscopic catalysis benefits greatly from the defect engineering of 2D materials. Doped graphene and defective MoS_2 has shown greatly improved electrocatalytic activities in oxygen reduction reaction (ORR) and hydrogen evolution reaction (HER), respectively. In TMDs system, the catalysis behavior mainly stems from the localized *d*-band for both edges and vacancies where bonding of the Mo atoms are both unsaturated. Hence, the nanomagnetism through chemical doping or antisite defects is often correlated with the enhanced single-atom catalysis effects.

5.3 Prospects

In terms of the future electron microscopy of 2D materials, we propose several prospects or issues related with the local structure, opto/electronic, and magnetic properties of atomic defects. Firstly, we may combine the ADF-STEM imaging and cathodoluminescence (CL) to uncover the mechanism of single-photon emitter and to accomplish the map of the defect-photonics diversity in TMDs. Secondly, we can further capture the dynamic evolution of defects or surfaces or atomic-scale sample growth mechanism through 4D TEM imaging, and improve the irradiation damage mechanism more systematically, with the inclusion of radiolysis and chemical etching. Thirdly, we may fully utilize the resolving ability of C_c+C_s corrected TEM to reveal the possible 3D structure of the Jahn-Teller distortion of defects. Fourthly, we might also exploit the defects' magnetism through STEM-EMCD, although the current theory and technique development is still a challenge.

In summary, we review the nanophysics of point defects in 2D crystals including local structure and associated electronic states as probed by electron microscopy and EELS at single atom level, together with their effects on the electrical transport, electronic, optical, magnetic and catalytic properties. These results suggest different strategies can be taken when developing practical applications: 1) reducing intrinsic defects in sample synthesis or by post-growth treatment is crucial to the transport and optoelectronics; 2) introducing defects through chemical doping or defect engineering will benefit in p-n-junction involved logic devices (bipolar transistor and CMOS), nanomagnetism and catalysis decoration and in discovery of the novel 2D physics such as single photon emitter. Last but not least is the controllable and scalable sample growth with application-oriented defect or chemical engineering, which remains challenging but hopeful to take 2D family onto ground with breakthroughs both in applications and in basic 2D physics exploration.

6. Acknowledgements

This work was financially supported by the National Basic Research Program of China (Grant No. 2014CB932500 and No. 2015CB21004), and the National Science Foundation of China (Grant No. 51472215,No. 51222202, No. 11234011 and No. 11327901). J.Y. acknowledges the EPSRC (UK) funding EP/G070326 and EP/J022098, and supports from Pao Yu-Kong International Foundation for a Chair Professorship in Zhejiang University.

Received: ((will be filled in by the editorial staff))
Revised: ((will be filled in by the editorial staff))
Published online: ((will be filled in by the editorial staff))

References

[1] K. S. Novoselov, A. K. Geim, S. V. Morozov, D. Jiang, Y. Zhang, S. V. Dubonos, I. V. Grigorieva, A. A. Firsov, Science 2004, 306, 666.
[2] A. H. Castro Neto, N. M. R. Peres, K. S. Novoselov, A. K. Geim, Rev. Mod. Phys. 2009, 81, 109.

[3] K. S. Novoselov, S. V. Morozov, T. M. G. Mohinddin, L. A. Ponomarenko, D. C. Elias, R. Yang, I. I. Barbolina, P. Blake, T. J. Booth, D. Jiang, J. Giesbers, E. W. Hill, A. K. Geim, Phys. Status Solidi B 2007, 244, 4106.

[4] M. H. Gass, U. Bangert, A. L. Bleloch, P. Wang, R. R. Nair, A. K. Geim, Nat. Nanotechnol. 2008, 3, 676.

[5] A. K. Geim, K. S. Novoselov, Nat. Mater. 2007, 6, 183.

[6] K. S. Novoselov, Z. Jiang, Y. Zhang, S. V. Morozov, H. L. Stormer, U. Zeitler, J. C. Maan, G. S. Boebinger, P. Kim, A. K. Geim, Science 2007, 315, 1379.

[7] J. C. Meyer, A. K. Geim, M. I. Katsnelson, K. S. Novoselov, T. J. Booth, S. Roth, Nature 2007, 446, 60.

[8] K. S. Novoselov, A. K. Geim, S. V. Morozov, D. Jiang, M. I. Katsnelson, I. V. Grigorieva, S. V. Dubonos, A. A. Firsov, Nature 2005, 438, 197.

[9] Y. B. Zhang, Y. W. Tan, H. L. Stormer, P. Kim, Nature 2005, 438, 201.

[10] X. S. Li, W. W. Cai, J. H. An, S. Kim, J. Nah, D. X. Yang, R. Piner, A. Velamakanni, I. Jung, E. Tutuc, S. K. Banerjee, L. Colombo, R. S. Ruoff, Science 2009, 324, 1312.

[11] K. Watanabe, T. Taniguchi, H. Kanda, Nat. Mater. 2004, 3, 404.

[12] C. Jin, F. Lin, K. Suenaga, S. Iijima, Phys. Rev. Lett. 2009, 102, 195505.

[13] A. Splendiani, L. Sun, Y. B. Zhang, T. S. Li, J. Kim, C. Y. Chim, G. Galli, F. Wang, Nano Lett. 2010, 10, 1271.

[14] L. K. Li, Y. J. Yu, G. J. Ye, Q. Q. Ge, X. D. Ou, H. Wu, D. L. Feng, X. H. Chen, Y. B. Zhang, Nat. Nanotechnol. 2014, 9, 372.

[15] W. L. Lu, H. Y. Nan, J. H. Hong, Y. M. Chen, C. Zhu, Z. Liang, X. Y. Ma, Z. H. Ni, C. H. Jin, Z. Zhang, Nano Res. 2014, 7, 853.

[16] L. K. Li, G. J. Ye, V. Tran, R. X. Fei, G. R. Chen, H. C. Wang, J. Wang, K. Watanabe, T. Taniguchi, L. Yang, X. H. Chen, Y. B. Zhang, Nat. Nanotechnol. 2015, 10, 608.

[17] K. S. Novoselov, D. Jiang, F. Schedin, T. J. Booth, V. V. Khotkevich, S. V. Morozov, A. K. Geim, P. Natl. Acad. Sci. USA 2005, 102, 10451.

[18] A. K. Geim, I. V. Grigorieva, Nature 2013, 499, 419.

[19] R. Chau, B. Doyle, S. Datta, J. Kavalieros, K. Zhang, Nat. Mater. 2007, 6, 810.

[20] M. Lundstrom, Science 2003, 299, 210.

[21] A. D. Franklin, Science 2015, 349, aab2750.

[22] T. N. Theis, P. M. Solomon, Science 2010, 327, 1600.

[23] S. B. Desai, S. R. Madhvapathy, A. B. Sachid, J. P. Llinas, Q. Wang, G. H. Ahn, G. Pitner, M. J. Kim, J. Bokor, C. Hu, H.-S. P. Wong, A. Javey, Science 2016, 354, 99.

[24] C. Ataca, H. Sahin, S. Ciraci, J. Phys. Chem. C 2012, 116, 8983.

[25] M. S. Shur, *GaAs devices and circuits*, Springer Science & Business Media, New York 2013.

[26] S. Nakamura, Science 1998, 281, 956.

[27] S. Nakamura, S. Pearton, G. Fasol, *The blue laser diode: the complete story*, Springer Science & Business Media, 2013.

[28] B. Radisavljevic, A. Radenovic, J. Brivio, V. Giacometti, A. Kis, Nat. Nanotechnol. 2011, 6, 147.

[29] L. Britnell, R. M. Ribeiro, A. Eckmann, R. Jalil, B. D. Belle, A. Mishchenko, Y. J. Kim, R. V. Gorbachev, T. Georgiou, S. V. Morozov, A. N. Grigorenko, A. K. Geim, C. Casiraghi, A. H. Castro Neto, K. S. Novoselov, Science 2013, 340, 1311.

[30] T. Georgiou, R. Jalil, B. D. Belle, L. Britnell, R. V. Gorbachev, S. V. Morozov, Y. J. Kim, A. Gholinia, S. J. Haigh, O. Makarovsky, L. Eaves, L. A. Ponomarenko, A. K. Geim, K. S. Novoselov, A. Mishchenko, Nat. Nanotechnol. 2013, 8, 100.

[31] C. J. Chen, *Introduction to scanning tunneling microscopy*, Vol. 2, Oxford University Press New York, 1993.

[32] R. Wiesendanger, *Scanning probe microscopy and spectroscopy: methods and applications*, Cambridge University Press, 1994.

[33] D. A. Muller, L. F. Kourkoutis, M. Murfitt, J. H. Song, H. Y. Hwang, J. Silcox, N. Dellby, O. L. Krivanek, Science 2008, 319, 1073.

[34] O. L. Krivanek, G. J. Corbin, N. Dellby, B. F. Elston, R. J. Keyse, M. F. Murfitt, C. S. Own, Z. S. Szilagyi, J. W. Woodruff, Ultramicroscopy 2008, 108, 179.

[35] P. E. Batson, N. Dellby, O. L. Krivanek, Nature 2002, 418, 617.

[36] P. D. Nellist, M. F. Chisholm, N. Dellby, O. L. Krivanek, M. F. Murfitt, Z. S. Szilagyi, A. R. Lupini, A. Borisevich, W. H. Sides, S. J. Pennycook, Science 2004, 305, 1741.

[37] S. J. P. a. P. D. Nellist, *Scanning Transmission Electron Microscopy-Imaging and Analysis*, Springer, 2011.

[38] R. F. Egerton, *Electron Energy-Loss Spectroscopy in the Electron Microscope*, Plenum Press, New York 1996.

[39] O. L. Krivanek, M. F. Chisholm, V. Nicolosi, T. J. Pennycook, G. J. Corbin, N. Dellby, M. F. Murfitt, C. S. Own, Z. S. Szilagyi, M. P. Oxley, S. T. Pantelides, S. J. Pennycook, Nature 2010, 464, 571.

[40] H. Sawada, T. Sasaki, F. Hosokawa, K. Suenaga, Phys. Rev. Lett. 2015, 114, 166102.

[41] http://www.salve-project.de/newspress/SALVE-CC-correction-realized.html#refresource; http://www.salve-project.de/home.html.

[42] M. Linck, P. Hartel, S. Uhlemann, F. Kahl, H. Müller, J. Zach, M. Haider, M. Niestadt, M. Bischoff, J. Biskupek, Phys. Rev. Lett. 2016, 117, 076101.

[43] T. Eberlein, U. Bangert, R. R. Nair, R. Jones, M. Gass, A. L. Bleloch, K. S. Novoselov, A. Geim, P. R. Briddon, Phys. Rev. B 2008, 77, 233406.

[44] J. A. Scholl, A. L. Koh, J. A. Dionne, Nature 2012, 483, 421.

[45] B. Rafferty, L. M. Brown, Phys. Rev. B 1998, 58, 10326.

[46] L. Gu, V. Srot, W. Sigle, C. Koch, P. van Aken, F. Scholz, S. B. Thapa, C. Kirchner, M. Jetter, M. Ruehle, Phys. Rev. B 2007, 75, 195214.

[47] H. Tan, S. Turner, E. Yücelen, J. Verbeeck, G. Van Tendeloo, Phys. Rev. Lett. 2011, 107, 107602.

[48] L. R. a. H. Kohl, *Transmission Electron Microscopy-Physics of Image Formation*, Springer, 2008.

[49] S. M. Sze, K. K. Ng, *Physics of Semiconductor Devices*, John Wiley & Sons, Inc., New Jersey 2007.

[50] F. Banhart, J. Kotakoski, A. V. Krasheninnikov, ACS Nano 2011, 5, 26.

[51] L. Liu, M. Qing, Y. Wang, S. Chen, J. Mater. Sci. Technol. 2015, 31, 599.

[52] Q. Peng, J. Crean, A. K. Dearden, C. Huang, X. Wen, S. P. Bordas, S. De, Mod. Phys. Lett. B 2013, 27, 1330017.

[53] Z. Lin, B. R. Carvalho, E. Kahn, R. Lv, R. Rao, H. Terrones, M. A. Pimenta, M. Terrones, 2D Mater. 2016, 3, 022002.

[54] H. I. Rasool, C. Ophus, A. Zettl, Adv. Mater. 2015, 27, 5771.

[55] A. K. Geim, Science 2009, 324, 1530.

[56] K. I. Bolotin, K. J. Sikes, Z. Jiang, M. Klima, G. Fudenberg, J. Hone, P. Kim, H. L. Stormer, Solid State Commun. 2008, 146, 351.

[57] I. W. Frank, D. M. Tanenbaum, A. M. Van der Zande, P. L. McEuen, J. Vac. Sci. Technol. B 2007, 25, 2558.

[58] A. A. Balandin, S. Ghosh, W. Z. Bao, I. Calizo, D. Teweldebrhan, F. Miao, C. N. Lau, Nano Lett. 2008, 8, 902.

[59] A. A. Balandin, Nat. Mater. 2011, 10, 569.

[60] J. H. Seol, I. Jo, A. L. Moore, L. Lindsay, Z. H. Aitken, M. T. Pettes, X. S. Li, Z. Yao, R. Huang, D. Broido, N. Mingo, R. S. Ruoff, L. Shi, Science 2010, 328, 213.

[61] G. Eda, G. Fanchini, M. Chhowalla, Nat. Nanotechnol. 2008, 3, 270.

[62] S. Stankovich, D. A. Dikin, R. D. Piner, K. A. Kohlhaas, A. Kleinhammes, Y. Jia, Y. Wu, S. T. Nguyen, R. S. Ruoff, Carbon 2007, 45, 1558.

[63] F. Hao, D. N. Fang, Z. P. Xu, Appl. Phys. Lett. 2011, 99, 041901.

[64] K. Suenaga, M. Koshino, Nature 2010, 468, 1088.

[65] J. Yuan, L. M. Brown, Micron 2000, 31, 515.

[66] N. Fujita, P. J. Hasnip, M. I. J. Probert, J. Yuan, J. Phys. Condens. Mat. 2015, 27, 305301.

[67] J. Lu, S.-P. Gao, J. Yuan, Ultramicroscopy 2012, 112, 61.

[68] J. Homola, S. S. Yee, G. Gauglitz, Sensor. Actuat. B-Chem. 1999, 54, 3.

[69] S. Lal, S. Link, N. J. Halas, Nat. Photonics 2007, 1, 641.

[70] S. A. Maier, P. G. Kik, H. A. Atwater, S. Meltzer, E. Harel, B. E. Koel, A. A. G. Requicha, Nat. Mater. 2003, 2, 229.

[71] J. Nelayah, M. Kociak, O. Stephan, F. J. G. de Abajo, M. Tence, L. Henrard, D. Taverna, I. Pastoriza-Santos, L. M. Liz-Marzan, C. Colliex, Nat. Phys. 2007, 3, 348.

[72] F. J. G. de Abajo, Nature 2012, 483, 417.

[73] Z. Jacob, V. M. Shalaev, Science 2011, 334, 463.

[74] W. Zhou, J. Lee, J. Nanda, S. T. Pantelides, S. J. Pennycook, J.-C. Idrobo, Nat. Nanotechnol. 2012, 7, 161.

[75] J. Z. Zhang, C. Noguez, Plasmonics 2008, 3, 127.

[76] D. E. Chang, A. S. Sorensen, E. A. Demler, M. D. Lukin, Nat. Phys. 2007, 3, 807.

[77] W. Zhou, M. D. Kapetanakis, M. P. Prange, S. T. Pantelides, S. J. Pennycook, J.-C. Idrobo, Phys. Rev. Lett. 2012, 109, 206803.

[78] J. Lee, W. Zhou, S. J. Pennycook, J. C. Idrobo, S. T. Pantelides, Nat. Commun. 2013, 4, 1650.

[79] Q. M. Ramasse, C. R. Seabourne, D.-M. Kepaptsoglou, R. Zan, U. Bangert, A. J. Scott, Nano Lett. 2013, 13, 4989.

[80] L. Y. Zhao, R. He, K. T. Rim, T. Schiros, K. S. Kim, H. Zhou, C. Gutierrez, S. P. Chockalingam, C. J. Arguello, L. Palova, D. Nordlund, M. S. Hybertsen, D. R. Reichman, T. F. Heinz, P. Kim, A. Pinczuk, G. W. Flynn, A. N. Pasupathy, Science 2011, 333, 999.

[81] A. Lherbier, A. R. Botello-Mendez, J. C. Charlier, Nano Lett. 2013, 13, 1446.

[82] J. C. Meyer, S. Kurasch, H. J. Park, V. Skakalova, D. Kunzel, A. Gross, A. Chuvilin, G. Algara-Siller, S. Roth, T. Iwasaki, U. Starke, J. H. Smet, U. Kaiser, Nat. Mater. 2011, 10, 209.

[83] Y. Wang, Y. Huang, Y. Song, X. Y. Zhang, Y. F. Ma, J. J. Liang, Y. S. Chen, Nano Lett. 2009, 9, 220.

[84] M. A. H. Vozmediano, M. P. Lopez-Sancho, T. Stauber, F. Guinea, Phys. Rev. B 2005, 72, 155121.

[85] K. Nomura, A. H. MacDonald, Phys. Rev. Lett. 2006, 96, 256602.

[86] O. V. Yazyev, L. Helm, Phys. Rev. B 2007, 75, 125408.

[87] C. K. Jannik C. Meyer, R. Erni, Marta D. Rosse, M. F. Crommie, and A. Zettl, Nano Lett. 2008, 8, 3582.

[88] H. González-Herrero, J. M. Gómez-Rodríguez, P. Mallet, M. Moaied, J. J. Palacios, C. Salgado, M. M. Ugeda, J.-Y. Veuillen, F. Yndurain, I. Brihuega, Science 2016, 352, 437.

[89] Y.-C. Lin, P.-Y. Teng, P.-W. Chiu, K. Suenaga, Phys. Rev. Lett. 2015, 115, 206803.

[90] A. Krasheninnikov, P. Lehtinen, A. S. Foster, P. Pyykkö, R. M. Nieminen, Phys. Rev. Lett. 2009, 102, 126807.

[91] H. S. S. R. Matte, K. S. Subrahmanyam, C. N. R. Rao, J. Phys. Chem. C 2009, 113, 9982.

[92] M. Sepioni, R. R. Nair, S. Rablen, J. Narayanan, F. Tuna, R. Winpenny, A. K. Geim, I. V. Grigorieva, Phys. Rev. Lett. 2010, 105, 207205.

[93] R. R. Nair, M. Sepioni, I. L. Tsai, O. Lehtinen, J. Keinonen, A. V. Krasheninnikov, T. Thomson, A. K. Geim, I. V. Grigorieva, Nat. Phys. 2012, 8, 199.

[94] X. K. Kong, C. L. Chen, Q. W. Chen, Chem. Soc. Rev. 2014, 43, 2841.

[95] D. S. Geng, Y. Chen, Y. G. Chen, Y. L. Li, R. Y. Li, X. L. Sun, S. Y. Ye, S. Knights, Energ. Environ. Sci. 2011, 4, 760.

[96] J. Greeley, I. E. L. Stephens, A. S. Bondarenko, T. P. Johansson, H. A. Hansen, T. F. Jaramillo, J. Rossmeisl, I. Chorkendorff, J. K. Norskov, Nat. Chem. 2009, 1, 552.

[97] J. T. Zhang, Z. H. Zhao, Z. H. Xia, L. M. Dai, Nat. Nanotechnol. 2015, 10, 444.

[98] Y. Ito, W. T. Cong, T. Fujita, Z. Tang, M. W. Chen, Angew. Chem. Int. Edit. 2015, 54, 2131.

[99] Y. Zheng, Y. Jiao, Y. H. Zhu, L. H. Li, Y. Han, Y. Chen, A. J. Du, M. Jaroniec, S. Z. Qiao, Nat. Commun. 2014, 5, 3783.

[100] L. S. Panchokarla, K. S. Subrahmanyam, S. K. Saha, A. Govindaraj, H. R. Krishnamurthy, U. V. Waghmare, C. N. R. Rao, Adv. Mater. 2009, 21, 4726.

[101] Z. H. Sheng, H. L. Gao, W. J. Bao, F. B. Wang, X. H. Xia, J. Mater. Chem. 2012, 22, 390.

[102] X. K. Kong, Q. W. Chen, Z. Y. Sun, Chemphyschem 2013, 14, 514.

[103] P. Wang, Z. K. Wang, L. X. Jia, Z. L. Xiao, Phys. Chem. Chem. Phys. 2009, 11, 2730.

[104] J. C. Bai, Q. Q. Zhu, Z. X. Lv, H. Z. Dong, J. H. Yu, L. F. Dong, Int. J. Hydrogen Energ. 2013, 38, 1413.

[105] D. C. Wei, Y. Q. Liu, Y. Wang, H. L. Zhang, L. P. Huang, G. Yu, Nano Lett. 2009, 9, 1752.

[106]D. H. Deng, X. L. Pan, L. A. Yu, Y. Cui, Y. P. Jiang, J. Qi, W. X. Li, Q. A. Fu, X. C. Ma, Q. K. Xue, G. Q. Sun, X. H. Bao, Chem. Mater. 2011, 23, 1188.

[107] N. Li, Z. Y. Wang, K. K. Zhao, Z. J. Shi, Z. N. Gu, S. K. Xu, Carbon 2010, 48, 255.

[108] L. F. Lai, J. R. Potts, D. Zhan, L. Wang, C. K. Poh, C. H. Tang, H. Gong, Z. X. Shen, L. Y. Jianyi, R. S. Ruoff, Energ. Environ. Sci. 2012, 5, 7936.

[109] X. R. Wang, X. L. Li, L. Zhang, Y. Yoon, P. K. Weber, H. L. Wang, J. Guo, H. J. Dai, Science 2009, 324, 768.

[110] H. Niwa, K. Horiba, Y. Harada, M. Oshima, T. Ikeda, K. Terakura, J. Ozaki, S. Miyata, J. Power Sources 2009, 187, 93.

[111] D. W. Boukhvalov, Y. W. Son, Nanoscale 2012, 4, 417.

[112] U. Bangert, W. Pierce, D. M. Kepaptsoglou, Q. Ramasse, R. Zan, M. H. Gass, J. A. Van den Berg, C. B. Boothroyd, J. Amani, H. Hofsass, Nano Lett. 2013, 13, 4902.

[113] S. Y. Wang, L. P. Zhang, Z. H. Xia, A. Roy, D. W. Chang, J. B. Baek, L. M. Dai, Angew. Chem. Int. Edit. 2012, 51, 4209.

[114] Y. Zheng, Y. Jiao, L. Ge, M. Jaroniec, S. Z. Qiao, Angew. Chem. Int. Edit. 2013, 52, 3110.

[115] Y. Meng, H. K. Mao, P. J. Eng, T. P. Trainor, M. Newville, M. Y. Hu, C. C. Kao, J. F. Shu, D. Hausermann, R. J. Hemley, Nat. Mater. 2004, 3, 111.

[116] L. Vel, G. Demazeau, J. Etourneau, Mater. Sci. Eng.: B 1991, 10, 149.

[117] D. Pacile, J. C. Meyer, C. O. Girit, A. Zettl, Appl. Phys. Lett. 2008, 92, 133107.

[118] J. C. Meyer, A. Chuvilin, G. Algara-Siller, J. Biskupek, U. Kaiser, Nano Lett. 2009, 9, 2683.

[119] N. Alem, R. Erni, C. Kisielowski, M. D. Rossell, W. Gannett, A. Zettl, Phys. Rev. B 2009, 80, 155425.

[120]N. Alem, O. V. Yazyev, C. Kisielowski, P. Denes, U. Dahmen, P. Hartel, M. Haider, M. Bischoff, B. Jiang, S. G. Louie, A. Zettl, Phys. Rev. Lett. 2011, 106, 126102.

[121] K. Suenaga, H. Kobayashi, M. Koshino, Phys. Rev. Lett. 2012, 108, 075501.

[122] B. Huang, H. J. Xiang, J. J. Yu, S. H. Wei, Phys. Rev. Lett. 2012, 108, 206802.

[123] M. Parzefall, P. Bharadwaj, A. Jain, T. Taniguchi, K. Watanabe, L. Novotny, Nat. Nanotechnol. 2015, 10, 1058.

[124] R. Bourrellier, S. Meuret, A. Tararan, O. Stephan, M. Kociak, L. H. G. Tizei, A. Zobelli, Nano Lett. 2016, 16, 4317.

[125] T. T. Tran, K. Bray, M. J. Ford, M. Toth, I. Aharonovich, Nat. Nanotechnol. 2016, 11, 37.

[126] S. Lin, X. X. Ye, R. S. Johnson, H. Guo, J. Phys. Chem. C 2013, 117, 17319.

[127] H. Oka, O. O. Brovko, M. Corbetta, V. S. Stepanyuk, D. Sander, J. Kirschner, Rev. Mod. Phys. 2014, 86, 1127.

[128] S. Baumann, W. Paul, T. Choi, C. P. Lutz, A. Ardavan, A. J. Heinrich, Science 2015, 350, 417.

[129] M. Enayat, Z. X. Sun, U. R. Singh, R. Aluru, S. Schmaus, A. Yaresko, Y. Liu, C. T. Lin, V. Tsurkan, A. Loidl, J. Deisenhofer, P. Wahl, Science 2014, 345, 653.

[130] T. Miyamachi, T. Schuh, T. Markl, C. Bresch, T. Balashov, A. Stohr, C. Karlewski, S. Andre, M. Marthaler, M. Hoffmann, M. Geilhufe, S. Ostanin, W. Hergert, I. Mertig, G. Schon, A. Ernst, W. Wulfhekel, Nature 2013, 503, 242.

[131] S. Loth, S. Baumann, C. P. Lutz, D. M. Eigler, A. J. Heinrich, Science 2012, 335, 196.

[132] Y. Zhang, T.-T. Tang, C. Girit, Z. Hao, M. C. Martin, A. Zettl, M. F. Crommie, Y. R. Shen, F. Wang, Nature 2009, 459, 820.

[133] M. S. C. Mazzoni, R. W. Nunes, S. Azevedo, H. Chacham, Phys. Rev. B 2006, 73, 073108.

[134] A. Y. Liu, R. M. Wentzcovitch, M. L. Cohen, Phys. Rev. B 1989, 39, 1760.

[135] X. L. Wei, M. S. Wang, Y. Bando, D. Golberg, ACS Nano 2011, 5, 2916.

[136] M. O. Watanabe, S. Itoh, K. Mizushima, T. Sasaki, J. Appl. Phys. 1995, 78, 2880.

[137] M. O. Watanabe, S. Itoh, T. Sasaki, K. Mizushima, Phys. Rev. Lett. 1996, 77, 187.

[138] Y. Chen, J. C. Barnard, R. E. Palmer, M. O. Watanabe, T. Sasaki, Phys. Rev. Lett. 1999, 83, 2406.

[139] L. Ci, L. Song, C. H. Jin, D. Jariwala, D. X. Wu, Y. J. Li, A. Srivastava, Z. F. Wang, K. Storr, L. Balicas, F. Liu, P. M. Ajayan, Nat. Mater. 2010, 9, 430.

[140] P. Sutter, R. Cortes, J. Lahiri, E. Sutter, Nano Lett. 2012, 12, 4869.

[141] C. Huang, C. Chen, M. Zhang, L. Lin, X. Ye, S. Lin, M. Antonietti, X. Wang, Nat. Commun. 2015, 6, 7698.

[142] K. Yuge, Phys. Rev. B 2009, 79, 144109.

[143] X. L. Wei, M. S. Wang, Y. Bando, D. Golberg, J. Am. Chem. Soc. 2010, 132, 13592.

[144] R. Arenal, O. Stephan, M. Kociak, D. Taverna, A. Loiseau, C. Colliex, Phys. Rev. Lett. 2005, 95, 127601.

[145] C. T. Pan, R. R. Nair, U. Bangert, Q. Ramasse, R. Jalil, R. Zan, C. R. Seabourne, A. J. Scott, Phys. Rev. B 2012, 85, 045440.

[146] M. Chhowalla, H. S. Shin, G. Eda, L.-J. Li, K. P. Loh, H. Zhang, Nat. Chem. 2013, 5, 263.

[147] Q. H. Wang, K. Kalantar-Zadeh, A. Kis, J. N. Coleman, M. S. Strano, Nat. Nanotechnol. 2012, 7, 699.

[148] Mattheis.Lf, Phys. Rev. B 1973, 8, 3719.

[149] K. F. Mak, K. L. He, J. Shan, T. F. Heinz, Nat. Nanotechnol. 2012, 7, 494.

[150] H. L. Zeng, J. F. Dai, W. Yao, D. Xiao, X. D. Cui, Nat. Nanotechnol. 2012, 7, 490.

[151] T. Cao, G. Wang, W. P. Han, H. Q. Ye, C. R. Zhu, J. R. Shi, Q. Niu, P. H. Tan, E. Wang, B. L. Liu, J. Feng, Nat. Commun. 2012, 3, 887.

[152] S. F. Wu, C. M. Huang, G. Aivazian, J. S. Ross, D. H. Cobden, X. D. Xu, ACS Nano 2013, 7, 2768.

[153] B. Radisavljevic, A. Kis, Nat. Mater. 2013, 12, 815.

[154] S. Helveg, J. V. Lauritsen, E. Laegsgaard, I. Stensgaard, J. K. Norskov, B. S. Clausen, H. Topsoe, F. Besenbacher, Phys. Rev. Lett. 2000, 84, 951.

[155] H. Hwang, H. Kim, J. Cho, Nano Lett. 2011, 11, 4826.

[156] C. Q. Feng, J. Ma, H. Li, R. Zeng, Z. P. Guo, H. K. Liu, Mater. Res. Bull. 2009, 44, 1811.

[157] J. Chen, N. Kuriyama, H. Yuan, H. T. Takeshita, T. Sakai, J. Am. Chem. Soc. 2001, 123, 11813.

[158] K. F. Mak, C. Lee, J. Hone, J. Shan, T. F. Heinz, Phys. Rev. Lett. 2010, 105, 136805.

[159]J. N. Coleman, M. Lotya, A. O'Neill, S. D. Bergin, P. J. King, U. Khan, K. Young, A. Gaucher, S. De, R. J. Smith, I. V. Shvets, S. K. Arora, G. Stanton, H. Y. Kim, K. Lee, G. T. Kim, G. S. Duesberg, T. Hallam, J. J. Boland, J. J. Wang, J. F. Donegan, J. C. Grunlan, G. Moriarty, A. Shmeliov, R. J. Nicholls, J. M. Perkins, E. M. Grieveson, K. Theuwissen, D. W. McComb, P. D. Nellist, V. Nicolosi, Science 2011, 331, 568.

[160] A. Castellanos-Gomez, M. Barkelid, A. M. Goossens, V. E. Calado, H. S. J. van der Zant, G. A. Steele, Nano Lett. 2012, 12, 3187.

[161] Y. L. Liu, H. Y. Nan, X. Wu, W. Pan, W. H. Wang, J. Bai, W. W. Zhao, L. T. Sun, X. R. Wang, Z. H. Ni, ACS Nano 2013, 7, 4202.

[162] K. K. Liu, W. J. Zhang, Y. H. Lee, Y. C. Lin, M. T. Chang, C. Su, C. S. Chang, H. Li, Y. M. Shi, H. Zhang, C. S. Lai, L. J. Li, Nano Lett. 2012, 12, 1538.

[163] Y. M. Shi, W. Zhou, A. Y. Lu, W. J. Fang, Y. H. Lee, A. L. Hsu, S. M. Kim, K. K. Kim, H. Y. Yang, L. J. Li, J. C. Idrobo, J. Kong, Nano Lett. 2012, 12, 2784.

[164] S. Najmaei, Z. Liu, W. Zhou, X. L. Zou, G. Shi, S. D. Lei, B. I. Yakobson, J. C. Idrobo, P. M. Ajayan, J. Lou, Nat. Mater. 2013, 12, 754.

[165] A. M. van der Zande, P. Y. Huang, D. A. Chenet, T. C. Berkelbach, Y. M. You, G. H. Lee, T. F. Heinz, D. R. Reichman, D. A. Muller, J. C. Hone, Nat. Mater. 2013, 12, 554.

[166] X. S. Wang, H. B. Feng, Y. M. Wu, L. Y. Jiao, J. Am. Chem. Soc. 2013, 135, 5304.

[167] W. Jin, P.-C. Yeh, N. Zaki, D. Zhang, J. T. Sadowski, A. Al-Mahboob, A. M. van der Zande, D. A. Chenet, J. I. Dadap, I. P. Herman, P. Sutter, J. Hone, R. M. Osgood, Jr., Phys. Rev. Lett. 2013, 111, 106801.

[168] H. S. Lee, S.-W. Min, Y.-G. Chang, M. K. Park, T. Nam, H. Kim, J. H. Kim, S. Ryu, S. Im, Nano Lett. 2012, 12, 3695.

[169] Z. Yin, H. Li, H. Li, L. Jiang, Y. Shi, Y. Sun, G. Lu, Q. Zhang, X. Chen, H. Zhang, ACS Nano 2012, 6, 74.

[170] K. Behnia, Nat. Nanotechnol. 2012, 7, 488.

[171] Y. J. Zhang, T. Oka, R. Suzuki, J. T. Ye, Y. Iwasa, Science 2014, 344, 725.

[172] H. Li, Z. Yin, Q. He, H. Li, X. Huang, G. Lu, D. W. H. Fam, A. I. Y. Tok, Q. Zhang, H. Zhang, Small 2012, 8, 63.

[173] H. P. Komsa, A. V. Krasheninnikov, Phys. Rev. B 2015, 91, 125304.

[174] W. Zhou, X. L. Zou, S. Najmaei, Z. Liu, Y. M. Shi, J. Kong, J. Lou, P. M. Ajayan, B. I. Yakobson, J. C. Idrobo, Nano Lett. 2013, 13, 2615.

[175] Z. Y. Wang, H. Li, Z. Liu, Z. J. Shi, J. Lu, K. Suenaga, S. K. Joung, T. Okazaki, Z. N. Gu, J. Zhou, Z. X. Gao, G. P. Li, S. Sanvito, E. G. Wang, S. Iijima, J. Am. Chem. Soc. 2010, 132, 13840.

[176] Y. F. Li, Z. Zhou, S. B. Zhang, Z. F. Chen, J. Am. Chem. Soc. 2008, 130, 16739.

[177] C. Zhang, A. Johnson, C.-L. Hsu, L.-J. Li, C.-K. Shih, Nano Lett. 2014, 14, 2443.

[178] Y. H. Lee, X. Q. Zhang, W. J. Zhang, M. T. Chang, C. T. Lin, K. D. Chang, Y. C. Yu, J. T. W. Wang, C. S. Chang, L. J. Li, T. W. Lin, Adv. Mater. 2012, 24, 2320.

[179] H. Liu, M. W. Si, S. Najmaei, A. T. Neal, Y. C. Du, P. M. Ajayan, J. Lou, P. D. D. Ye, Nano Lett. 2013, 13, 2640.

[180] Z. H. Yu, Y. M. Pan, Y. T. Shen, Z. L. Wang, Z. Y. Ong, T. Xu, R. Xin, L. J. Pan, B. G. Wang, L. T. Sun, J. L. Wang, G. Zhang, Y. W. Zhang, Y. Shi, X. R. Wang, Nat. Commun. 2014, 5, 5290.

[181] K. Kaasbjerg, K. S. Thygesen, K. W. Jacobsen, Phys. Rev. B 2012, 85, 115317.

[182] Y. C. Lin, D. O. Dumcenco, H. P. Komsa, Y. Niimi, A. V. Krasheninnikov, Y. S. Huang, K. Suenaga, Adv. Mater. 2014, 26, 2857.

[183] K. Dolui, I. Rungger, C. Das Pemmaraju, S. Sanvito, Phys. Rev. B 2013, 88, 075420.

[184] H. P. Komsa, J. Kotakoski, S. Kurasch, O. Lehtinen, U. Kaiser, A. V. Krasheninnikov, Phys. Rev. Lett. 2012, 109, 035503.

[185] J. C. Meyer, F. Eder, S. Kurasch, V. Skakalova, J. Kotakoski, H. J. Park, S. Roth, A. Chuvilin, S. Eyhusen, G. Benner, A. V. Krasheninnikov, U. Kaiser, Phys. Rev. Lett. 2012, 108, 196102.

[186] J. Suh, T. E. Park, D. Y. Lin, D. Y. Fu, J. Park, H. J. Jung, Y. B. Chen, C. Ko, C. Jang, Y. H. Sun, R. Sinclair, J. Chang, S. Tongay, J. Q. Wu, Nano Lett. 2014, 14, 6976.

[187] H. Fang, M. Tosun, G. Seol, T. C. Chang, K. Takei, J. Guo, A. Javey, Nano Lett. 2013, 13, 1991.

[188] Y. C. Cheng, Z. Y. Zhu, W. B. Mi, Z. B. Guo, U. Schwingenschlogl, Phys. Rev. B 2013, 87, 100401.

[189] R. Mishra, W. Zhou, S. J. Pennycook, S. T. Pantelides, J. C. Idrobo, Phys. Rev. B 2013, 88, 144409.

[190] J. H. Hong, Z. X. Hu, M. Probert, K. Li, D. H. Lv, X. N. Yang, L. Gu, N. N. Mao, Q. L. Feng, L. M. Xie, J. Zhang, D. Z. Wu, Z. Y. Zhang, C. H. Jin, W. Ji, X. X. Zhang, J. Yuan, Z. Zhang, Nat. Commun. 2015, 6, 6293.

[191] Q. Feng, Y. Zhu, J. Hong, M. Zhang, W. Duan, N. Mao, J. Wu, H. Xu, F. Dong, F. Lin, Adv. Mater. 2014, 26, 2648.

[192] Q. L. Feng, N. N. Mao, J. X. Wu, H. Xu, C. M. Wang, J. Zhang, L. M. Xie, ACS Nano 2015, 9, 7450.

[193] C. Gong, C. M. Huang, J. Miller, L. X. Cheng, Y. F. Hao, D. Cobden, J. Kim, R. S. Ruoff, R. M. Wallace, K. Cho, X. D. Xu, Y. J. Chabal, ACS Nano 2013, 7, 11350.

[194] H. Qiu, T. Xu, Z. L. Wang, W. Ren, H. Y. Nan, Z. H. Ni, Q. Chen, S. J. Yuan, F. Miao, F. Q. Song, G. Long, Y. Shi, L. T. Sun, J. L. Wang, X. R. Wang, Nat. Commun. 2013, 4, 2642.

[195] A. Ferrari, J. Meyer, V. Scardaci, C. Casiraghi, M. Lazzeri, F. Mauri, S. Piscanec, D. Jiang, K. Novoselov, S. Roth, Phys. Rev. Lett. 2006, 97, 187401.

[196] W. M. Parkin, A. Balan, L. Liang, P. M. Das, M. Lamparski, C. H. Naylor, J. A. Rodríguez-Manzo, A. C. Johnson, V. Meunier, M. Drndic, ACS Nano 2016, 10, 4134.

[197] P. K. Chow, R. B. Jacobs-Gedrim, J. Gao, T. M. Lu, B. Yu, H. Terrones, N. Koratkar, ACS Nano 2015, 9, 1520.

[198] K. F. Mak, K. L. He, C. Lee, G. H. Lee, J. Hone, T. F. Heinz, J. Shan, Nat. Mater. 2013, 12, 207.

[199] S. Tongay, J. Suh, C. Ataca, W. Fan, A. Luce, J. S. Kang, J. Liu, C. Ko, R. Raghunathanan, J. Zhou, F. Ogletree, J. B. Li, J. C. Grossman, J. Q. Wu, Sci. Rep. 2013, 3, 2657.

[200] H. Y. Nan, Z. L. Wang, W. H. Wang, Z. Liang, Y. Lu, Q. Chen, D. W. He, P. H. Tan, F. Miao, X. R. Wang, J. L. Wang, Z. H. Ni, ACS Nano 2014, 8, 5738.

[201] F. Fabbri, E. Rotunno, E. Cinquanta, D. Campi, E. Bonnini, D. Kaplan, L. Lazzarini, M. Bernasconi, C. Ferrari, M. Longo, G. Nicotra, A. Molle, V. Swaminathan, G. Salviati, Nat. Commun. 2016, 7, 13044.

[202] A. Srivastava, M. Sidler, A. V. Allain, D. S. Lembke, A. Kis, A. Imamoglu, Nat. Nanotechnol. 2015, 10, 491.

[203] M. Koperski, K. Nogajewski, A. Arora, V. Cherkez, P. Mallet, J. Y. Veuillen, J. Marcus, P. Kossacki, M. Potemski, Nat. Nanotechnol. 2015, 10, 503.

[204] Y. M. He, G. Clark, J. R. Schaibley, Y. He, M. C. Chen, Y. J. Wei, X. Ding, Q. Zhang, W. Yao, X. D. Xu, C. Y. Lu, J. W. Pan, Nat. Nanotechnol. 2015, 10, 497.

[205]C. Chakraborty, L. Kinnischtzke, K. M. Goodfellow, R. Beams, A. N. Vamivakas, Nat. Nanotechnol. 2015, 10, 507.

[206] W. J. Zhu, T. Low, Y. H. Lee, H. Wang, D. B. Farmer, J. Kong, F. N. Xia, P. Avouris, Nat. Commun. 2014, 5, 3087.

[207] S. Takagi, A. Toriumi, M. Iwase, H. Tango, IEEE T. Electron Dev. 1994, 41, 2357.

[208] J. S. Qiao, X. H. Kong, Z. X. Hu, F. Yang, W. Ji, Nat. Commun. 2014, 5, 4475.

[209] Y. Gong, Z. Liu, A. R. Lupini, G. Shi, J. Lin, S. Najmaei, Z. Lin, A. L. Elías, A. Berkdemir, G. You, Nano Lett. 2013, 14, 442.

[210]H. Li, X. Duan, X. Wu, X. Zhuang, H. Zhou, Q. Zhang, X. Zhu, W. Hu, P. Ren, P. Guo, J. Am. Chem. Soc. 2014, 136, 3756.

[211] J. Mann, Q. Ma, P. M. Odenthal, M. Isarraraz, D. Le, E. Preciado, D. Barroso, K. Yamaguchi, G. V. Palacio, A. Nguyen, T. Tran, M. Wurch, A. Nguyen, V. Klee, S. Bobek, D. Z. Sun, T. F. Heinz, T. S. Rahman, R. Kawakami, L. Bartels, Adv. Mater. 2014, 26, 1399.

[212] Y. F. Chen, J. Y. Xi, D. O. Dumcenco, Z. Liu, K. Suenaga, D. Wang, Z. G. Shuai, Y. S. Huang, L. M. Xie, ACS Nano 2013, 7, 4610.

[213] D. O. Dumcenco, H. Kobayashi, Z. Liu, Y.-S. Huang, K. Suenaga, Nat. Commun. 2013, 4, 1351.

[214] M. Zhang, J. X. Wu, Y. M. Zhu, D. O. Dumcenco, J. H. Hong, N. N. Mao, S. B. Deng, Y. F. Chen, Y. L. Yang, C. H. Jin, S. H. Chaki, Y. S. Huang, J. Zhang, L. M. Xie, ACS Nano 2014, 8, 7130.

[215] S. Tongay, D. S. Narang, J. Kang, W. Fan, C. H. Ko, A. V. Luce, K. X. Wang, J. Suh, K. D. Patel, V. M. Pathak, J. B. Li, J. Q. Wu, Appl. Phys. Lett. 2014, 104, 012101.

[216] B. Huang, M. Yoon, B. G. Sumpter, S. H. Wei, F. Liu, Phys. Rev. Lett. 2015, 115, 126806.

[217] Xufan Li, Ming-Wei Lin, Leonardo Basile, Saban M. Hus, Alexander A. Puretzky, Jaekwang Lee , Yen-Chien Kuo , Lo-Yueh Chang , Kai Wang , Juan C. Idrobo , An-Ping Li , Chia-Hao Chen , Christopher M. Rouleau , David B. Geohegan , K. Xiao, Adv. Mater. 2016, 28, 8240.

[218] D. Kiriya, M. Tosun, P. D. Zhao, J. S. Kang, A. Javey, J. Am. Chem. Soc. 2014, 136, 7853.

[219] K. H. Zhang, S. M. Feng, J. J. Wang, A. Azcatl, N. Lu, R. Addou, N. Wang, C. J. Zhou, J. Lerach, V. Bojan, M. J. Kim, L. Q. Chen, R. M. Wallace, M. Terrones, J. Zhu, J. A. Robinson, Nano Lett. 2015, 15, 6586.

[220] J. Gao, Y. D. Kim, L. Liang, J. C. Idrobo, P. Chow, J. Tan, B. Li, L. Li, B. G. Sumpter, T.-M. Lu, V. Meunier, J. Hone, N. Koratkar, Adv. Mater. 2016, 28, 9735.

[221] J. K. Norskov, T. Bligaard, J. Rossmeisl, C. H. Christensen, Nat. Chem. 2009, 1, 37.

[222] B. Hinnemann, P. G. Moses, J. Bonde, K. P. Jorgensen, J. H. Nielsen, S. Horch, I. Chorkendorff, J. K. Norskov, J. Am. Chem. Soc. 2005, 127, 5308.

[223] J. Kibsgaard, Z. B. Chen, B. N. Reinecke, T. F. Jaramillo, Nat. Mater. 2012, 11, 963.

[224] A. B. Laursen, S. Kegnaes, S. Dahl, I. Chorkendorff, Energ. Environ. Sci. 2012, 5, 5577.

[225] T. F. Jaramillo, K. P. Jorgensen, J. Bonde, J. H. Nielsen, S. Horch, I. Chorkendorff, Science 2007, 317, 100.

[226]J. F. Xie, H. Zhang, S. Li, R. X. Wang, X. Sun, M. Zhou, J. F. Zhou, X. W. Lou, Y. Xie, Adv. Mater. 2013, 25, 5807.

[227] A. B. Laursen, P. C. K. Vesborg, I. Chorkendorff, Chem. Commun. 2013, 49, 4965.

[228] Y. H. Chang, C. T. Lin, T. Y. Chen, C. L. Hsu, Y. H. Lee, W. J. Zhang, K. H. Wei, L. J. Li, Adv. Mater. 2013, 25, 756.

[229] D. Merki, X. L. Hu, Energ. Environ. Sci. 2011, 4, 3878.

[230] G. L. Ye, Y. J. Gong, J. H. Lin, B. Li, Y. M. He, S. T. Pantelides, W. Zhou, R. Vajtai, P. M. Ajayan, Nano Lett. 2016, 16, 1097.

[231] J. F. Xie, J. J. Zhang, S. Li, F. Grote, X. D. Zhang, H. Zhang, R. X. Wang, Y. Lei, B. C. Pan, Y. Xie, J. Am. Chem. Soc. 2013, 135, 17881.

[232] D. Voiry, H. Yamaguchi, J. W. Li, R. Silva, D. C. B. Alves, T. Fujita, M. W. Chen, T. Asefa, V. B. Shenoy, G. Eda, M. Chhowalla, Nat. Mater. 2013, 12, 850.

[233] Y. Yin, J. C. Han, Y. M. Zhang, X. H. Zhang, P. Xu, Q. Yuan, L. Samad, X. J. Wang, Y. Wang, Z. H. Zhang, P. Zhang, X. Z. Cao, B. Song, S. Jin, J. Am. Chem. Soc. 2016, 138, 7965.

[234] M. A. Lukowski, A. S. Daniel, F. Meng, A. Forticaux, L. S. Li, S. Jin, J. Am. Chem. Soc. 2013, 135, 10274.

[235] D. Voiry, M. Salehi, R. Silva, T. Fujita, M. W. Chen, T. Asefa, V. B. Shenoy, G. Eda, M. Chhowalla, Nano Lett. 2013, 13, 6222.

[236] D. Voiry, R. Fullon, J. E. Yang, C. D. C. E. Silva, R. Kappera, I. Bozkurt, D. Kaplan, M. J. Lagos, P. E. Batson, G. Gupta, A. D. Mohite, L. Dong, D. Q. Er, V. B. Shenoy, T. Asefa, M. Chhowalla, Nat. Mater. 2016, 15, 1003.

[237] H. Li, C. Tsai, A. L. Koh, L. L. Cai, A. W. Contryman, A. H. Fragapane, J. H. Zhao, H. S. Han, H. C. Manoharan, F. Abild-Pedersen, J. K. Norskov, X. L. Zheng, Nat. Mater. 2016, 15, 48.

[238] G. Rothenberg, *Catalysis: concepts and green applications*, Wiley-VCH, 2008.

[239] J. D. Benck, T. R. Hellstern, J. Kibsgaard, P. Chakthranont, T. F. Jaramillo, ACS Catal. 2014, 4, 3957.

[240] H. Li, M. Du, M. J. Mleczko, A. L. Koh, Y. Nishi, E. Pop, A. J. Bard, X. L. Zheng, J. Am. Chem. Soc. 2016, 138, 5123.

[241] Y. X. Ouyang, C. Y. Ling, Q. Chen, Z. L. Wang, L. Shi, J. L. Wang, Chem. Mater. 2016, 28, 4390.

[242] J. K. Norskov, T. Bligaard, A. Logadottir, J. R. Kitchin, J. G. Chen, S. Pandelov, J. K. Norskov, J. Electrochem. Soc. 2005, 152, J23.

[243] L. Fei, S. Lei, W.-B. Zhang, W. Lu, Z. Lin, C. H. Lam, Y. Chai, Y. Wang, Nat. Commun. 2016, 7, 12206.

[244] Z.-J. Wang, J. Dong, Y. Cui, G. Eres, O. Timpe, Q. Fu, F. Ding, R. Schlögl, M.-G. Willinger, Nat. Commun. 2016, 7, 13256.

[245] Z. Liu, L. H. Tizei, Y. Sato, Y. C. Lin, C. H. Yeh, P. W. Chiu, M. Terauchi, S. Iijima, K. Suenaga, Small 2016, 12, 252.

[246]X. Xu, Z. Zhang, L. Qiu, J. Zhuang, L. Zhang, H. Wang, C. Liao, H. Song, R. Qiao, P. Gao, Z. Hu, L. Liao, Z. Liao, D. Yu, E. Wang, F. Ding, H. Peng, K. Liu, Nat. Nanotechnol. 2016, 11, 930.

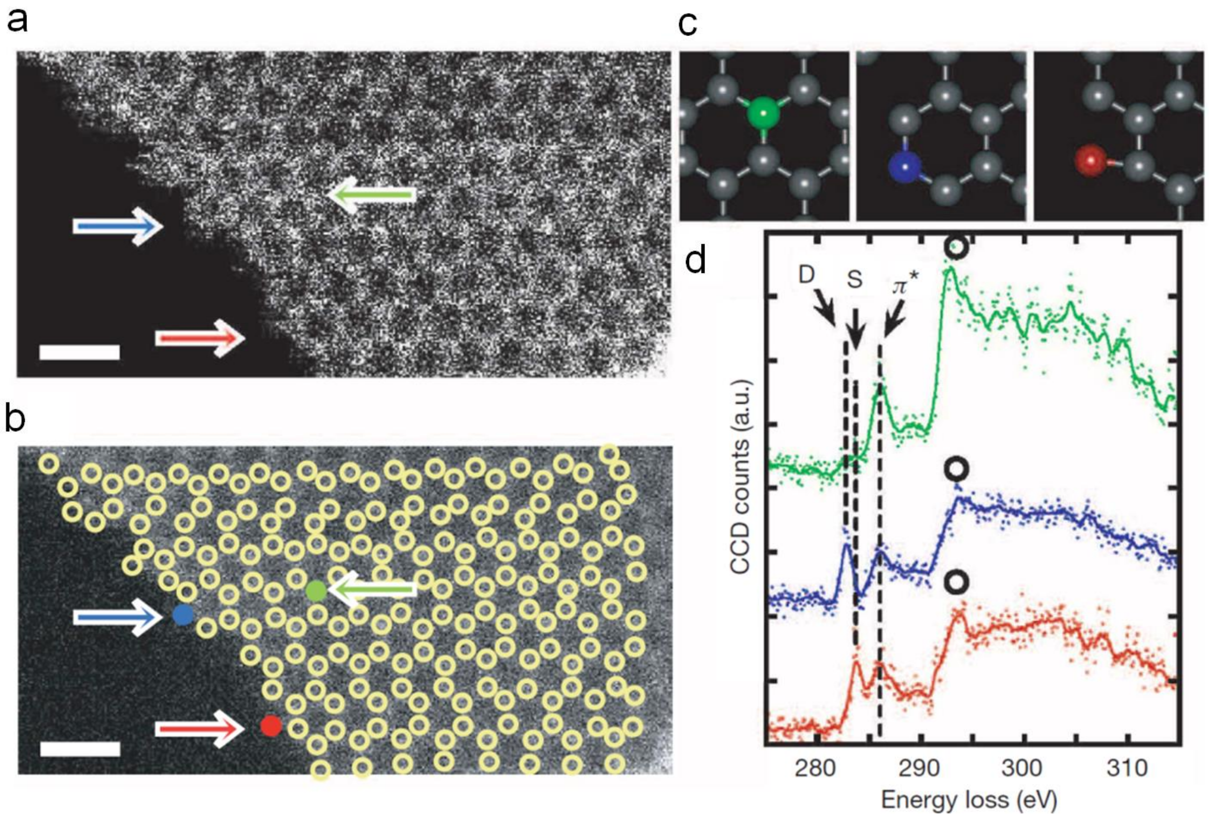

Figure.1 Electronic properties of edge atoms in graphene. (a, b) Atomically resolved ADF image of a graphene edge. Scale bar: 0.5nm. (c) Structure model of the triple- (green), double- (blue) and single-coordinated (red) C atoms. (d) Corresponding experimental EELS-ELNES spectra of the K-edges of different C atoms. Reproduced with permission.[64] Copyright 2010, Nature Publishing Group.

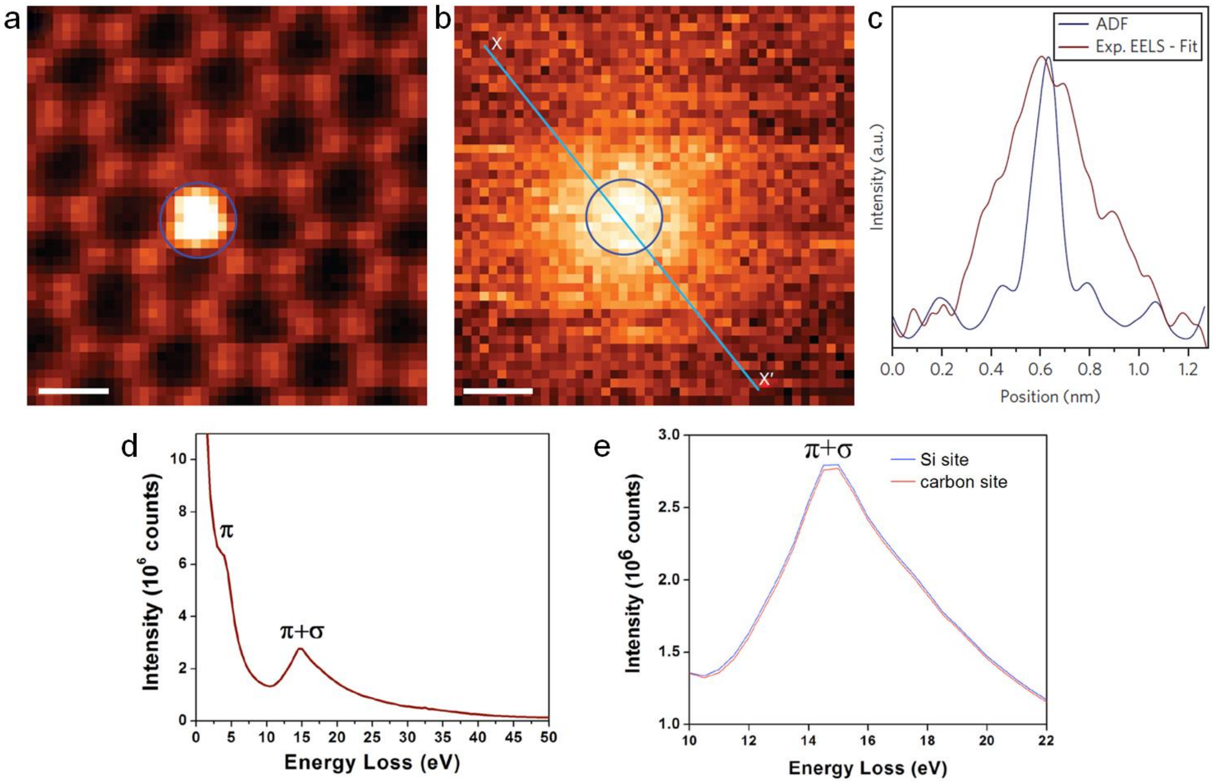

Figure.2 Atomically localized plasmon enhancement by dopant Si in graphene. (a) Atomic resolved ADF image of a four-coordinated Si dopant (Si-C4). Scale bar: 0.2 nm. (b) The mapping of π+σ plasmon excitation around Si dopant. (c) The intensity line profile of ADF image in a and π+σ plasmon mapping in b. (d) Experimental low loss spectra of graphene. (e) The π+σ plasmon peak of graphene enhanced at the Si site. Reproduced with permission.[74] Copyright 2012, Nature Publishing Group.

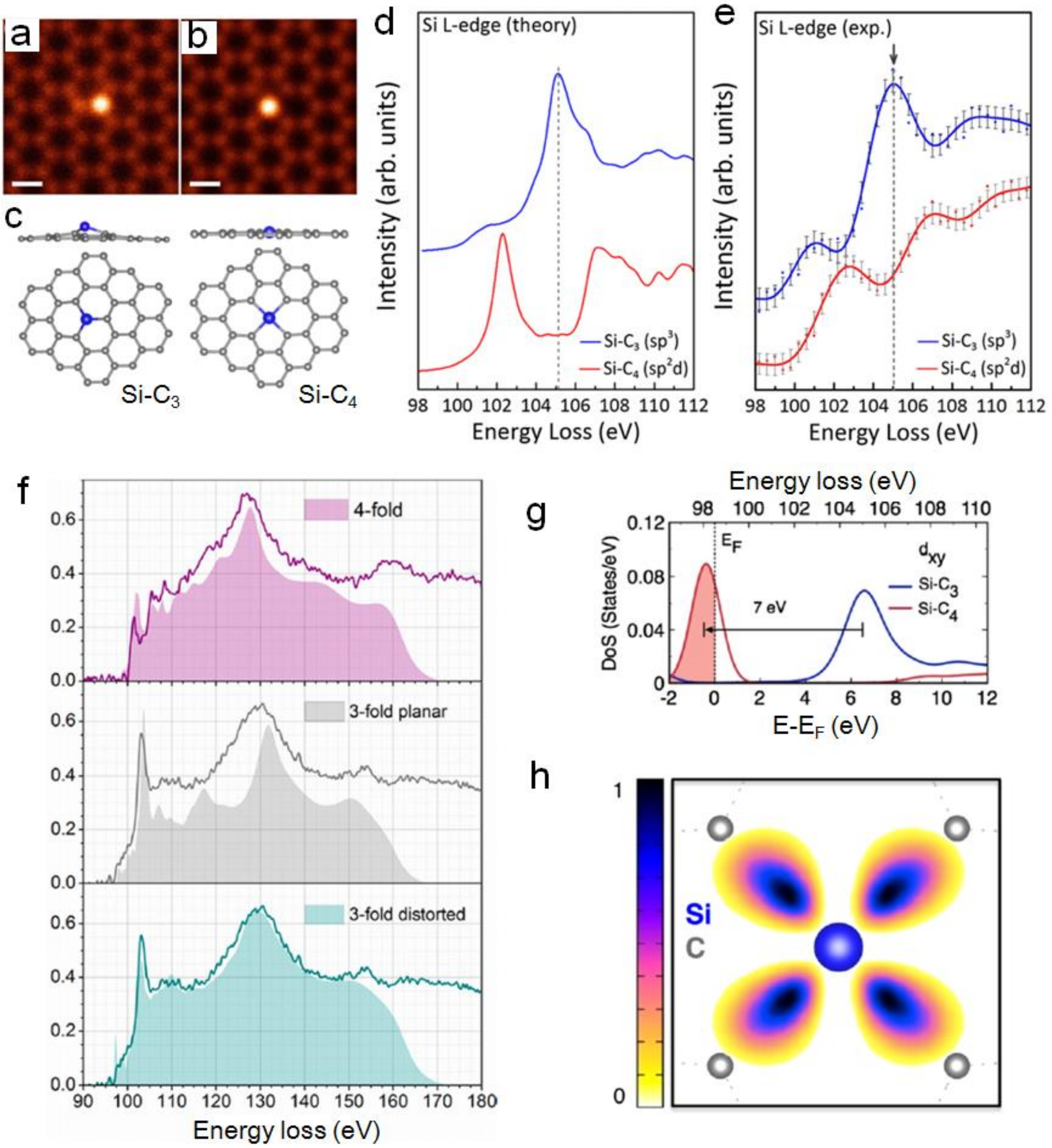

Figure.3 Electronic properties of dopant Si in graphene. (a, b) Experimental ADF image of three- and four-coordinated dopants Si-C$_3$ and Si-C$_4$. (c) DFT calculated structure of Si-C$_3$ and Si-C$_4$. (d) The calculated ELNES based on the relaxed structure in c. (e) The experimental ELNES of Si-C$_3$ and Si-C$_4$. (f) Experimental (curves) and simulated (shaded) EXELFS of 3-fold Si-C$_3$ and 4-fold Si-C$_4$ dopants. Reproduced with permission.[79] Copyright 2012, American Chemical Society. (g) Calculated density of states (DOS) of 3d_{xy} states of the Si-C$_3$ and Si-C$_4$, where Si-C$_4$ has an obvious 7-eV redshift. (h) The charge density distribution of 3d_{xy} state of the Si-C$_4$. Reproduced with permission.[77] Copyright 2012, American Physical Society.

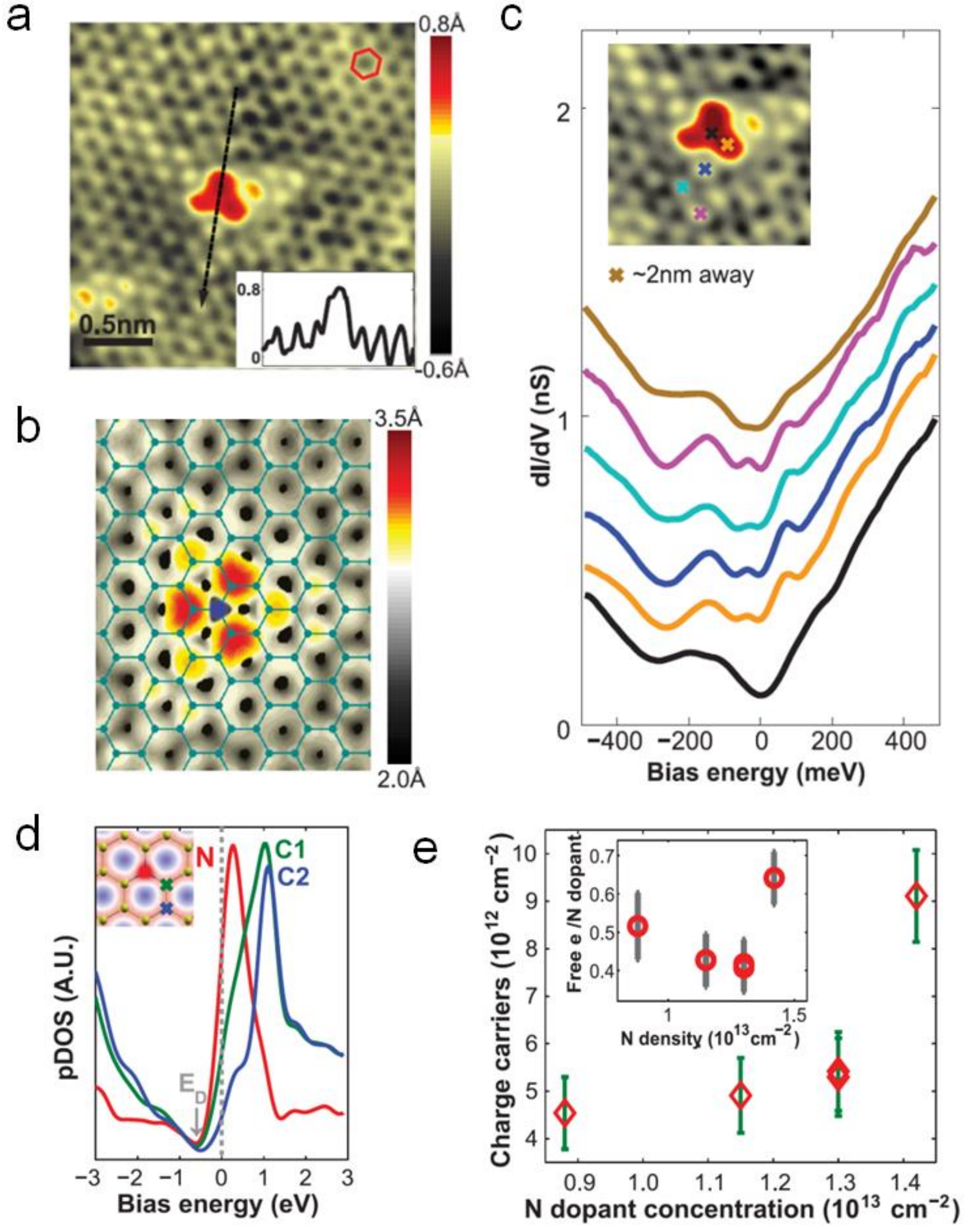

Figure.4 Electronic properties of dopant N in graphene. (a, b) Experimental and simulated STM images of dopant N atom, respectively. (c) The experimental STS of different sites around N dopant. (d) Calculated projected DOS of N atom and neighboring sites. (e) The dependence of charge carrier density on the N dopant concentration. Reproduced with permission.[80] Copyright 2011, Science.

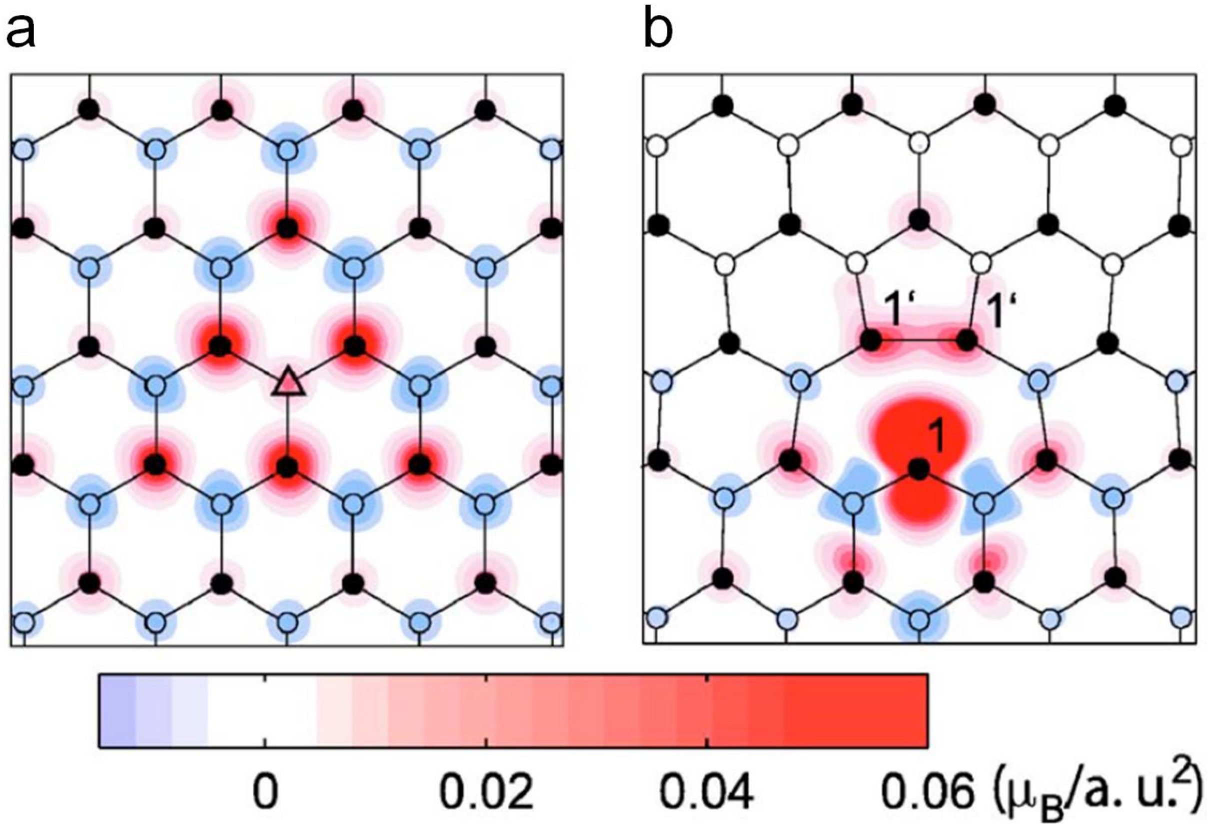

Figure.5 Magnetic properties of H adatom and vacancy in graphene. (a) The magnetic structure of a H adatom (triangle) on top of C lattice. (b) The magnetic structure of a single vacancy. In both cases, the magnetic moments are mostly concentrated within the neighbors of the defects. Reproduced with permission.[86] Copyright 2007, American Physical Society.

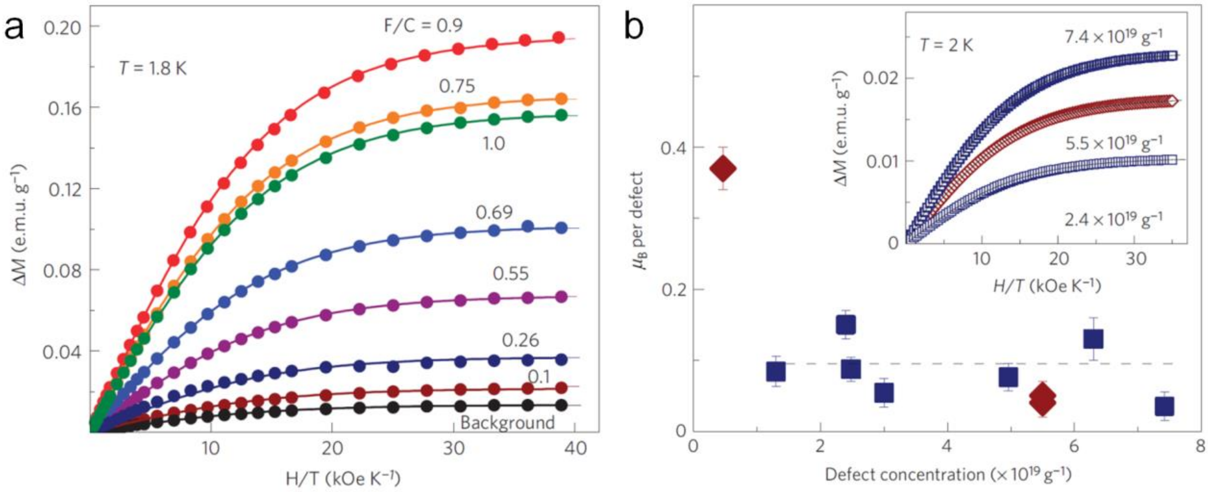

Figure.6 Magnetic properties induced by dopants and vacancies in graphene. (a) Experimental magnetization curve of F-doped graphene at low temperature. (b) The contribution of magnetic moment from vacancy defects. The inset is the magnetization curve. Reproduced with permission.[93] Copyright 2012, Nature Publishing Group.

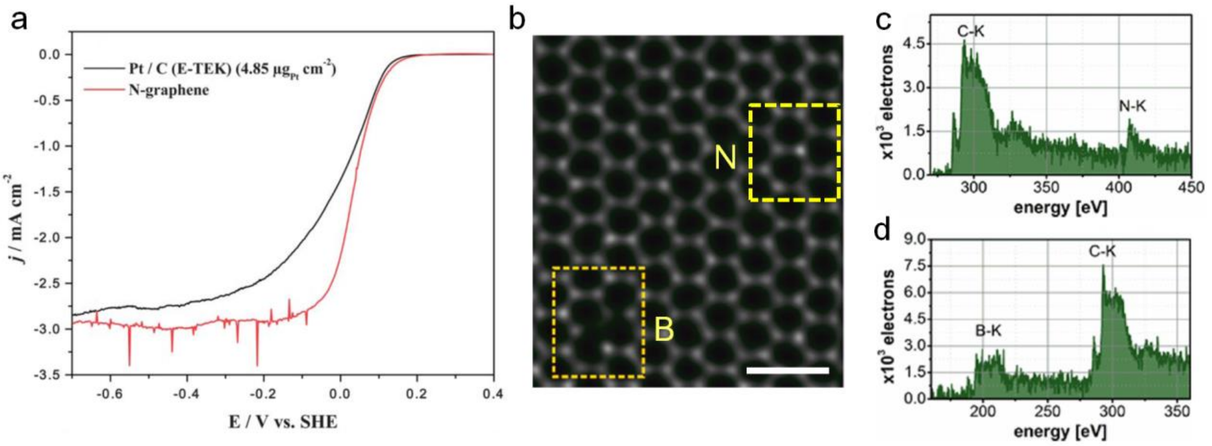

Figure 7. Catalysis performance of doped graphene. (a) The polarization curves in oxygen reduction reaction (ORR) for N-doped graphene and Pt/C. Reproduced with permission.[95] Copyright 2011, The Royal Society of Chemistry. (b) ADF-STEM image of B, N co-doped graphene, where B and N dopants are highlighted. (c, d) Core loss K edges of B and N dopants, respectively. Reproduced with permission.[112] Copyright 2013, American Chemical Society.

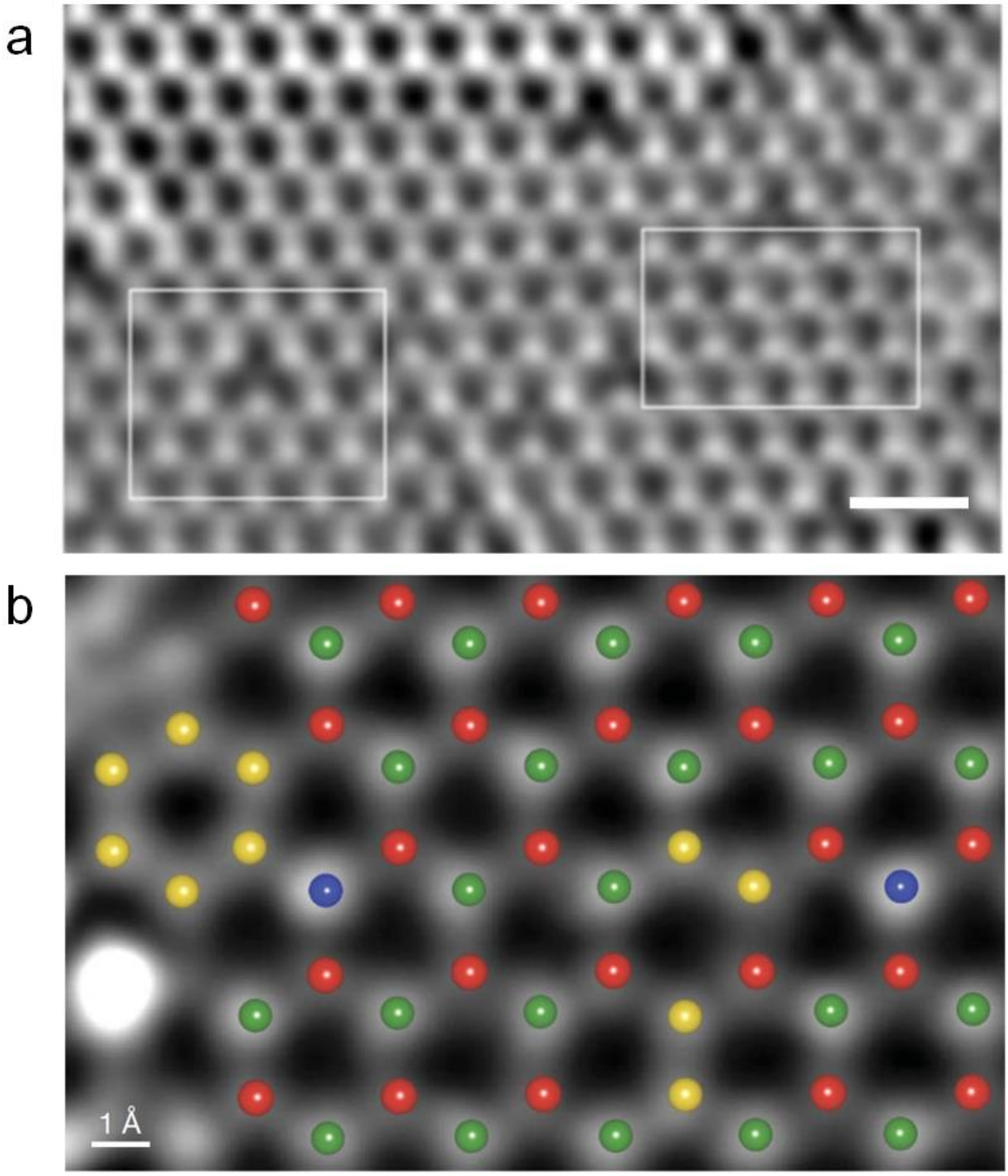

Figure.8 Point defects in monolayer h-BN. (a) Atomically resolved HRTEM image of monolayer BN containing boron vacancies (V_B). Scale bars: 0.5nm. Reproduced with permission.[12] Copyright 2009, American Physical Society. (b) ADF imaging of BN with chemical assignment of C and O impurity dopant atoms. Red: B; green: N; yellow: C; blue: O. Scale bar: 1A. Reproduced with permission.[39] Copyright 2010, Nature Publishing Group.

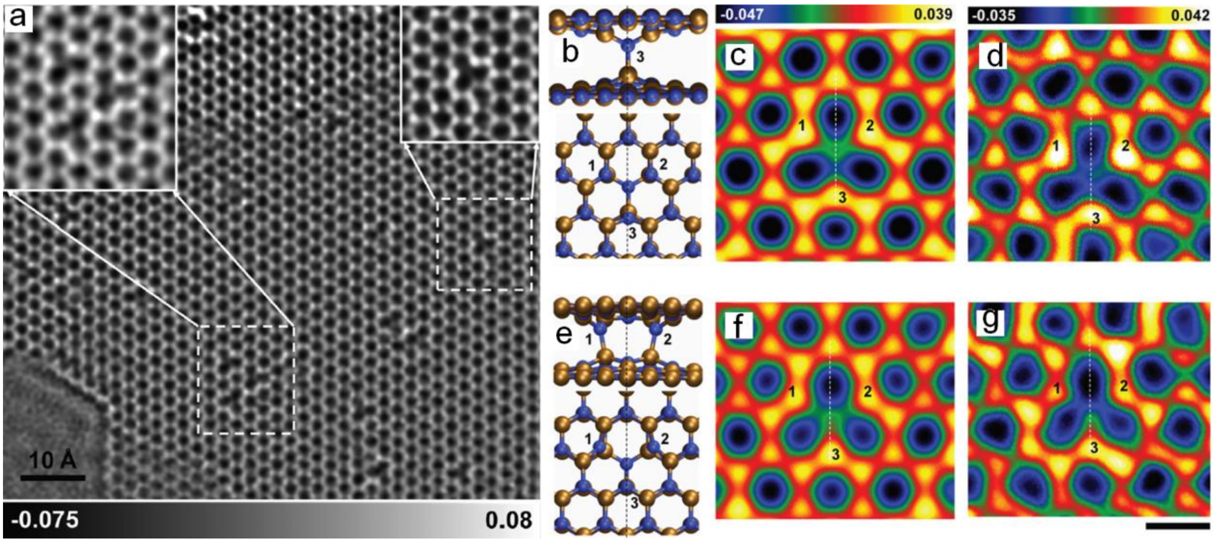

Figure.9 Three-dimensional structure of V_B in bilayer BN. (a) Atomically resolved HRTEM image of bilayer BN where single V_B is highlighted in the squares. (b) Side view and top view of DFT-relaxed structure of single V_B in bilayer BN. Note that among the neighboring atoms, B-N pair in column 3 are bonded with obvious out-of-plane distortion. (c, d) Simulated and experimental HRTEM image of the vacancy structure in b. (e) Side view and top view of another DFT-relaxed structure of single V_B in bilayer BN. Among the neighboring atoms, B-N pair in column 1 and 2 are both bonded within each atom column with out-of-plane displacement. (f, g) Simulated and experimental HRTEM image of the vacancy structure in e. Reproduced with permission.[120] Copyright 2011, American Physical Society.

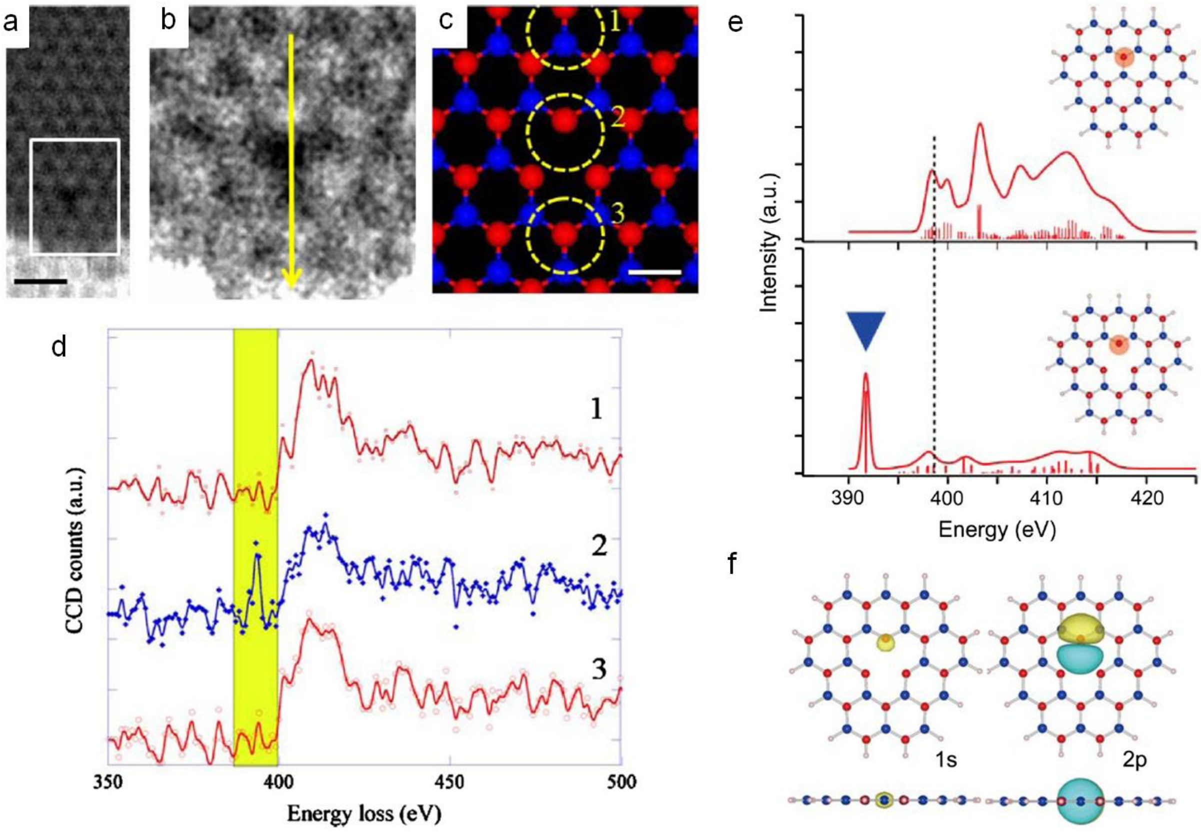

Figure.10 Electronic states of V_B in monolayer BN. (a, b) Atomically resolved ADF image of V_B in monolayer BN. Fig. b is an enlargement of the defect region. Scale bar: 0.5nm. (c) DFT relaxed structure of V_B. (d) Experimental K-edge EELS-ELNES of N atoms 1, 2, 3 collected along the yellow line. The double coordinated N atom (No.2) has an obvious pre-peak. (e) DFT calculated ELNES of the triple-coordinated and double-coordinated N atoms. (f) DFT calculated electronic states distribution involved in the K-edge 1s→2p transition. Reproduced with permission.[121] Copyright 2012, American Physical Society.

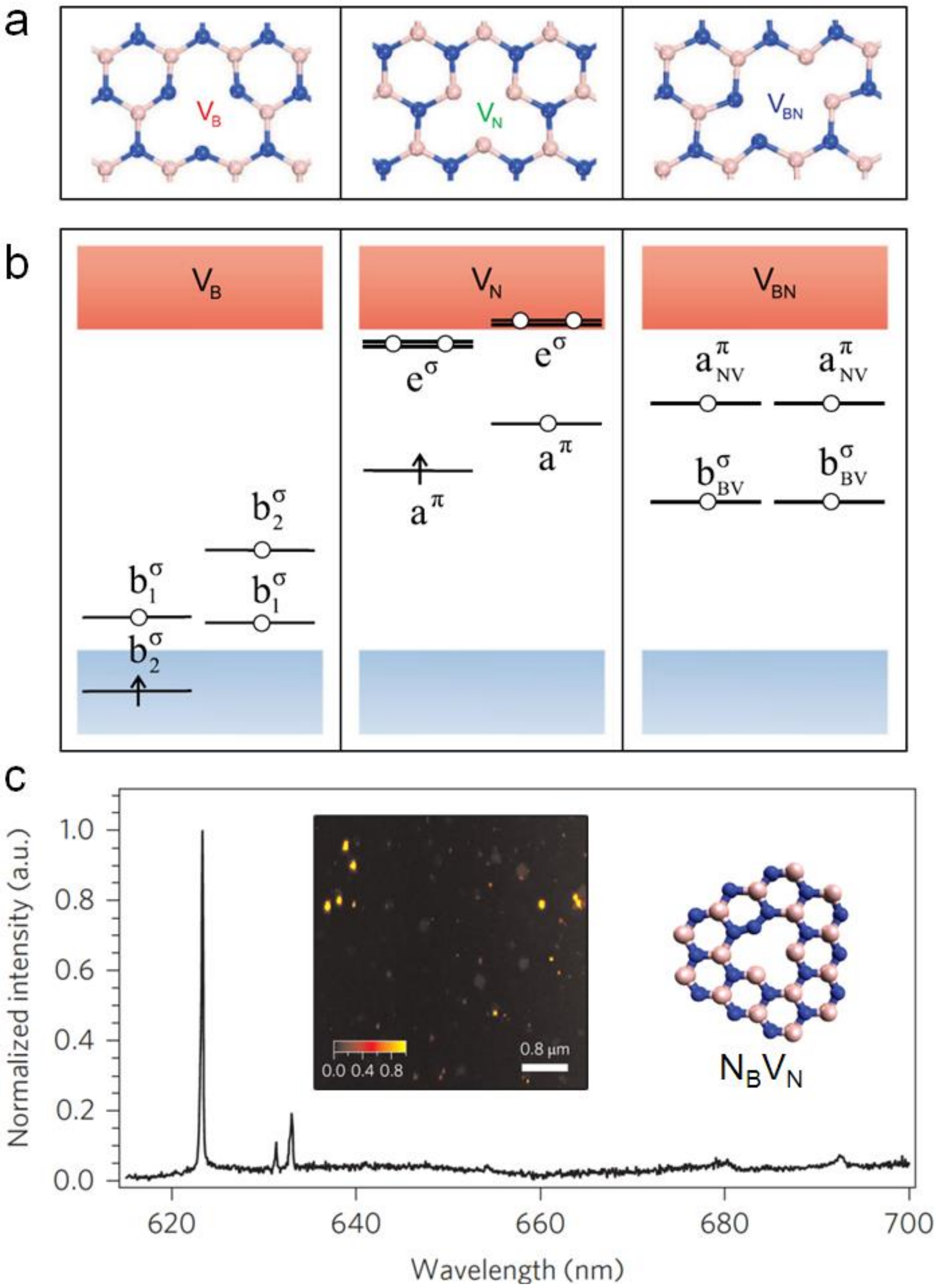

Figure.11 Electronic and photonic properties of vacancies in BN. (a, b) Atomic and electronic structures of vacancies V_B, V_N, V_{BN}, respectively. Reproduced with permission.[122] Copyright 2012, American Physical Society. (c) Single photon emitter resulting from vacancies in BN. Inset shows the ultrabright quantum emission within a BN multilayer and the suggested defect structure responsible for the brightest emission at 623 nm. Reproduced with permission.[125] Copyright 2016, Nature Publishing Group.

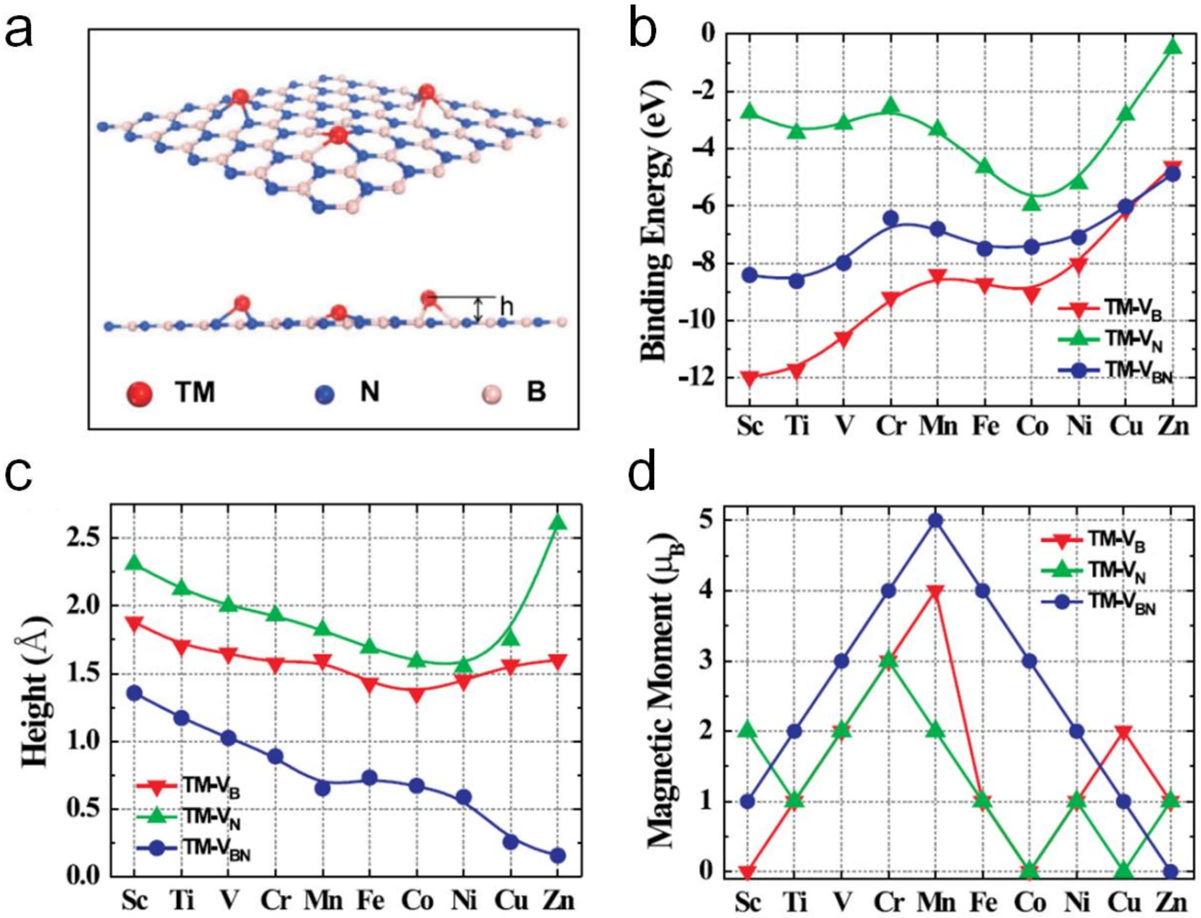

Figure.12 Electronic properties of dopants in monolayer BN. (a) Transition metal (TM) atom dopants occupying the vacancies V_B, V_N, V_{BN}. (b) Binding energies of dopants at different sites. (c) Calculated heights of different dopants. (d) Magnetic properties induced by dopants. Reproduced with permission.[122] Copyright 2012, American Physical Society.

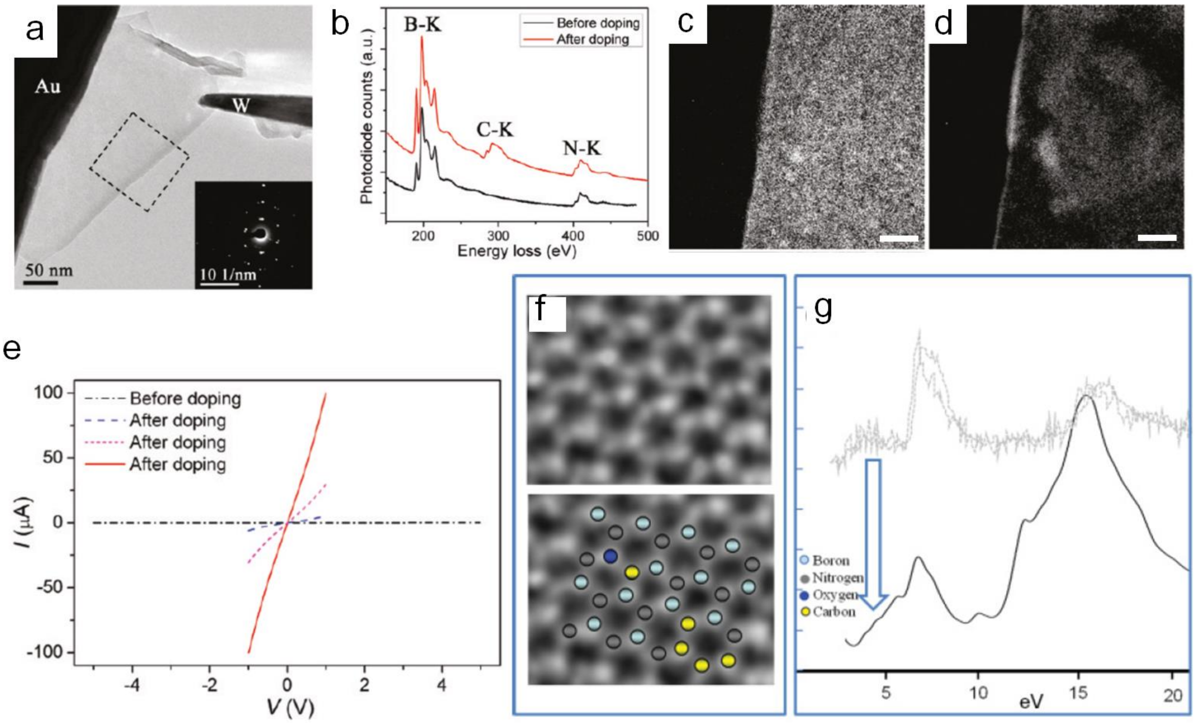

Figure.13 Doping effect in monolayer BN. (a) TEM image of a BN nanosheet. (b) EELS spectra of BN nanosheets before and after doping. (c, d) Energy filtered TEM image of B and C elements, respectively. (e) Electric transport of the nanosheet. The C doping changes the insulating BN into a semiconductor. Reproduced with permission.[135] Copyright 2011, American Chemical Society. (f) Experimental ADF-STEM image of monolayer BN with C dopants (yellow dots) (g) Corresponding low loss spectra of C-doped BN. The experimental electronic excitation below the bandgap of BN is consistent with simulated spectra, indicating the semiconducting properties induced by C doping. Reproduced with permission.[145] Copyright 2012, American Physical Society.

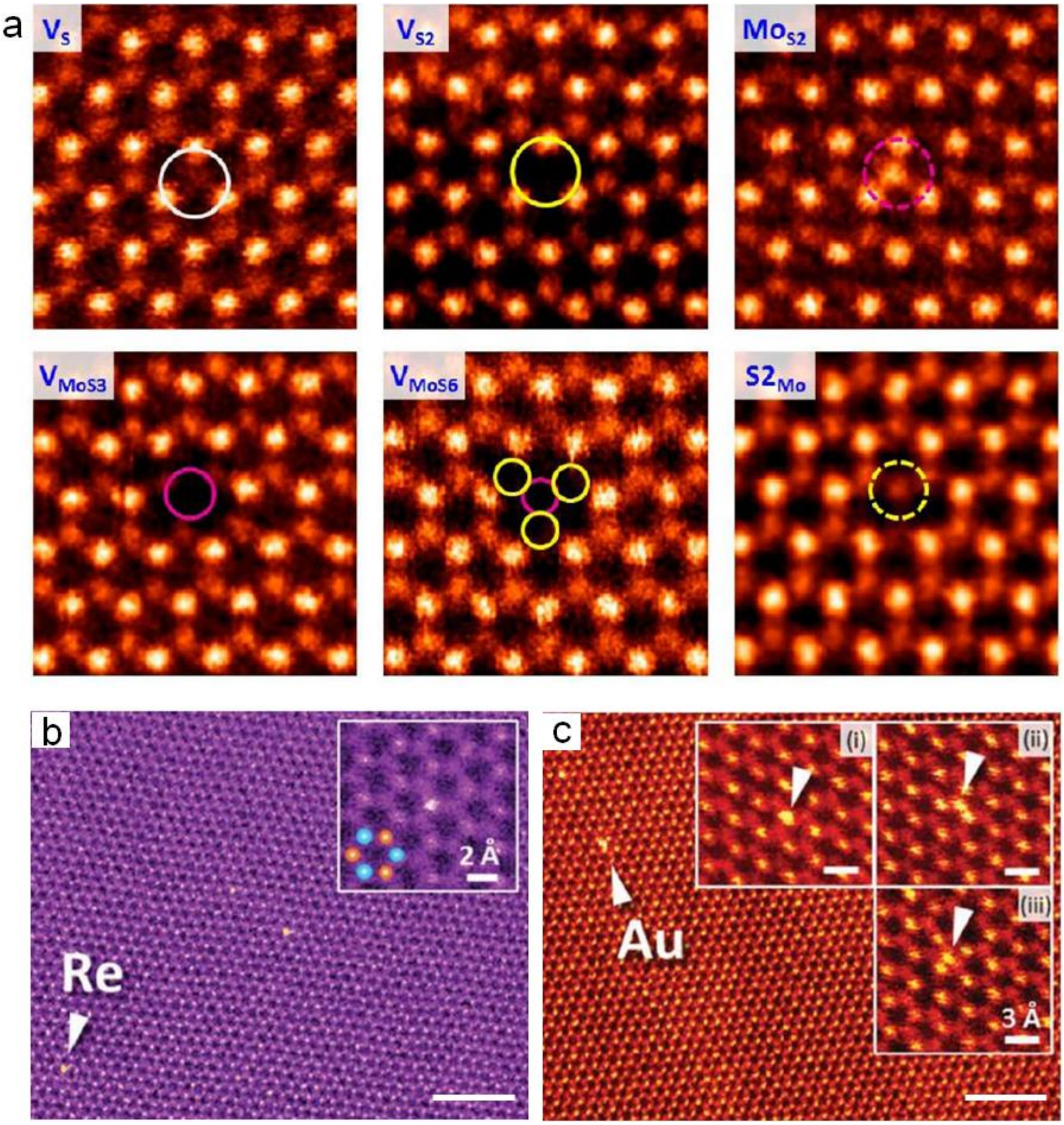

Figure.14 Single-atom defects in monolayer MoS_2. (a) Experimental ADF image of vacancies and antisite defects in MoS_2. Reproduced with permission.[174] Copyright 2013, American Chemical Society. (b) Re adatom on monolayer MoS_2. (c) Au adatom on monolayer MoS_2. Reproduced with permission.[182] Copyright 2014, Wiley-VCH.

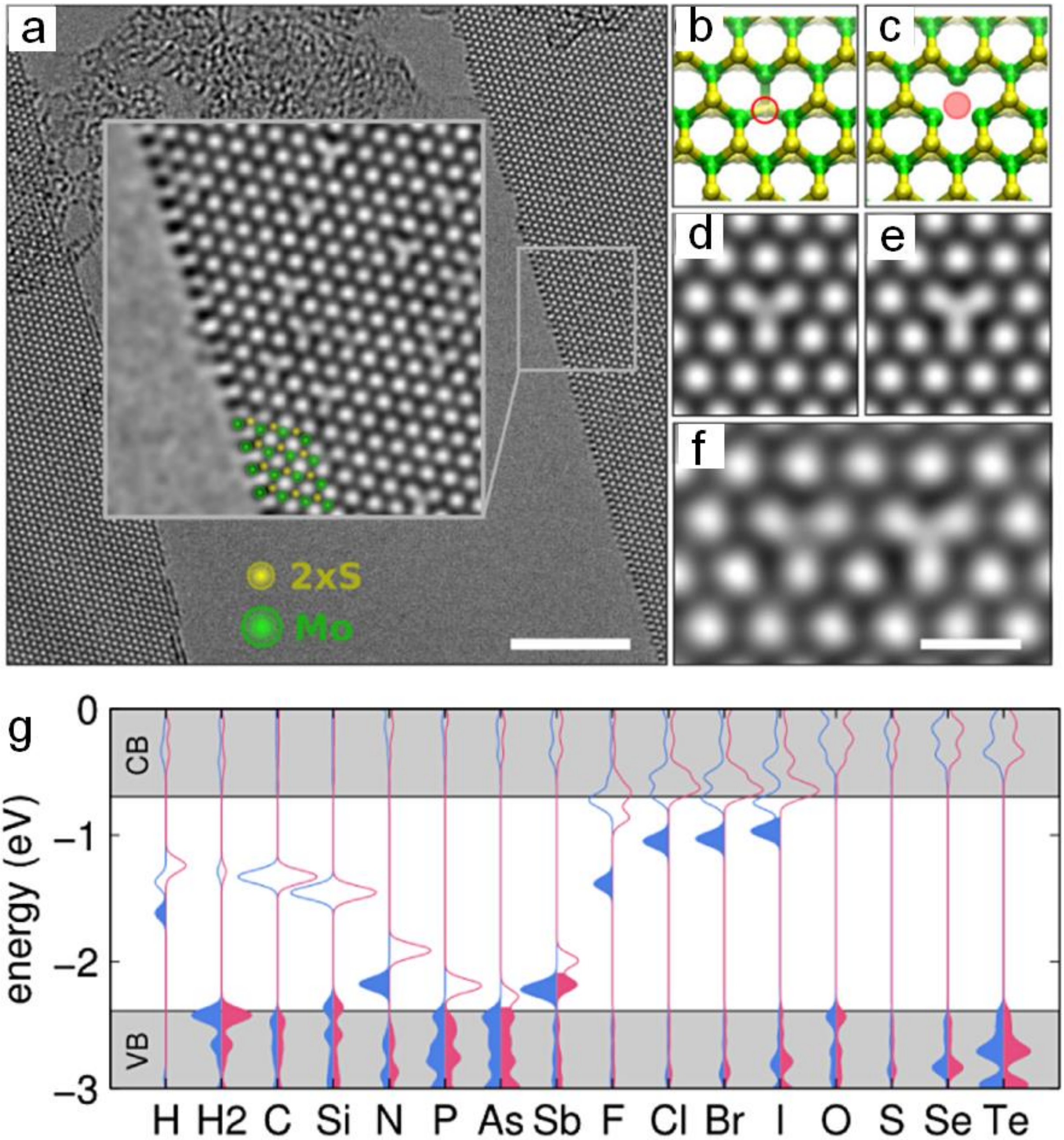

Figure.15 Vacancies and electronic structure engineering by substitutional doping in MoS_2. (a) Experimental HRTEM image of vacancies in MoS_2. (b, c) DFT-relaxed structure of V_S and V_{S2}. (d, e) Simulated HRTEM image of V_S and V_{S2}. (f) Experimental image of both V_S and V_{S2}. (g) Calculated DOS of dopants occupying the V_S site. Filled spin-resolved states are colored. Reproduced with permission.[184] Copyright 2012, American Physical Society.

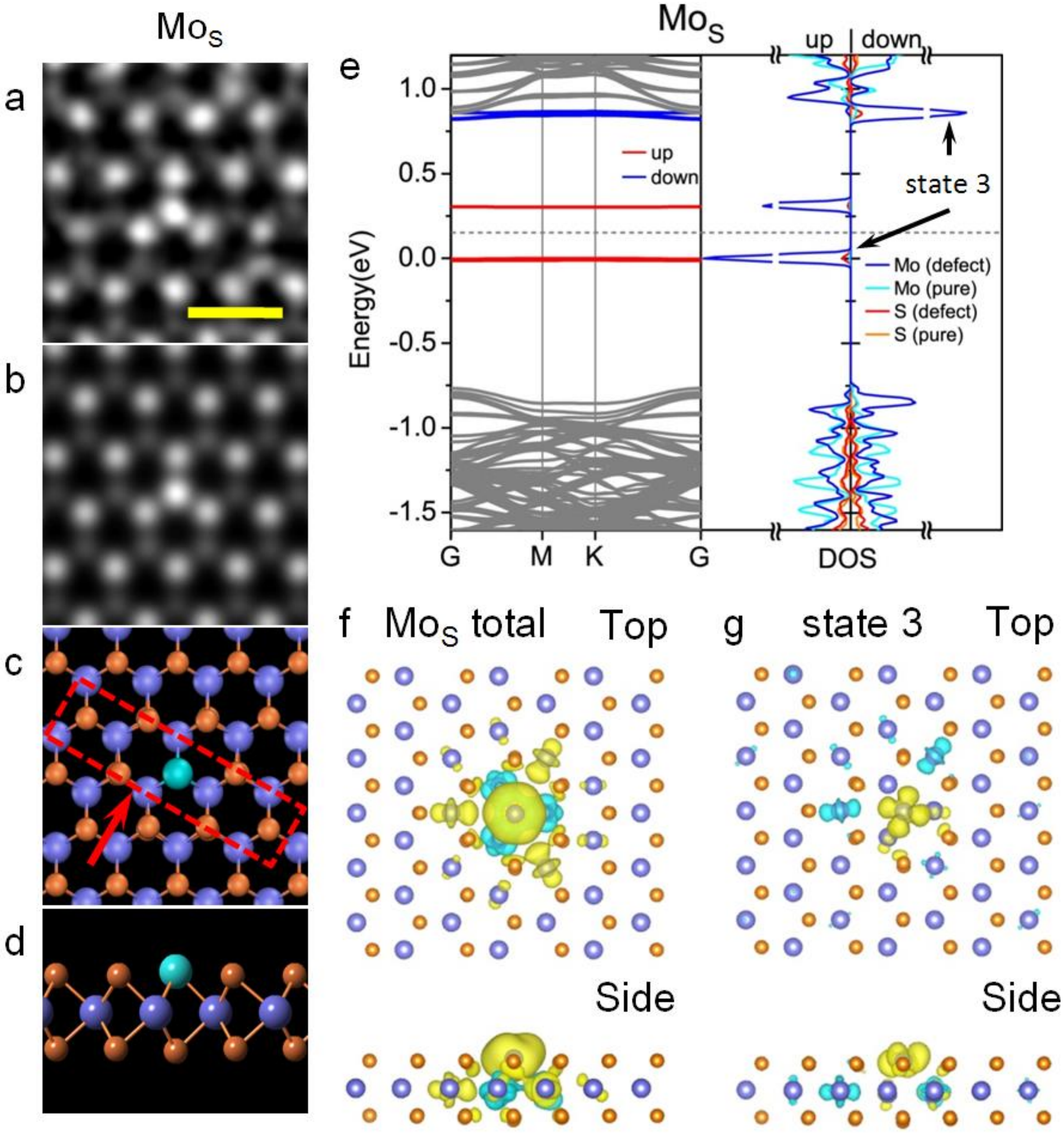

Figure.16 Antisite defect in monolayer MoS$_2$ and its electronic property. (a, b) Experimental and simulated ADF image of antisite defect Mo$_S$, respectively. Scale bar: 0.5 nm. (c, d) Top view and side view of relaxed structure of antisite Mo$_S$. (e) Calculated spin-resolved electronic structure and DOS. Dashed line is the Fermi level. (f) The distribution of the total spin charge density. Yellow marks spin up and cyan spin down. (g) Real-space distribution of defect state 3 in e. Reproduced with permission.[190] Copyright 2015, Nature Publishing Group.

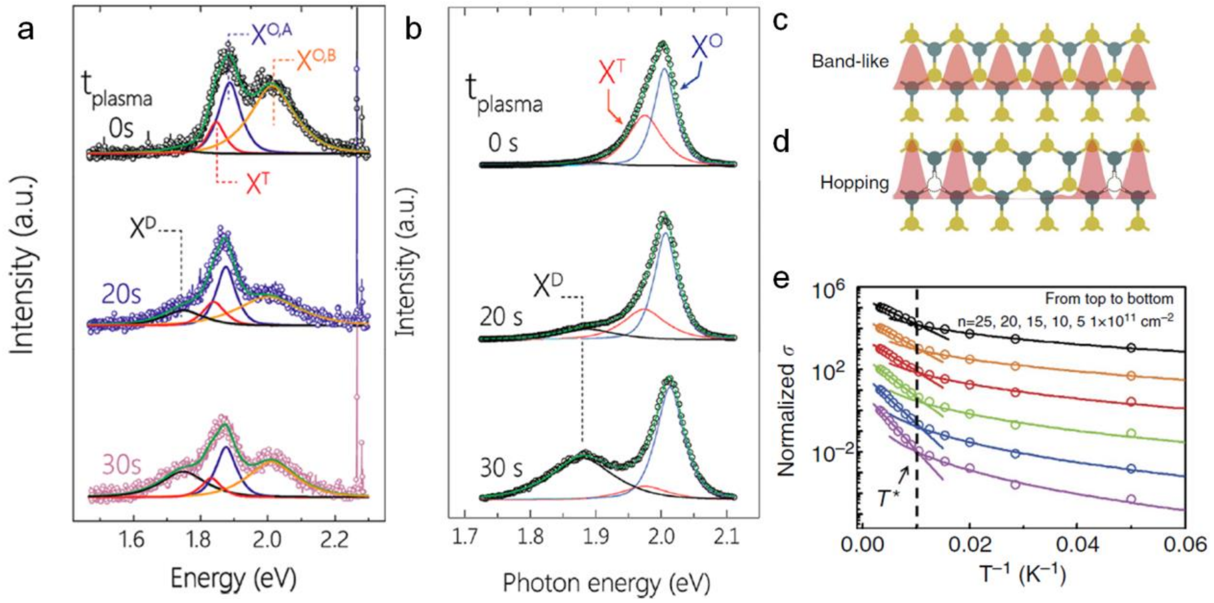

Figure.17 Optical and transport properties induced by vacancies in TMDs. (a) Photoluminescence of monolayer MoS_2 with the presence of vacancy defect induced by plasma etching. (b) Vacancy-related defect peaks in the photoluminescence of WS_2 evolving with plasma treatment. Reproduced with permission.[197] Copyright 2015, American Chemical Society. (c, d) Schematics of band-like electronic transport through normal bands and hopping transport through defect states. (e) Experimental variable-temperature conductance measurements in MoS_2. Reproduced with permission.[194] Copyright 2013, Nature Publishing Group.

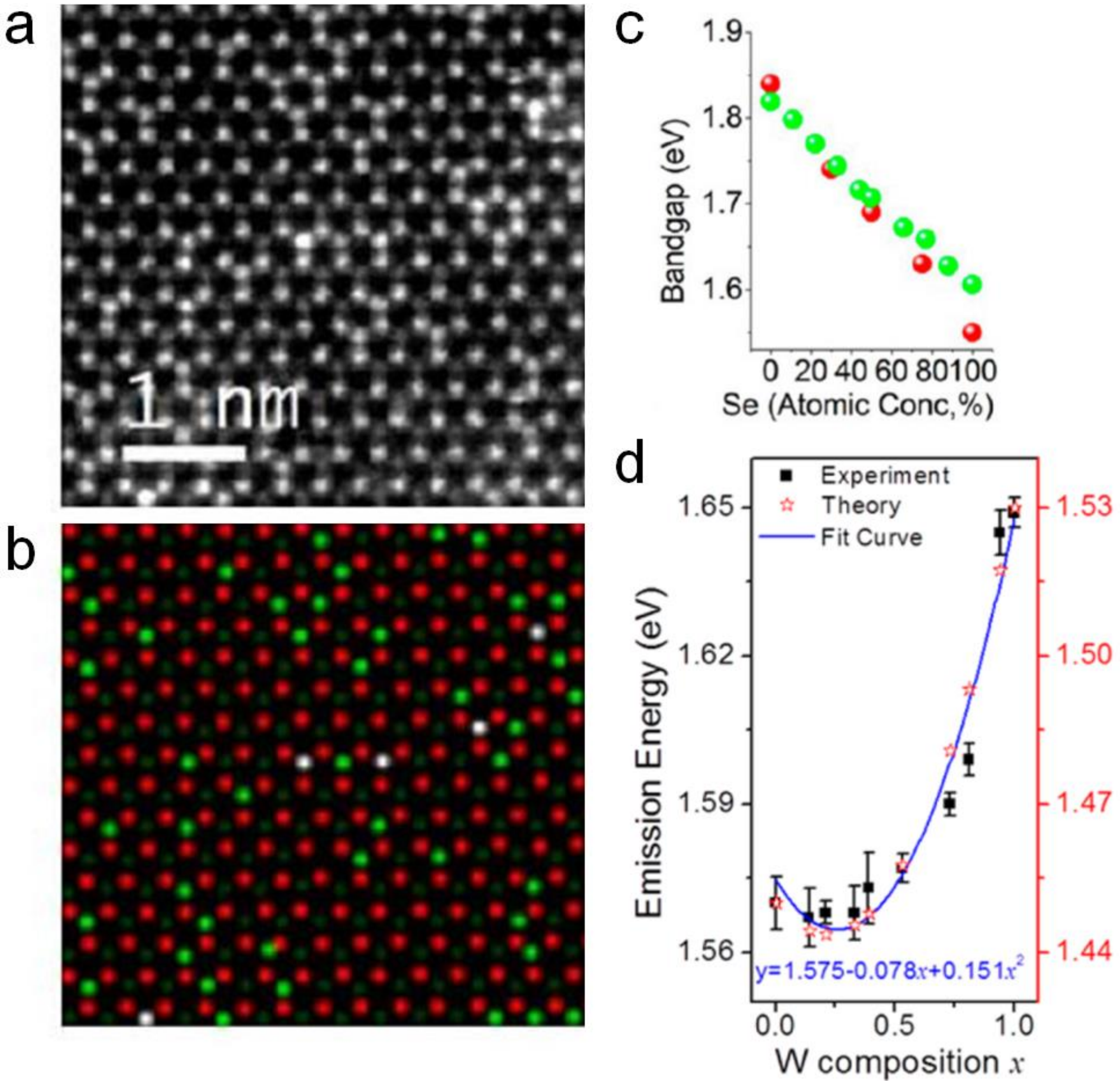

Figure.18 Optical gap engineering by chemical doping in TMDs. (a, b) Experimental ADF image of Se-doped monolayer MoS$_2$. (b) Chemically resolved atomic structure in different colors to demonstrate the distribution of Se dopants. Red dots are Mo, dark green S$_2$, bright green SSe and white Se$_2$. (c) Composition dependent bandgap of monolayer MoS$_{2-2x}$Se$_{2x}$ measured by photoluminescence spectroscopy. Reproduced with permission.[209] Copyright 2014, American Chemical Society. (d) Bandgap of monolayer Mo$_{1-x}$W$_x$Se$_2$. Reproduced with permission.[214] Copyright 2014, American Chemical Society.

69

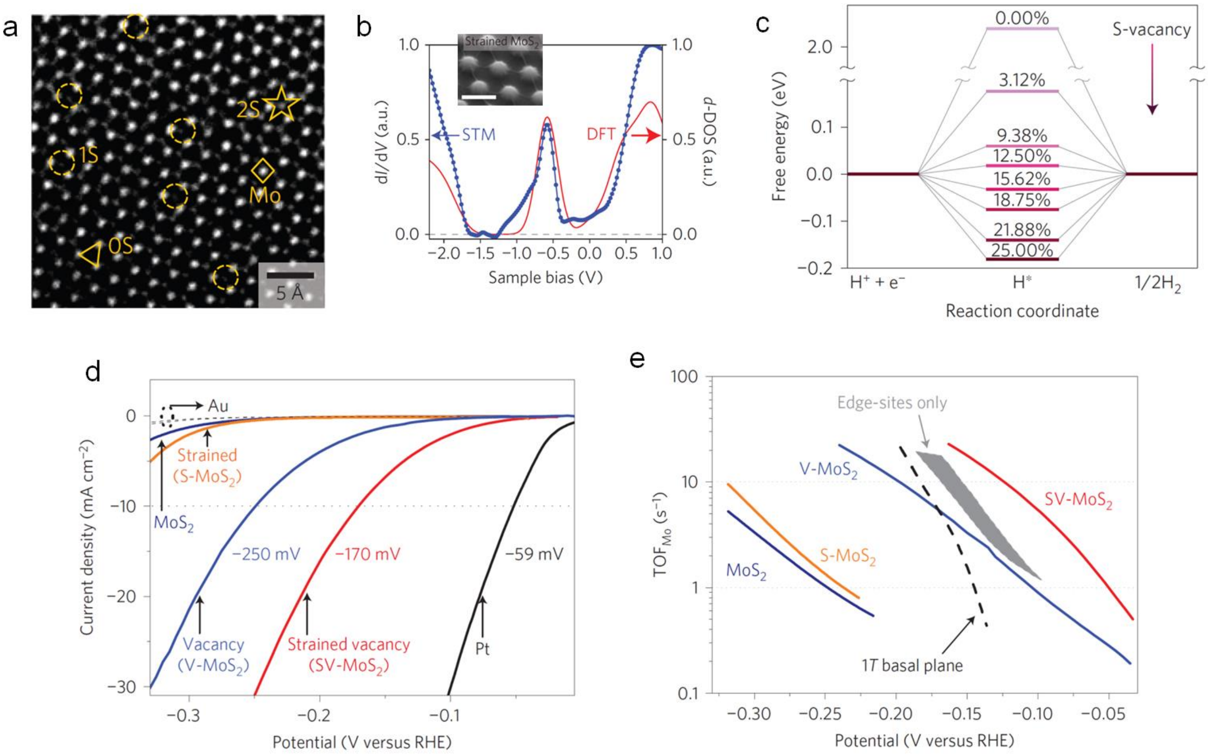

Figure.19 Enhanced catalysis of strained MoS_2 with vacancy defects. (a) Experimental ADF image of monolayer MoS_2 with sulfur vacancy engineering by controllable plasma etching. (b) Experimental STS and DFT-calculated *d*-DOS of defective MoS_2. (c) Calculated hydrogen adsorption free energy ΔG_H for S-vacancies with different concentrations. (d) Polarization curves of pristine, strain-only (S-MoS_2), vacancy-only (V-MoS_2) and strain-vacancy-combined MoS_2 (SV-MoS_2) for hydrogen evolution reaction (HER), in comparison with that of Pt. (e) The turnover frequency per surface Mo atom in various MoS_2. Reproduced with permission.[237] Copyright 2016, Nature Publishing Group.

Table 1 | Phonon-limited carrier mobility estimation of perfect and defective MoS_2 monolayers. Reproduced with permission.[190] Copyright 2015, Nature Publishing Group.

	m^*/m_0				***E*(eV)**				**μ ($cm^2V^{-1}s^{-1}$)**			
	e	**h**	***d*-e**	***d*-h**	**e**	**h**	***d*-e**	***d*-h**	**e**	**h**	***d*-e**	***d*-h**
Perfect	0.40	-0.57	-	-	-14.9	-3.4	-	-	410	3850	-	-
V_S	0.43	-0.96	35.2	105.6	-13.9	-3.4	-4.5	5.4	410	1390	<1	<1
V_{S2}	0.42	-1.2	31.1	9.2	-13.9	-3.1	-4.9	6.8	426	1066	<1	4
Mo_S	0.99	-1.2	75.5	34.1	-11.1	-4.0	-3.0	-2.9	123	631	<1	2
Mo_{S2}	0.71	-1.1	8.8	28.6	-13.3	-3.6	-4.3	-6.8	164	902	10	<1

(1) Carrier types ‘e’ and ‘h’ denote ‘electron’ and ‘hole’ for the original conduction and valence bands in perfect MoS_2 monolayer, and ‘*d*-e’ and ‘*d*-h’ represent those for the defect states, respectively;

(2) All mobilities are estimated based on the intrinsic limit 410 $cm^2V^{-1}s^{-1}$ for the electron mobility in the perfect monolayer.

Author CV

Dr. **Jinhua Hong**, He obtained his B.S. from Department of Physics, Zhejiang University and will obtain Ph.D. degree from Materials Science and Engineering of Zhejiang University, China. His research is mainly on two-dimensional materials and electron energy loss spectroscopy. He just joined the Japan Fine Ceramics Center as a postdoc research associate.

Prof. Dr. **Chuanhong Jin**, is now leading a research team in the Center of Electron Microscopy, State Key Laboratory of Silicon Materials and School of Materials Science and Engineering in Zhejiang University. He is mostly working on resolving the atomic and electronic structures of two-dimensional material by advanced electron microscopy, and liquid-cell electron microscopy.

Prof. Dr. **Jun Yuan**, is Professor of Nanophysics and Electron Microscopy at Department of Physics, University of York. He also holds a visiting Professorship at School of Materials Science and Engineering and the Center of Electron Microscopy, State Key Laboratory of Silicon Materials and School of Materials Science and Engineering in Zhejiang University. His current research interests are in the development of novel electron microscopy and spectroscopy techniques as well as growth and structural characterization of nanomaterials, including two-dimensional layer systems.

Prof. Dr. **Ze Zhang** is now the director of the Center of Electron Microscopy of Zhejiang University. He is also a Member of Chinese Academy of Sciences, the President of Asia-Pacific Microscopy Society and President of Chinese Electron Microscopy Society. Most of his recent work has been focused on the microstructure-property correlation of low-dimensional functional materials.

The table of contents entry should be 50−60 words long (max. 400 characters), and the first phrase should be bold.

Single-atom defects are systematically reviewed in two-dimensional material systems such as graphene, BN and transition metal dichalcogenides. The local atomic arrangement and associated electronic structure were probed by transmission electron microscopy and single-atom spectroscopy, and the influence from the defects on the macroscopic functionalities of two-dimensional materials are discussed, focusing mostly on electronics, photonics, nanomagnetism and catalysis.

ToC figure ((Please choose one size: 55 mm broad × 50 mm high **or** 110 mm broad × 20 mm high. Please do not use any other dimensions))